ADVERTIMENT. La consulta d'aquesta tesi queda condicionada a l'acceptació de les següents condicions d'ús: La difusió d'aquesta tesi per mitjà del servei TDX (www.tesisenxarxa.net) ha estat autoritzada pels titulars dels drets de propietat intel·lectual únicament per a usos privats emmarcats en activitats d'investigació i docència. No s'autoritza la seva reproducció amb finalitats de lucre ni la seva difusió i posada a disposició des d'un lloc aliè al servei TDX. No s'autoritza la presentació del seu contingut en una finestra o marc aliè a TDX (framing). Aquesta reserva de drets afecta tant al resum de presentació de la tesi com als seus continguts. En la utilització o cita de parts de la tesi és obligat indicar el nom de la persona autora.

ADVERTENCIA. La consulta de esta tesis queda condicionada a la aceptación de las siguientes condiciones de uso: La difusión de esta tesis por medio del servicio TDR (www.tesisenred.net) ha sido autorizada por los titulares de los derechos de propiedad intelectual únicamente para usos privados enmarcados en actividades de investigación y docencia. No se autoriza su reproducción con finalidades de lucro ni su difusión y puesta a disposición desde un sitio ajeno al servicio TDR. No se autoriza la presentación de su contenido en una ventana o marco ajeno a TDR (framing). Esta reserva de derechos afecta tanto al resumen de presentación de la tesis como a sus contenidos. En la utilización o cita de partes de la tesis es obligado indicar el nombre de la persona autora.

WARNING. On having consulted this thesis you're accepting the following use conditions: Spreading this thesis by the TDX (www.tesisenxarxa.net) service has been authorized by the titular of the intellectual property rights only for private uses placed in investigation and teaching activities. Reproduction with lucrative aims is not authorized neither its spreading and availability from a site foreign to the TDX service. Introducing its content in a window or frame foreign to the TDX service is not authorized (framing). This rights affect to the presentation summary of the thesis as well as to its contents. In the using or citation of parts of the thesis it's obliged to indicate the name of the author

Contribution to the Improvement of the Soil Moisture and Ocean Salinity (SMOS) Mission Sea Surface Salinity Retrieval Algorithm

UPC
Departament de Teoria
del Senyal i Comunicacions
UNIVERSITAT POLITÈCNICA DE CATALUNYA

Marco Talone

Remote Sensing LAB - Teoria del Senyal i Comunicacions Department

Universitat Politcnica de Catalunya, UPC

Advisors

Prof. Adriano José Camps Carmona, UPC
Dr. Carolina Gabarró Prats, ICM/CSIC

A thesis submitted for the degree of

PhilosophiæDoctor (PhD)

October 2010

“È difficile, caro, dimostrare in modo
soddisfacente qualche cosa di importante
senza aiutarci con dei modelli.”

Platone, Politico.

“The higher ideas, my dear friend,
can hardly be set forth
except throught the medium of models.”

Plato, Stateman.

Acknowledgements

First, I would like to acknowledge *Prof. Adriano José Camps Carmona*, *Dr. Carolina Gabarró*, my advisors, as well as *Dr. Mercé Vall-llossera Ferran* and *Prof. Jordi Font Ferré* for their support, guidance, and advice during the last years. A particular acknowledgment goes to *Dr. Roberto Sabia* and *Dr. Jérôme Gourrion*, who strongly contributed to this thesis sharing their experience with me and helping me to solve my daily problems. Thanks to the *Remote Sensing Laboratory* of the *Teoria del Senyal i Comunicacions* Department of the *Universitat Politècnica de Catalunya* and to Departament of *Oceanografia Física* of the *Institut de Ciències del Mar* for giving me the opportunity of carring out my PhD thesis in a very interesting, inter-disciplinary, and challenging environment.

A special acknowledgement goes also:

> to *Professor Paolo Ferrazzoli* of the "Universita di Tor Vergata", Roma, whose lectures awoked my interest for the remote sensing.
>
> to *Dr. Jacqueline Boutin* and *Dr. Gilles Reverdin* for kindly hosting me in their institution (the Laboratoire d'Oceanographie et du Climat: Experimentation et Approches Numeriques, LOCEAN, Paris) during the months of May - July 2008.
>
> to *Mr. Fernando Martin-Porqueras*, *Dr. Juha Kainulainen*, *Dr. Joseph Tenerelli*, and *Dr. Manuel Martin-Neira* for their very useful remarks and advice during the processing of the HUT data (chapter 6).
>
> to *Mr. Fernando Pérez López* and *Dr. Justino Martinez González* for their willingness and professionalism in fixing all the weird and untimely computer problems I experienced so far.

Finally, I would like to express my gratitude to *Dr. Sandra Monerris* and *Dr. Maria Piles* for their fundamental help in writing this thesis.

This work was supported by the Spanish National Program on Space under the Projects ESP2005-06823-C05 (MIDAS-4) and ESP2007-65667-C04 (MIDAS-5) and the Spanish Ministry of Science and Innovation through the Formación de Personal Investigador (FPI) fellowship ESP2005-06823-C05-02.

Abstract

The European Space Agency's Soil Moisture and Ocean Salinity (SMOS) satellite was launched on November, 2, 2009 from the Russian cosmodrome of Plesetsk. Its objective is to globally and regularly collect measurements of soil moistre and Sea Surface Salinity (*SSS*). To do that, a pioneering instrument has been developed: the Microwave Imaging Radiometer by Aperture Synthesis (MIRAS), the first space-borne, 2-D interferometric radiometer ever built; it operates at L-band, with a central frequency of 1.4135 GHz, and consists of 69 antennas arranged in a Y shape array. MIRAS' output are brightness temperature maps, from which *SSS* can be derived through an iterative algorithm, and using auxiliary information. For each overpass of the satellite an *SSS* map is produced, with an estimated accuracy of 1 psu (rmse). According to the Global Ocean Data Assimilation Experiment (GODAE) the mission requirement is instead specified as 0.1 psu after averaging in a 10-day and $2^\circ \times 2^\circ$ spatio-temporal boxes.

In previuos works ((*Sabia et al.*, 2010), or more extensively in Dr. Sabia's Ph.D. thesis (*Sabia*, 2008)) the main error sources in retrieving *SSS* from SMOS measurements were determined as:

1. Scene-dependent bias in the simulated measurements,
2. L-band forward modeling definition,
3. Radiometric sensitivity and accuracy,
4. Constraints in the cost function, and
5. Spatio-temporal averaging.

This Ph.D. thesis, is an attempt of reducing part of the aforementioned errors (the relative to the one-overpass *SSS* (1 - 4)) by a more sophisticated

data processing.

Firstly, quasi-realistic brightness temperatures have been simulated using the SMOS End-to-end Performance Simulator (SEPS) in its full mode and an ocean model, as provider for geophysical parameters. Using this data set the *External Brightness Temperature Calibration* technique has been tested to mitigate the scene-dependent bias, while the error introduced by inaccuracies in the L-band forward models has been accounted for by the application of the *External Sea Surface Salinity Calibration*.

Apart from simulated brightness temperatures, both *External Brightness Temperature Calibration* and *External Sea Surface Salinity Calibration* have been tested using real synthetic-aperture brightness temperatures, collected by the Helsinki University of Technology HUT-2D radiometer during the SMOS Calibration and Validation Rehearsal Campaign in August 2007 and ten days of data acquired by the SMOS satellite between July 10 and 19, 2010.

Finally, a study of the cost function used to derive *SSS* has been performed: the correlation between measurement misfits has been estimated and the effect of including it in the processing have been assessed.

As an outcome of a 3-month internship at the Laboratoire LOCEAN in Paris, France, a theoretical review of the effect of the rain on the very top *SSS* vertical profile has been carried out and is presented as Appendix.

Contents

List of Figures

List of Tables

Glossary

AF-FOV	Alias-Free Field of View
AMIRAS	Airborne MIRAS
CATDS	Centre Aval de Traitement de Données
CCSDS	Consultative Committee for Space Data Systems
CDTI	Centro para el Desarrollo Tecnologico Industrial
CEOS	Comittee on Earth Observation Satellites
CMN	Control and Monitoring Nodes
CNES	Centre Nationale dÉtudes Spatiales
CP34	Centro de Producción de niveles 3 y 4
ECMWF	European Centre for Medium-range Weather Forecast
ESA	European Space Agency
FOV	Field of View
GODAE	Global Ocean Data Assimilation Experiment
GPS	Global Positioning System
IEM	Integral Equation MEthod
IFREMER	Institut Français de Recherche pour l'Exploitation de la Mer
ISEA	Icosahedron Snyder Equal Area
KM	Kirchoff Model
L2PP	Level 2 Prototype Processor
LAURA	L-band AUtomatic RAdiometer
LICEF	LIghtweight Cost-Effective Front-end
MIRAS	Microwave Imaging Radiometer by Aperture Synthesis
MLE	Maximum Likelihood Estimator
MSS	Mean Square Slope
NCEP	National Center for Environmental Predictions
NIR	Noise Injection Radiometer
PSU	Pactical Salinity Units
SEPS	SMOS End-to-end Performance Simulator
SMOS	Soil Moisture and Ocean Salinity
SPM	Small Perturbation Model
SSA	Small Slope Approximation
SSS	Sea Surface Salinity
SWH	Significant Wave Height
TEC	Total Electron Content
TSM	Two Scale Model
UPC	Universitat Politécnica de Catalunya
WISE	WInd and Salinity Experiment
WOA	World Ocean Atlas

Preface

According to Thermodynamics, the Earth can be defined as a closed system; In facts, it can only exchange energy, not matter, with its surroundings (asteroid penetrations and satellite leavings can be definitely neglected). Global water content on Earth, as any other matter, doesn't change; nevertheless water doesn't stand steady, but it is in continous movement.

Water relentlessy changes in position and state, moving throghout the whole planet in liquid, gaseous, and solid states; this proces is called the *Water Cycle*. The Water Cycle affects, and is studied by, several disciplines, among them Oceanography, Meteorology, Hydrology, Agronomy etc.

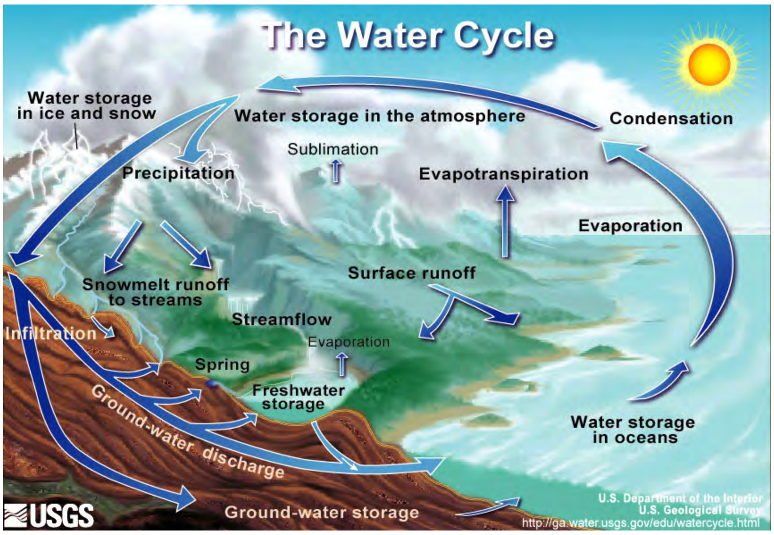

Figure 1: The Water Cycle (from http://ga.water.usgs.gov).

It is obvious that water is crucial for human life in the day-by-day needs, anyway the same importance is played in large-scale dynamics. Water cycle is, in fact, responsible of mitigating climate variations and homogenizing Earth's temperature, being at the same time a good tracer and forcer of climate changes.

Among the variables mirroring the water cycle, sea surface salinity (*SSS*) is maybe the most important one, or at least, it is the one whose knowledge would improve most the characterization of the large-scale water dynamics (*Lagerloef et al.*, 1995). Sea surface salinity is the direct observable that includes the changes in water density induced by evaporation, precipitation, ice melting, and rivers run-offs; which are, in turn, the first drivers of the oceanic currents. In Figs. 2a and 2b the most important ocean surface currents and the thermohaline circulation (the so-called *"Conveyor Belt"*) are shown.

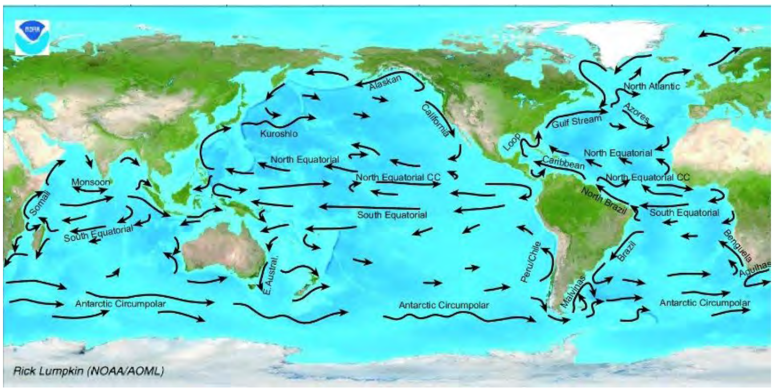

(a)

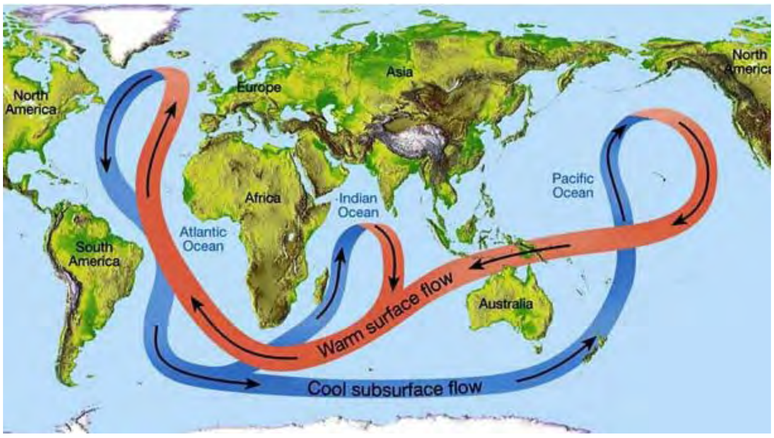

(b)

Figure 2: (a) The main ocean surface currents (from NOAA) and (b) the thermohaline current (from www.global-greenhouse-warming.com)

Anyway, even though the importance of a better understanding of the water cycle and of the role played by sea surface salinity has been widely accepted, until recently, any progress in their knowledge has been limited by the available technology. Monitoring *SSS* implies periodic and global-scale measurements, making unfeasable in situ direct sampling. As shown in Fig. 3 even today 50% of the ocean is, in fact, not sampled on a regular basis.

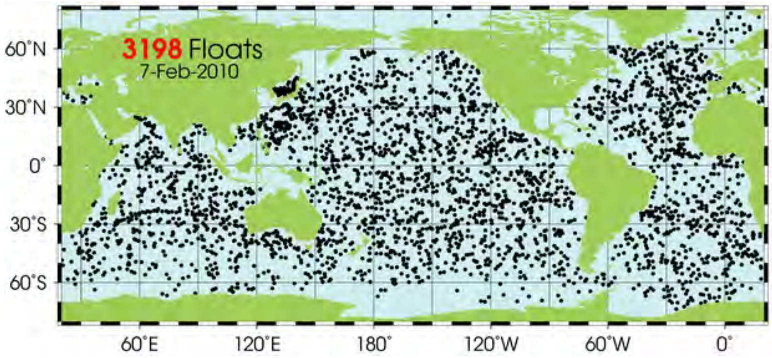

Figure 3: In situ observations of the sea surface salinity up to February 2010

During the last decades much effort has been spent by the scientific community to overcome these difficulties and, finally, satellite microwave radiometry has been chosen as the optimal measurement technique. Satellite microwave radiometry presents several advantages: from one side, satellites permit the synoptic measurements of the Earth with a good revisit time (3 days for SMOS); on the other side, since microwave measurements can be acquired during both day-time and night-time regardless of the weather conditions (atmosphere is almost transparent at these frequencies) both European Space Agency (ESA) and National Aeronautics and Space Administration (NASA) have active programmes to measure *SSS* using satellite microwave radiometers: the European one (SMOS) was launched on November 2009, whereas the NASA Aquarius mission is scheduled for the first half of 2011.

The optimization of the sea surface salinity retrieval algorithms for the SMOS mission are the topic of this Ph.D. thesis, that is structured as follows (articles directly arised from the elaboration of the thesis are referred between brackets in the corresponding chapter):

Chapter 1 : Introduction of the basic concepts of microwave radiometry.

Chapter 2 : Review of the mostly used L-band emissivity models.

Chapter 3 : SMOS mission description.

Chapter 4 : Description and testing of two pre- (*External Brightness Temperature Calibration*) and post- (*External Sea Surface Salinity Calibration*) processing techniques to improve *SSS* retrieval performance.

[M. Talone, A. Camps, B. Mourre, R. Sabia, M. Vall-llossera, J. Gourrion, C. Gabarró, and J. Font. Simulated SMOS level 2 and 3 products: The effect of introducing ARGO data in the processing chain and its impact on the error induced by the vicinity of the coast. *IEEE Trans. on Geosci. and Remote Sens., 47(9): 3041 - 3050,* September 2009.]

Chapter 5 : Analysis of the brightness temperature misfits covariance matrices. Assessment of the retrieval performance using covariance matrices, the cost functions in literature, or a new expression proposed.

[**UNDER REVISION** M. Talone, A. Camps, R. Sabia, M. Vall-llossera, C. Gabarró, J. Gourrion, and J. Font. Error covariance matrices characterization in the ocean salinity retrieval cost function within the SMOS mission *Journal of Atmospheric and Oceanic Technology, XX(XX): x - x,* XX.]

Chapter 6 : Testing of the proposed techniques on real data acquired by the Helsinki University of Technology HUT-2D radiometer, and by the SMOS satellite.

[M. Talone, R. Sabia, A. Camps, M. Vall-llossera, C. Gabarró, and J. Font. Sea Surface Salinity Retrievals from HUT-2D L-band Radiometric Measurements. *Remote Sensing of the Environment, 114: 1756 - 1764,* 2010. doi: 10.1016/j.rse.2010.03.006]

Chapter 7 : Main conclusions and summary of the original contributions of the PhD.

Chapter 8 : Future research lines overview.

Appendix A : Analysis of the rain effect on brightness temperature - as outcome of the 3-month stage at LOCEAN, Paris.

Appendix B : List of Publications.

1

Introduction to microwave radiometry

This chapter is devoted to provide to the reader the necessary background on microwave radiometry: the basics of this discipline are described, as well as the main concepts of the radiative transfer theory.

1.1 Introduction

Radiometry is the field of science devoted to the measurement of the electromagnetic radiation. Its application is useful, and sometimes even fundamental, for many other disciplines such as physical oceanography, biology, atmospheric modeling, weather forecasting, agronomy etc...

Most of the energy received by the Earth comes from the Sun as electromagnetic radiation. Part of this energy is diffused or absorbed by the atmosphere, the rest is transmitted down to the Earth's surface; once on the surface, the energy is, once again, partly scattered and partly absorbed. According to Thermodynamics laws, when the thermal equilibrium is reached the energy absorbed by both the atmosphere and the surface is then re-emitted. All these energy transformations are subject to the so-called *radiative transfer law*, and the aforementioned spontaneous emission is the quantity measured by radiometers.

Several geophysical parameters can be estimated by means of radiometric measurements, but since the whole process is very complex and involves many different physical elements and phenomena, in order to achieve the adequate accuracy of the estimates a number of things must be taken into account. The basic concepts concerning microwave radiometry are addressed in this chapter. Next chapter is focused on the description of the currently used forward models when observing sea surface emission.

1.2 Planck's law and the black body radiation

Planck's law expresses the emitted power dependence on the physical temperature and frequency for an ideal body called the *black body.* The black body is defined as an ideal, perfectly opaque, material that absorbs all the incident radiation at every frequency of the spectrum (and re-emits it all once the thermal equilibrium is reached). Accordingly, a black body satisfies the following properties:

- It absorbs all the incident radiation, independently from the wavelength or the direction.
- For a given temperature and wavelength no material can emit more energy than the black body.
- Even though the radiation emitted by a black body is a function of the wavelength it is not dependent on the direction. The black body is defined as a *scatter emitter.*

A plot of the emitted energy density by a black body according to the Plack's Law (*Planck*, 1901), as a function of the physical temperature and the wavelength, is shown in Fig. 1.1. It can be noticed that the emitted energy increases and its maximum moves towards lower wavelengths with increasing the physical temperature of the body.

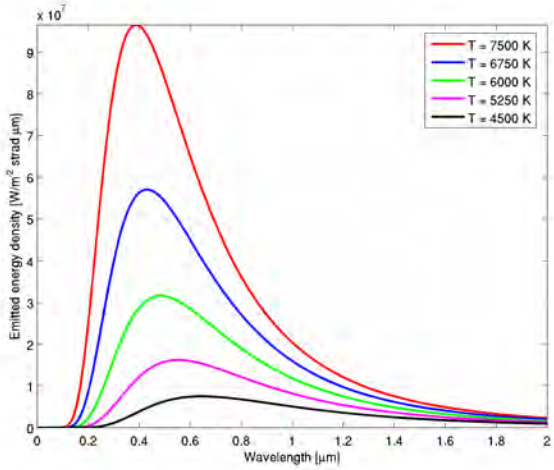

Figure 1.1: The Black Body - Emitted energy density as a function of the temperature and of the wavelength

1.3 Brightness or radiance

Considering a surface element with area A_t $[m^2]$, emitting with an angular distribution function F_t $[W \cdot sr^{-1}]$, and a receiving antenna characterized by its effective area A_r $[m^2]$ oriented one in front of the other in the direction of maximum directivity and at a distance R for which the power density S_t $[W \cdot m^{-2}]$ can be considered constant over the solid angle Ω_t $[sr]$, then the received power is given by Eqn. 1.1:

$$P = S_t A_r = F_t \frac{A_r}{R^2}. \tag{1.1}$$

The *brightness*, or *radiance*, B $[W \cdot m^{-2} \cdot sr^{-1}]$ can be then defined as the power flux emitted F_t per unity of surface A_t and solid angle:

$$B = \frac{F_t}{A_t}. \tag{1.2}$$

Then, the received power in Eqn. 1.1 can be expressed as:

$$P = B \cdot A_r \frac{A_t}{R^2} = B A_r \Omega_r, \tag{1.3}$$

which, considering an infinitesimal solid angle and expressing as $F_n(\theta, \varphi)$ the normalized receiving antenna pattern, leads to:

$$dP = A_r B(\theta, \varphi) F_n(\theta, \varphi) d\Omega df. \tag{1.4}$$

In this way, the total power received by the antenna from all possible directions in a band Δf $[Hz]$ can be written as:

$$P = \frac{1}{2} A_r \int_f^{f+\Delta f} \iint_{4\pi} B_f(\theta, \varphi) F_n(\theta, \varphi) d\Omega df, \tag{1.5}$$

where the term 1/2 accounts for the fact that an antenna can only receive in one polarization while the emitted radiation is randomly polarized.

1.4 Thermal radiation

As stated, defining the black body as the ideal body absorbing all the incident energy along the whole spectrum, it is also defined as the perfect emitter. The brightness spectral density B_f $[W m^{-2} sr^{-1} Hz^{-1}]$ of a black body depends thus only on its physical temperature T_0 and frequency f. Being h_P the Plack's constant ($6.63 \times 10^{-34} Js$), c the speed of propagation in vacuum ($3 \times 10^8 m s^{-1}$), and k_B the Boltzmann's constant

$(1.38 \times 10^{-23} JK^{-1})$, B_f is expressed, according to the Planck's radiation law (*Planck*, 1901), as:

$$B_f = \frac{2h_P f^3}{c^2} \frac{1}{e^{\frac{h_P f}{k_B T_0}} - 1}. \tag{1.6}$$

In the microwave part of the spectrum $h_p \ll k_B T_0$, and it is possible to approximate Eqn. 1.6 by the Rayleigh-Jeans law:

$$B_f \simeq \frac{2k_B f^2 T_0}{c^2} = \frac{2k_B T_0}{\lambda^2}. \tag{1.7}$$

Taking into account Eqns. 1.5 ans 1.7 and considering a narrow enough bandwidth (Δf), the total power (P_{bb}) received by an antenna of effective area A_r completely surrounded by a black body at the physical temperature T_0 can be written as:

$$P_{bb} = k_B T_0 \Delta f \frac{A_r}{\lambda^2} \iint_{4\pi} F_n(\theta, \varphi) d\Omega, \tag{1.8}$$

but since:

$$\iint_{4\pi} F_n(\theta, \varphi) d\Omega = \Omega_P = \frac{\lambda^2}{A_r}, \tag{1.9}$$

where Ω_P is the antenna solid angle, Eqn. 1.9 becomes:

$$P_{bb} = k_B T_0 \Delta f. \tag{1.10}$$

Real materials do not behave as perfect emitters or absorbers and present a smaller brightness than the black body at the same physical temperature T_0. They are called *gray bodies*. To express the brightness of a gray body in a similar way as for a black body the *brightness temperature* T_B $[K]$ is defined so that:

$$B_f = \frac{2k_B T_B}{\lambda^2}. \tag{1.11}$$

At this stage it is possible to define a coefficient e (*emissivity*) as the ratio between the brightness of a gray body and the one of a black body at the same physical temperature.

$$e(\theta, \varphi) = \frac{B(\theta, \varphi)}{B_{bb}} = \frac{T_B(\theta, \varphi)}{T_0}. \tag{1.12}$$

Considering that by definition $0 \leqslant T_B \leqslant T_0$, it can be concluded that $0 \leqslant e \leqslant 1$.

1.5 Radiative transfer theory

The radiative transfer theory deals directly with the transportation of the energy through a medium containing particles, differently from the analytical theory which is derived from the differential Maxwell's equations. This theory describes the spatial behaviour of the radiation intensity in terms of spectral radiance (or brightness) propagating in a generic medium that can absorb, emit or scatter the radiation itself. The problem is usually approached in a scalar fashion, i.e. considering the spectral radiance at one polarization and not its decomposition in polarizations. The complete characterization considering media inhomogeneities and anysotropies is considered out of the scope of this introduction.

The radiative transfer theory is formulated through four constitutive functions:

- *absorption coefficient*, that describes the attenuation of the spectral radiance due to absorption.
- *scattering coefficient*, that describes the attenuation of the spectral radiance due to scattering.
- *thermal emission function*, that accounts for the volume element emission.
- *phase function*, that characterizes the incident and scattered radiation intensities coupling between polarizations and directions in every point within the medium.

To express the radiative transfer equation in differential form, and according to the direction of propagation r, let us consider a cylindrical volume element of base area dA, length dr, and whose axis is directed along r. In Fig. 1.2 the geometry of the problem is schematically represented .

The material constituting the propagation medium is considered to be homogeneous inside the volume, and $I(f, r)$ is the spectral radiance entering in it, impinging normally to the surface of the volume element at r. The spectral radiance $I(f, r+\delta r)$ leaving the volume in the direction normal to the surface at $r + \delta r$ is different from $I(f, r)$ due to the interaction with the medium. The processes that contribute to increase or decrease this radiance are briefly described in the following paragraphs.

1.5.1 Spectral radiance decrease due to absorption

Part of the energy associated to the radiation entering in the volume is absorbed, i.e. transformed in another form of energy (thermal), by the medium. To describe in

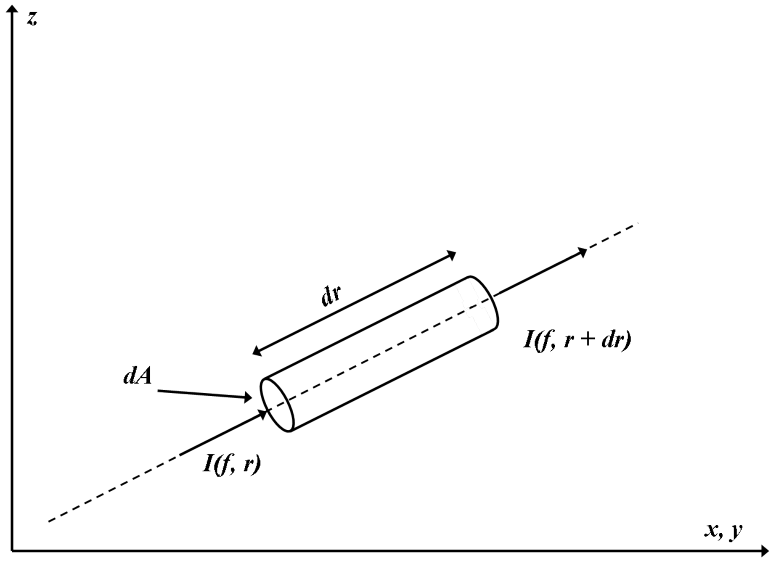

Figure 1.2: Radiative transfer through an elementary cylindrical volume

quantitative terms this decrease of spectral radiance it is necessary to introduce the *volumetric absorption coefficient* of the medium k_a $[Np \cdot m^{-1}]$, defined as:

$$k_a(f,r) = \frac{dW_a(f,r)}{dAdrP_i(f,r)} = \frac{dI_a(f,r)dAd\Omega df}{dAdrI(f,r)d\Omega df} = \frac{dI_a(f,r)}{drI(f,r)}, \tag{1.13}$$

where dW_a represents the power absorbed by the volume when a radiation characterized by the flow P_i (intensity of the Poynting vector) impinges normally on the surface $dA(r)$. The contribution to the leaving radiation due to absorption can be written as:

$$dI_a(f,r) = -k_a(f,r)I(f,r)dr, \tag{1.14}$$

where the negative sign indicates that the variation in spectral radiance due to absorption is negative (it decreases).

1.5.2 Spectral radiance decrease due to scattering

Another part of the energy associated to the radiation entering in the volume is scattered, i.e. diverted to directions different from the original direction of propagation, within the medium and does not leave the volume through the surface $dA(r + \Delta r)$. To describe this process the *volumetric scattering coefficient* of the medium k_s $[Np \cdot m^{-1}]$

is introduced. It is defined as:

$$k_s(f,r) = \frac{dW_s(f,r)}{dAdrP_i(f,r)} = \frac{dI_s(f,r)dAd\Omega df}{dAdrI(f,r)d\Omega df} = \frac{dI_s(f,r)}{drI(f,r)}, \tag{1.15}$$

where, similarly to the absorption case, dW_s represents the elementary power scattered by the volume when a radiation characterized by the flow P_i impinges normally on the surface $dA(r)$. The contribution to the exiting radiation due to scattering can be written as:

$$dI_s(f,r) = -k_s(f,r)I(f,r)dr, \tag{1.16}$$

also in this case the variation in spectral radiance is negative.

Since both absorption and scattering are linear phenomena, it is possible to consider the global effect, the so-called *extinction*, as the sum of those, and to define the *volumetric extinction coefficient* as:

$$k_e = k_a + k_s, \tag{1.17}$$

leading to a global variation of the spectral radiance equal to:

$$dI_e(f,r) = -[k_a(f,r)I(f,r)dr + k_s(f,r)I(f,r)dr] = -k_e(f,r)I(f,r)dr. \tag{1.18}$$

1.5.3 Spectral radiance increment due to thermal emission

Part of the impinging energy absorbed by the medium tends to increase the temperature of the volume itself. To maintain the thermal equilibrium, the volume will emit the same quantity of energy that is absorbed. Assuming local thermal equilibrium inside the propagation medium, so that a value for the temperature T can be defined in every point inside it, the energy balance requirement leads to the Kirchoff's law. The radiance increment due to thermal emission can, thus, be written as:

$$dI_{te}(f,r) = k_a(f,r)J_a(f,r)dr, \tag{1.19}$$

where the thermal emission source $J_a(f,r)$ must be isotropic and equal to the spectral radiance of a black body as expressed in 1.6.

$$J_a(f,r) = B(f,T(r)) = \frac{2h_P f^3}{c^2}\frac{1}{e^{\frac{h_P f}{k_B T(r)}} - 1}. \tag{1.20}$$

1.5.4 Spectral radiance increment due to scattering

Part of the energy propagating through the volume element along directions different from the direction of observation can be diverted by the scattering elements inside the volume and exit in the direction of observation. In this way the spectral radiance measured in the direction of interest is increased of a quantity directly proportional to the scattering coefficient equal to:

$$dI_{sc}(f,r) = k_s(f,r)J_s(f,r)dr, \tag{1.21}$$

expressing with $J_s(f,r)$ the source function. This can be calculated considering the integral on the whole solid angle of any possible propagating radiation $I(r_i)$ weighted by the phase function $\Psi(r,r_i)$ accounting for the coupling, generally non-isotropic, between incident and scattered intensity in every point of the medium:

$$J_s = \frac{1}{4\pi}\int \Psi(r,r_i)I(r_i)d\Omega\ , \tag{1.22}$$

For sake of compactness, the two source function also can be summed up after being weighted by its volumetric coefficients and normalized by the extinction coefficient, leading to one only term representing the total source function J:

$$J = \frac{k_a}{k_e}J_a + \frac{k_s}{k_e}J_s = (1-w)J_a + wJ_s, \tag{1.23}$$

where w is defined as the single scattering albedo coefficient ($w = k_s/k_e$). The total variation of the spectral radiance crossing the volume element can then be expressed as the algebraic sum of the four contributions just described:

$$dI = -k_eIdr + k_eJdr = (J-1)k_edr, \tag{1.24}$$

where the dimensionless product k_edr is usually abbreviated as $d\tau$, the so-called *optical thickness increment*. Equation 1.24 can then be written in a differential form as:

$$\frac{dI}{d\tau} + I = J. \tag{1.25}$$

Once the radiative transfer law is formulated as in Eqn. 1.25, the solution can be easily found considering the case of a semi-infinite medium (as shown in Fig. 1.3) characterized by the extinction coefficient k_e, the total source function J and the boundary spectral radiance $I(0)$ in the direction r.

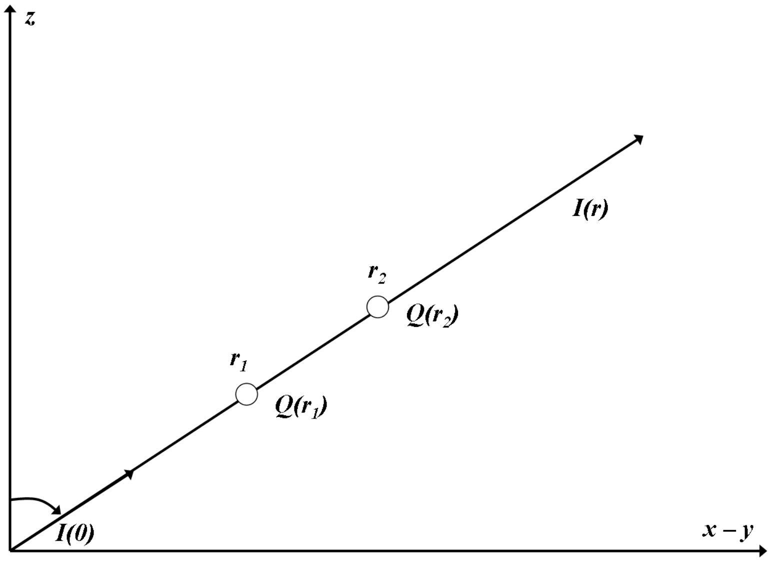

Figure 1.3: Geometry for the radiative transfer equation

With the introduction of the optical thickness for the path between abscissas r_1 and r_2, calculated as:

$$\tau(r_1, r_2) = \int_{r_1}^{r_2} k_e dr, \tag{1.26}$$

the solution of Eqn. 1.25 gives the spectral radiance observed at the abscissa r as:

$$I(r) = I(0)e^{-\tau(0,r)} + \int_0^r k_e(r')J(r')e^{-\tau(r',r)}dr'. \tag{1.27}$$

Equation 1.27 can be interpreted by realizing that the first term represents the boundary spectral radiance that reaches the observation point (r), attenuated by the extinction produced by the medium, whereas the second one describes the sum of infinite contributions of the medium (thermal emission and scattering) produced by the infinitesimal volume of width dr', each one attenuated by the extinction relative to the path between the source (r') and the observation point (r).

The complete solution for the radiative transfer equation in 1.27 when both absorption and scattering are present is very laborious. The most complex part is assessing the emission due to scattering, which needs to consider all the spectral radiances coming from all possible directions. However, in most cases the hypothesis of neglecting the scattering emission can be made ($w \ll 1$), leading to a large reduction of the complexity of the problem. In addition, in the microwave region the Rayleigh-Jeans approximation to the Planck's law (Eqn. 1.7) brings a further simplification to the problem.

In analogy to the definition of brightness temperature (Eqn. 1.11) it is possible to define an apparent radiometric temperature representative of the spectral radiance propagating inside the medium in correspondence of the abscissa r:

$$T_{AP}(f,r) = \frac{I(f,r)c^2}{2kf^2} = \frac{I(f,r)\lambda^2}{2k}. \tag{1.28}$$

Taking into account the definition of T_{AP}, Eqns. 1.20 and 1.22 can be rewritten as:

$$J_a(f,r) = \frac{2kT(r)}{\lambda^2}, \tag{1.29}$$

$$J_s(f,r) = \frac{2kT_{sc}(r)}{\lambda^2}, \tag{1.30}$$

where

$$T_{sc} = \frac{1}{4\pi}\iint_{4\pi} \Psi(r,r_i)T_{AP}(r_i)d\Omega, \tag{1.31}$$

and the solution of the radiative transfer equation (Eqn. 1.27) takes the form:

$$T_{AP}(r) = T_{AP}(0)e^{-\tau(0,r)} + \int_0^r k_e(r')\left[(1-w)T(r') + wT_{sc}(r')\right] e^{-\tau(r',r)}dr' \ , \tag{1.32}$$

where the emission source functions have been explained in terms of equivalent radiometric temperatures. In the case that scattering is not considered (or not present) the solution simplifies into:

$$T_{AP}(r) = T_{AP}(0)e^{-\tau(0,r)} + \int_0^r k_a(r')T(r')e^{-\tau(r',r)}dr' \ , \tag{1.33}$$

and in this case is also:

$$\tau(r',r) = \int_{r'}^r k_a(r'')dr''. \tag{1.34}$$

1.6 Emissivity, reflectivity, and transmissivity

In a medium with an impinging energy flux ϕ_i, three different situations can happen: energy can be reflected, transmitted, and absorbed. Once the thermal equilibrium is reached, all the energy absorbed by the medium will be emitted. In Fig 1.4 the typical scenario of a energy flux impinging on a dielectric medium is shown, ϕ_r, ϕ_t, ϕ_a, and ϕ_e are the reflected, transmitted, absorbed, and emitted fluxes, respectively.

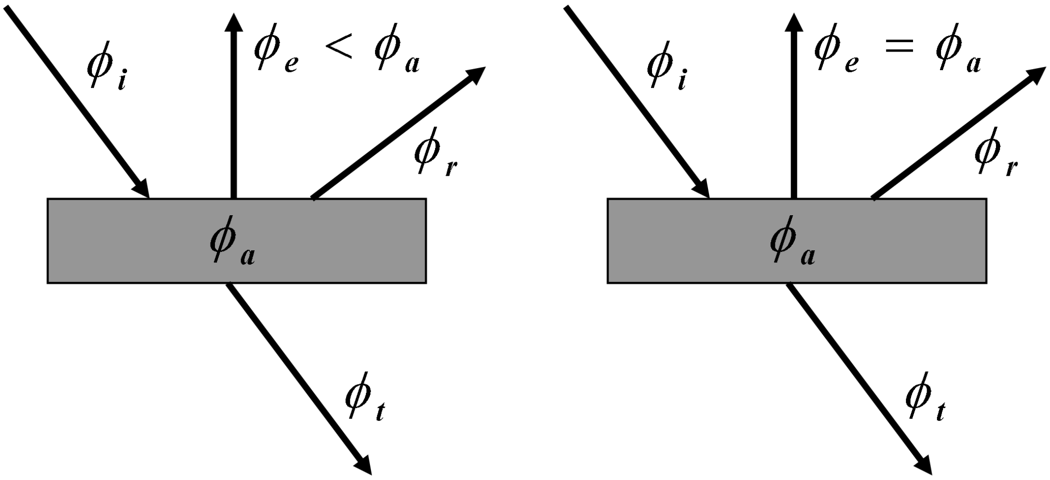

(a) (b)

Figure 1.4: Energy fluxes (a) before and (b) after reaching the thermal equilibrium

The relationship between outgoing and incoming fluxes permits to define the reflectivity (Γ), transmissivity (T), absorptivity (a), and emissivity (e) coefficients as:

$$\Gamma = \frac{\phi_r}{\phi_i}, T = \frac{\phi_t}{\phi_i}, a = \frac{\phi_a}{\phi_i}, e = \frac{\phi_e}{\phi_i}, \tag{1.35}$$

In this case too, the energy conservation law imposes the sum of the incoming fluxes to be equal to the sum of the outgoing ones giving before the thermal equilibrium:

$$\begin{aligned} \phi_i &= \phi_r + \phi_t + \phi_a, \\ 1 &= \Gamma + T + a, \end{aligned} \tag{1.36}$$

and after that ($\phi_e = \phi_a$):

$$\begin{aligned} \phi_i &= \phi_r + \phi_t + \phi_e, \\ 1 &= \Gamma + T + e, \end{aligned} \tag{1.37}$$

The following properties can be evinced:

- The proportion among ϕ_r, ϕ_t, and ϕ_a change for the different bodies on the Earth surface, depending on its material and physical condition.
- The aforementioned parameters depend on the wavelength. Objects that result indistinguishable in a certain spectral interval may be clearly discernible at another frequency. In the visible band these spectral differences translate into the effect of color.

The geometric shape of the object reflecting the energy is also a very important aspect, in particular according to the roughness of its surface an object is considered a:

specular reflector For any incidence direction it exists one and only one direction of reflection, the reflection angle is equal to the incidence one.

ideal or Lambertian scatterer No matter the direction of incidence, the energy is always scattered in all directions.

Most natural surfaces are neither specular reflectors, nor Lambertian scatterers but rather an intermediate situation between them. To classify an object, its roughness must be compared to the incident wavelength. In this sense, a natural surface can be considered plane (behaving like a specular reflector) if the ratio between the surface height rms (σ) and the wavelength λ is much smaller than unity ($\sigma/\lambda \ll 1$) (Fig 1.5a). On the contrary, if $\sigma/\lambda > 1/3$ the surface is considered rough and acts as a Lambertian scatterer (Fig 1.5b). In general the most common situation is that the reflected energy is distributed over all directions, but with a maximum around the specular direction (Fig 1.5c).

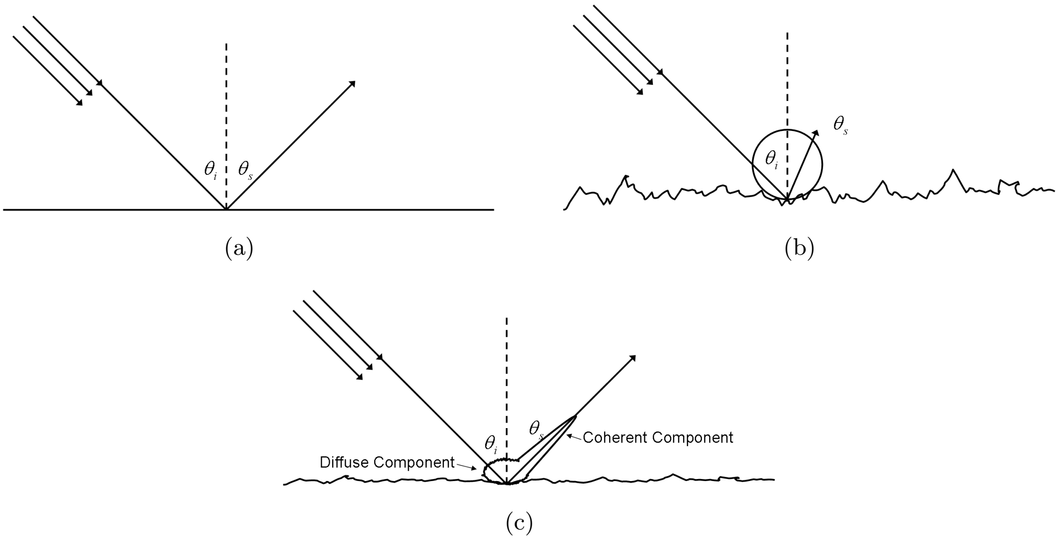

(a) (b) (c)

Figure 1.5: (a) Specular reflector, (b) Lambertian scatterer, and (c) real scatterer

1.7 Scattering

As introduced in the previous paragraph, energy is generally not reflected in just one direction, but it is rather scattered over several directions. If an electromagnetic wave with power P_t is emitted against an object, the reflected radiation power $P_r(\theta,\varphi)$ can be expressed as a function of the direction of observation according to the radar equation (*Ulaby et al.*, 1982):

$$P_r(\theta,\varphi) = \frac{\lambda^2}{(4\pi)^3}\int_A \frac{P_t(\theta,\varphi)G_tG_r}{R_1^2R_2^2}\sigma^0_{rt}\left(\theta_s,\varphi_s;\theta,\varphi\right)dA \tag{1.38}$$

According to Eqn. 1.38, the reflected power P_r depends on the transmitted one (P_t), the distance between the emitter and the scatterer (R_1), the transmitting and receiving antennas gains (G_t, G_s), and a parameter σ^0_{pq} dependent on the object itself as well as on the transmitted (q) and received (p) polarizations. In Fig. 1.6 a typical scenario to describe the radar equation is shown.

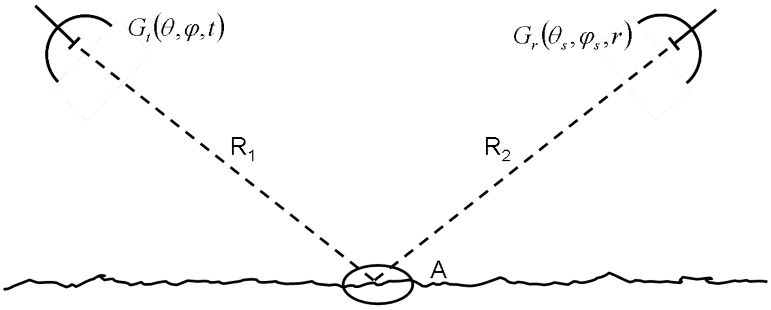

Figure 1.6: Typical scenario to describe the radar equation

The coefficient σ^0_{pq} is called bistatic scattering coefficient and describes the behavior of a certain object with respect to an incident electromagnetic wave. It depends on the direction and polarization of the incident wave (θ,ϕ,q) as well as on the direction and polarization of observation (θ,ϕ,p).

Since (σ^0_{pq}) is not dependent on the measurement system used, it can be defined as a function of the incident and scattered fields, considering that A represents the area illuminated by the incidence field:

$$\sigma^0_{pq}\left(\theta_s,\varphi_s;\theta,\varphi\right) = \frac{4\pi R_1^2|E_p^s|^2}{A|E_q^i|^2}. \tag{1.39}$$

In the same way it is possible to define a scattering coefficient matrix $[S]$ relating the incident and scattered fields for all the possible polarimetric combinations:

$$\begin{bmatrix} E_v^s \\ E_h^s \end{bmatrix} = \frac{e^{-jkR_1}}{R_1} \begin{bmatrix} S_{vv} & S_{vh} \\ S_{hv} & S_{hh} \end{bmatrix} \begin{bmatrix} E_v^i \\ E_h^i \end{bmatrix} \tag{1.40}$$

In Eqn. 1.40 it can be noticed that the incident wave is considered a plane wave (far field), whereas the reflected one is spherical. The unit for the S matrix coefficients are, thus, $m/\sqrt{sr}$, while σ^0 is dimensionless. Considering the definition of the reflectivity in Eqn. 1.35 and taking into account that for an electromagnetic wave incident with an angle θ the area projected is $Acos(\theta)$, Γ can be expressed as:

$$\Gamma_q(\theta,\varphi) = \frac{1}{4\pi cos(\theta)} \iint_{2\pi} \left[\sigma_{qq}^0\left(\theta_s,\varphi_s;\theta,\varphi\right) + \sigma_{pq}^0\left(\theta_s,\varphi_s;\theta,\varphi\right)\right] d\Omega_s \tag{1.41}$$

1.8 Stokes' vector

The polarization of an electromagnetic wave is defined as the geometric figure drawn by the edge of the electrical field $\overrightarrow{E}$ vector in a certain point of the space, looking at the wave moving away from the observer in the direction $\hat{h}$. The electric field vector can be split into vertical E_v and horizontal E_h components so that the reference system $(\hat{k},\hat{v},\hat{h})$ coincide with the spherical reference system $(\hat{r},\hat{\theta},\hat{\varphi})$ as expressed by the Eqn. 1.42

$$E = \left(E_v\hat{v} + E_h\hat{h}\right) e^{-jk\hat{k}r}. \tag{1.42}$$

To fully charecterize the polarization of a certain electromagnetic wave the Stokes vector is used, it is defined as (*Randa et al.*, 2008):

$$F = \begin{bmatrix} I_0 \\ Q \\ U \\ V \end{bmatrix} = \begin{bmatrix} |E_v|^2 + |E_h|^2 \\ |E_v|^2 - |E_h|^2 \\ 2Re(E_vE_h^*) \\ 2Im(E_vE_h^*) \end{bmatrix}. \tag{1.43}$$

In microwave radiometry, the *modified Stokes' vector* (F_m) is usually preferred, since the first and second terms directly describe the vertical and horizontal polarizations, as shown in Eqn. 1.44:

$$F_m = \begin{bmatrix} T_v \\ T_h \\ U \\ V \end{bmatrix} = \begin{bmatrix} \langle E_v E_v^* \rangle \\ \langle E_h E_h^* \rangle \\ 2Re(E_v E_h^*) \\ 2Im(E_v E_h^*) \end{bmatrix} . \tag{1.44}$$

Depending on the situation the emissivity Stokes' vector can also be used:

$$\begin{bmatrix} T_v \\ T_h \\ T_U \\ T_V \end{bmatrix} = T_0 \begin{bmatrix} e_v \\ e_h \\ e_U \\ e_V \end{bmatrix} = C \begin{bmatrix} \langle E_v E_v^* \rangle \\ \langle E_h E_h^* \rangle \\ 2Re(E_v E_h^*) \\ 2Im(E_v E_h^*) \end{bmatrix} , \tag{1.45}$$

where T_0 is the physical temperature of the body, and C is an adequate constant. This latter permits to fully characterize the emissivity behavior of an object and, eliminating the direct dependence on the surface temperature, which sometimes easies the analysis.

Taking into account Eqns. 1.36, 1.37, and 1.41 and considering an semi-infinite body ($T = 0$), the emissivity can be expressed as:

$$e_q(\theta, \varphi) = 1 - \frac{1}{4\pi cos(\theta)} \iint_{2\pi} \left[\sigma_{qq}^0 (\theta_s, \varphi_s; \theta, \varphi) + \sigma_{pq}^0 (\theta_s, \varphi_s; \theta, \varphi) \right] d\Omega_s \ , \tag{1.46}$$

where subindices q and p stand for the transmitted and scattered polarizations (usually horizontal (h) or vertical (v) polarizations).

If a unitary incident field is considered, then the bistatic scattering coefficient can be expressed as a function of only the scattered field (Eqn. 1.39 and 1.40). In this way, omitting the dependence on the incidence and scattering angles, the elements of the emissivity Stokes' vector (Eqn. 1.45) become:

$$\begin{bmatrix} e_v \\ e_h \end{bmatrix} = 1 - \frac{R^2}{Acos\theta} \iint_{2\pi} \begin{bmatrix} |E_{vv}|^2 + |E_{vh}|^2 \\ |E_{hv}|^2 + |E_{hh}|^2 \end{bmatrix} d\Omega_s \tag{1.47}$$

$$\begin{bmatrix} e_U \\ e_V \end{bmatrix} = - \frac{R^2}{Acos\theta} \iint_{2\pi} \begin{bmatrix} 2Re \left(E_{vh} E_{hh}^* + E_{vv} E_{hv}^* \right) \\ 2Im \left(E_{vh} E_{hh}^* + E_{vv} E_{hv}^* \right) \end{bmatrix} d\Omega_s \tag{1.48}$$

where $E_{pq} = \frac{E_p^s}{E_q^i}$, the ratio between the scattered field at p polarization and the incident at q polarization.

1.9 Conclusions

The basics concepts of microwave radiometry have been introduced in this chapter to easy the comprehension of the thesis. Nevertheless, considering the quantity and complexity of the subjects involved, references have been added, which allow a deeper understanding of the topic. Several forward emission models have been derived based on these theories, in the next chapter the currently most commonly used forward emission models at L-band will be briefly reviewed.

2

Emissivity models at L-band

This chapter is devoted to a quick review of the most consensuated and widely used forward emissivity models at L-band. A complete discussion would need a deep introduction to Physics, Chemistry, and Oceanography, which is considered out of the scope, so just the main concepts are introduced, leaving the details to the avaible referenced documents. To introduce the problem, a simple schematic scenario is presented in section 2.1, models are detailed in the following sections, starting with the sea surface (section 2.2), the atmosphere (section 2.3), the ionosphere (section 2.3), and, finally, the rotation from the Earth to the antenna reference frame (section 2.5).

2.1 Example of remote sensing scenario

To clearly explain the approach followed in the definition of the SMOS level 2 retrieval algorithm, a typical passive remote sensing scenario is considered (Fig. 2.1). It can be observed as the energy measured by the radiometer is not coming from the Earth's surface only, but is the sum of several contributions, each of these contributions is dependent on the geometric shape and the physical situation of the measured object as well as on the observation frequency. All these variables must be well known and correctly estimated to guarantee the good result of the geophysical parameter retrieval.

The total radiation measured by the radiometer is expressed in Eqn. 2.1

$$\begin{aligned} T_{AP} &= e^{-\tau}\left(T_B + \left(e^{-\tau}T_{COS} + \Gamma T_{DN}\right)\right) + T_{UP} = \\ &\quad e^{-\tau}T_B + e^{-2\tau}T_{COS} + \Gamma e^{-\tau}T_{DN} + T_{UP}. \end{aligned} \tag{2.1}$$

The radiation is given by the sum of:

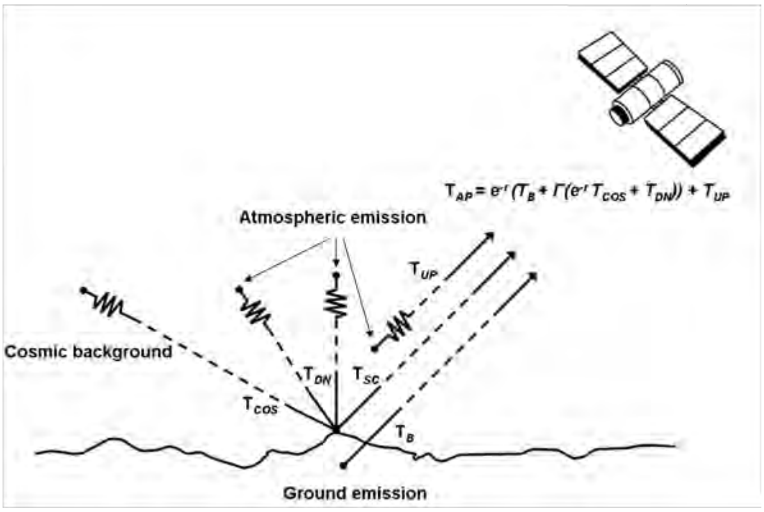

Figure 2.1: Typical passive remote sensing scenario - The radiation comes from several different sources

- the surface's contribution (T_B) attenuated by the atmospheric opacity ($e^{-\tau}$).
- the direct atmospheric contribution attenuated in the path from the source to the radiometer (T_{UP}).
- the direct atmospheric contribution attenuated in the path from the source to the Earth's surface (T_{DN}), then reflected (Γ), and attenuated again according to the atmosphere opacity ($e^{-\tau}$).
- the cosmic background (T_{COS}) reflected by the Earth's surface (Γ) and attenuated twice by the atmospheric opacity $\left(e^{-2\tau}\right)$.

Each contribution is addressed in more details in the next sections.

2.2 Sea surface emission at L-band

So far, several models have been developed to estimate the emission of the sea surface at L-band as a function of different key physical variables, such as the temperature, the salinity, and the roughness, as well as the presence of sea foam. In this section a brief introduction to the most representative ones are presented.

2.2.1 Flat sea

The simplest case is a smooth, calm sea surface. In this case the brightness temperature T_B is simply defined by the Fresnel's Law (*Ulaby et al.*, 1982) in terms of specular reflectivity $\Gamma^{sp}(f,\theta,p)$ as a function of the frequency (f), the incidence angle (θ), the polarization (p), and the physical temperature (SST):

$$T_B(f,\theta,p) = e^{sp}(f,\theta,p)SST = \left[1-\Gamma^{sp}(f,\theta,p)\right]SST, \qquad (2.2)$$

where, if the dielectric constant of sea water is expressed as ε_w; the specular reflectivity for the horizontal $(p=h)$ and vertical $(p=v)$ polarizations is respectively:

$$\Gamma^{sp}(f,\theta,h) = \left|\frac{cos\theta - \sqrt{\varepsilon_w - sin^2\theta}}{cos\theta + \sqrt{\varepsilon_w - sin^2\theta}}\right|^2, \qquad (2.3)$$

and

$$\Gamma^{sp}(f,\theta,v) = \left|\frac{\varepsilon_w cos\theta - \sqrt{\varepsilon_w - sin^2\theta}}{\varepsilon_w cos\theta + \sqrt{\varepsilon_w - sin^2\theta}}\right|^2. \qquad (2.4)$$

For what concerns the sea water dielectric constant the Klein and Swift model (*Klein and Swift*, 1977) is generally used even though several new models are available, such as Ellison et al. (*Ellison et al.*, 1998) above C-band, the recent one by Blanch and Aguasca (*Blanch and Aguasca*, 2004) and the one by Meissner and Wentz (*Meissner and Wentz*, 2004) at L-band. Figure 2.2 shows the brightness temperature dependence on the observation angle for both $h-$ and $v-$polarizations of a perfectly flat sea surface considering a sea surface temperature of SST=20 $°C$ and a sea surface salinity of SSS=36 psu.

2.2.2 Roughened foam-free sea

The presence of wind strongly affects the sea surface emission: it causes waves and, above certain speeds, foam. Neglecting the foam contribution, which will be assessed later, in this paragraph a short overview of the most frequently used models for roughened sea emission is presented.

The Kirchoff method A first approach to the estimation of the sea emission (or any general surface emission) is considering the random sea surface as the sum of infinite planes, each plane tangent to the surface in the point of incidence between the radiation and the surface. These planes are generally called *facets* and this idea is usually referred

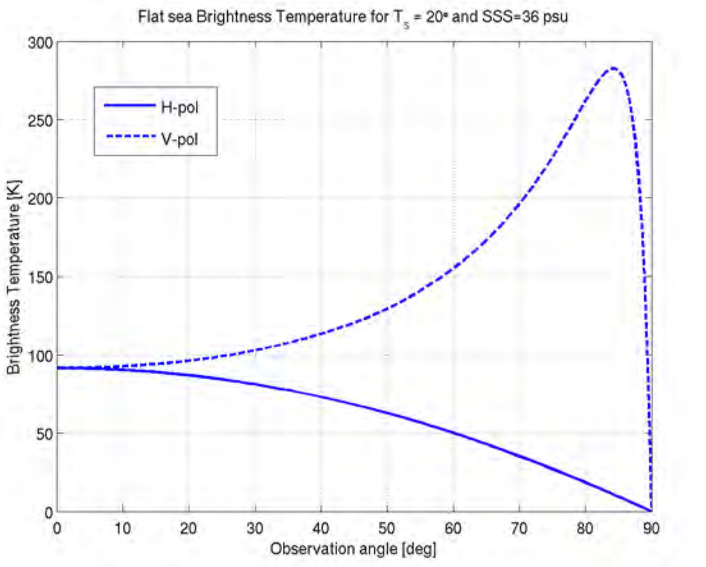

Figure 2.2: Brightness temperature dependence on the observation angle for a perfectly flat sea surface

as the Kirchoff, or Physical Optics, method (*Ulaby et al.*, 1982). The application of this technique is bind to the fulfilling of the following two conditions:

- in the horizontal dimension the correlation length l must be larger than the wavelength λ of the incident electromagnetic field;
- in the vertical dimension the surface's height standard deviation σ_η must be small compared to the wavelength λ.

These two conditions can be written as:

$$kl > 6, \tag{2.5}$$

and

$$r_c > \lambda, \tag{2.6}$$

where $k = 2\pi/\lambda$ is the wave number and r_c the curvature radius of the surface, that for a Gaussian surface is:

$$r_c = \frac{l^2}{2\sigma_\eta}\sqrt{\frac{\pi}{6}}. \tag{2.7}$$

On the other hand, the Kirchoff method cannot be used in case of very small roughness. The surface must have the minimum height standard deviation to satisfy:

$$k\sigma_\eta > 0.3. \tag{2.8}$$

Given these validity conditions, when applying the Kirchoff method to arbitrary roughened surfaces the analytical evaluation is still difficult to carry out and further simplyfing assumptions must be done. In case of large standard deviation of the surface height the *Stationary-Phase* approximation is used, which considers scattering only in the specular direction, whereas if the surface height standard deviation is medium or low and the surface has small slopes the *Scalar Approximation* is applied.

The Small Perturbation Method The Small Perturbation Method (SPM) (*Ulaby et al.*, 1982) is used when both the rms height and the correlation length are smaller than the wavelength of the incident field. In this case the analysis is much simpler and the first order approximation for the bistatic scattering coefficients can be used instead of the complete expression.

The Integral Equation Method The Integral Equation Model (IEM) (*Fung*, 1994) was developed to cover the range where neither the Kirchoff method nor the SPM give accurate results. Furthermore it reduces to Kirchoff-SP or to the SPM according their validity ranges. The most important approximation of the IEM is the use of the global incidence angle instead of the local one when Fresnel's coefficients are computed. The accuracy of this approach depends basically on the statistical parameters of the surface roughness and the autocorrelation function.

The Small Slope Approximation The Small Slope Approximation (SSA) described and tested in (*Irisov*, 1997), (*Johnson and Zhang*, 1999), and (*Reul et al.*, 2001) has demonstrated to give results as good as the SPM ones when applied to describe the thermal emission of a roughened surface. In addition to that the SSA approach compared to the SPM one presents the advantage of being only constrained on slope and not on height, making the model applicable to the entire ocean surface.

The Two Scale Model Applyng a Two Scale Model (TSM) was firstly proposed by Yueh in (*Yueh*, 1997) and a version tuned at L-band can be found in (*Dinnat et al.*, 2003). The sea surface is approximated by a two-scale surface with small-scale ripples or capillary waves on the top of large-scale surfaces. With this approximation, the total thermal emission from the surface is the sum of emissions from individual, slightly perturbed surface patches tilted by the underlying large-scale surface. Bragg's scattering mechanism is applied for assessing the contribution of the small-scale waves that are considered modulated according to the geometric optics by the large-scale ones. The two-scale approach gives good results in terms of numerical accuracy, nevertheless, being its "real accuracy" (performance in describing the reality) basically depending on the sea surface model and electromagnetic scattering theories, several parameters and configurations have been tested and results are very different depending on that choice.

2.2.3 Roughened foamy surface

Above certain speed (typically considered around 7 m/s) the wind, apart from increasing the sea surface roughness, also creates foam on its surface. The foam has different spectral characteristics from sea water and strongly affects the total emission of the sea surface. For partially foam covered sea surfaces, according to (*Yueh*, 1997) and (*Camps et al.*, 2005b), the emission is given by the simple weighted mean of the foam emissivity and the sea water one, as shown in Eqn. 2.9:

$$e(f,\theta,p,F) = (1-F)e_w(f,\theta,p) + Fe_f(f,\theta,p), \tag{2.9}$$

where F is the fractional foam coverage, e_w the emissivity of the wind roughened sea water, and e_f the emissivity of a totally foam-covered surface. F is generally estimated as function of the forces acting on the sea surface (expressed as wind speed or wind stress) and the resistance of the water to these forces (*viscosity*), which is function of the temperature and salinity.

2.2.4 Empirical models

Apart from the theoretical models, several empirical models have been also developed to describe the roughness effect of the sea surface emission at L-band. The first approximation, valid for all the empirical models, is to consider the total roughened sea surface brightness temperature emitted as the sum of the flat-sea brightness temperature and a contribution only due to roughness, as shown in Eqn. 2.10:

$$T_{B,p}(\theta, SST, SSS, U_{10}) = e_p(\theta, SST, SSS)SST + \Delta T_{B_{rough},p}(\theta, roughness) \tag{2.10}$$

where e_p is the flat-sea emissivity at p polarization, and θ is the incidence angle. The contribution $\Delta T_{B_{rough},p}$ can change according to the model used and it is generally function of the incidence angle and of one or more wind-related geophysical parameters such as 10-meter heigh wind speed (U_{10}), Significant Wave Height (SWH), or Mean Square Slope of waves (MSS) ...

Hollinger measurements derived model

One of the first empirical models used in literature is the linear regression of the measurements performed by Dr. Hollinger and his colleagues in 1970, published in (*Hollinger*, 1971). During the month of March 1970 Dr. Hollinger and his team measured the effect of the surface roughness on the sea surface brightness temperature at 1.41, 8.36, and 19.34 GHz. Measurements were acquired from the Argus Island tower, South-West of Bermuda, and under several different weather conditions (U ranging from 0 to 15 m/s measured at 43.3 m over the sea level). Measurements collected by Dr. Hollinger and his colleagues are reported in Fig. 2.3 as presented in *Hollinger* (1971). Measurements of the brightnes temperature on the (top) vertical and (bottom) horizontal polarizations, acquired at 1.41, 8.36, and 19.34 GHz, are shown for left to right as a function of the average wind speed. The solid lines are the result of a least square fitting applied to these.

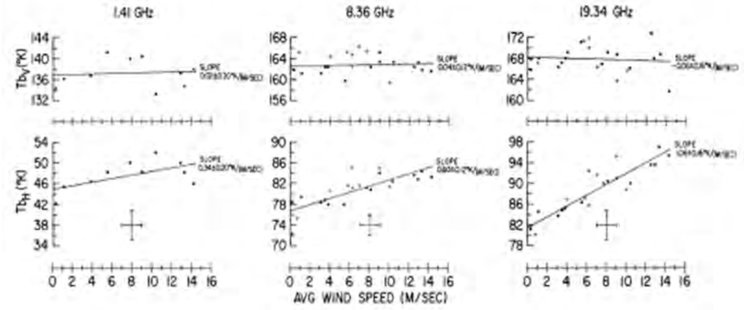

Figure 2.3: .

]Brightnes temperature on the (top) vertical and (bottom) horizontal polarizations, acquired at (left) 1.41, (center) 8.36, and (right) 19.34 GHz as a function of the average wind speed. Solid lines are the result of a least square fitting applied to the measurements [from *Hollinger* (1971)].

Based on this measurements, the effect of roughness on the brightness temperature can be expressed as a linear function of the wind speed and of the incidence angle, as in Eqns. 2.11 and 2.12.

$$\Delta T_{Bh} = 0.2 \left(1 + \frac{\theta}{55^{\circ}}\right) U \tag{2.11}$$

$$\Delta T_{Bv} = 0.2 \left(1 - \frac{\theta}{55^\circ}\right) U \qquad (2.12)$$

WISE derived models

In 2000 and 2001, sponsored by ESA, the WInd and Salinity Experiment (WISE) (*Vall-llossera et al.* (2003), *Camps et al.* (2004a), and *Camps et al.* (2004b)) was carried out on the Casablanca oil rig in the Mediterranean sea, just in front of the city of Tarragona. Measurements were collected over incidence angles ranging from 25° to 65° (with 5-degree steps), the sea surface temperature ranging between 16 and 22 °C and the wind speed between 0 and 15 m/s. For each of the steps in incidence angle, a linear regression was calculated assuming the brightness temperature depending on the wind speed and on the significant wave height, as shown in Fig. 2.4 (Fig. 6 of *Camps et al.* (2004b)). In Fig. 2.4 the brightness temperatures in the (top) horizontal and (center) vertical polarizations for an incidence angle of 20° to 65° are shown. The sensitivity of the brightness temperature to the the wind speed is shown in the bottom plot.

A linear fitting was then applied to these coefficients and the model resulting is expressed in Eqns. 2.13 and 2.14 as a function of wind speed, and in Eqns. 2.15 and 2.16 as a function of the significant wave height.

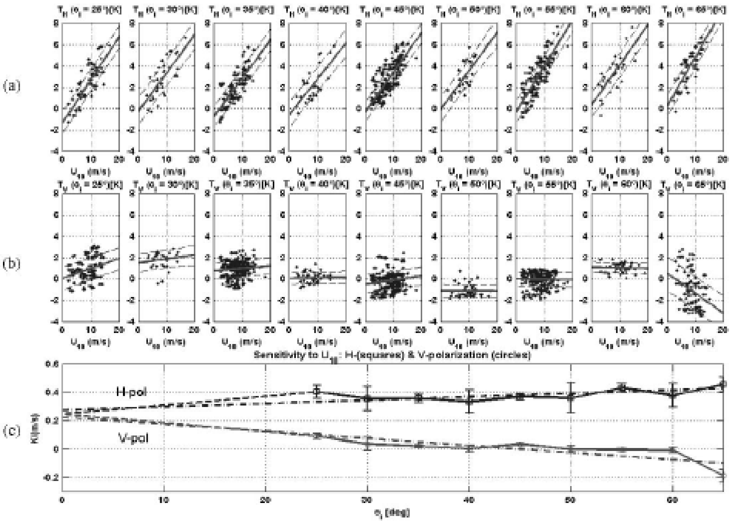

Figure 2.4: Brightness temperatures in the (top) horizontal and (center) vertical polarizations for an incidence angle of 20 to 65 degrees. The bottom plot summarize the sensitivity of the brightness temperature to the wind speed.

$$\Delta T_{Bh} = 0.25\left(1+\frac{\theta}{118^\circ}\right)U_{10} \tag{2.13}$$

$$\Delta T_{Bv} = 0.25\left(1-\frac{\theta}{45^\circ}\right)U_{10} \tag{2.14}$$

$$\Delta T_{Bh} = 1.09\left(1+\frac{\theta}{142^\circ}\right)SWH \tag{2.15}$$

$$\Delta T_{Bv} = 0.92\left(1-\frac{\theta}{51^\circ}\right)SWH \tag{2.16}$$

In Fig. 2.5 the two models depending on the wind speed (*Hollinger*, 1971) and (*Camps et al.*, 2004b) are compared for an incidence angle ranging from 0 to 90 degrees and a wind speed of 5, 10 , and 15 m/s

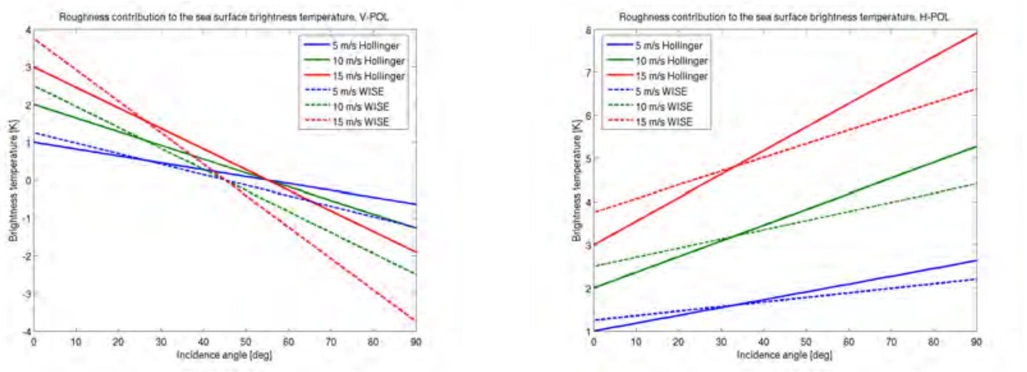

(a)

(b)

Figure 2.5: Comparison between the (solid) Hollinger measurements and the (dashed) WISE derived models. (a) V- and (b) H-polarizations

Gabarró et al. model

From the same WISE campaign another model assuming double dependency of the brightness temperature on both wind speed and significant wave height was proposed by Dr. Gabarró and her colleagues (*Gabarró et al.*, 2004). The resulting formulas are reported in Eqns. 2.17 and 2.18:

$$\Delta T_{Bh} = 0.12\left(1+\frac{\theta}{24^\circ}\right)U_{10} + 0.59\left(1+\frac{\theta}{50^\circ}\right)SWH, \tag{2.17}$$

$$\Delta T_{Bv} = 0.12 \left(1 - \frac{\theta}{40^\circ}\right) U_{10} + 0.59 \left(1 + \frac{\theta}{50^\circ}\right) SWH. \tag{2.18}$$

Following this approach the currently used empirical model for the SMOS mission has been derived (*Zine et al.*, 2008). It is linearly dependent on 5 geophysical parameters, describing different phenomena affecting the sea surface roughness, namely: wind speed (U_{10}), significant wave height *(SWH)*, inverse wave age (Ω), wind friction velocity (U^*), and mean square slope of the waves *(MSS)*. Some of these are proportional to a certain power of the wind speed, introducing in this way a higher grade dependence in the function. Three models are defined according to the wind speed (model 1 for $U_{10} < 3m/s$; model 2 for $3 < U_{10} < 12m/s$; model 3 for $U_{10} > 12m/s$), for each model different C and D array of coefficients are used, as described in Eqn. 2.19, where x is the model (1,2,3) and z .

$$\begin{aligned} \Delta T_{Bh} &= (C_{x,1,z} + D_{x,1,z}\theta_i)\, U_{10} + (C_{x,2,z} + D_{x,2,z}\theta_i)\, SWH + \\ &\quad + (C_{x,3,z} + D_{x,3,z}\theta_i)\, \Omega + (C_{x,4,z} + D_{x,4,z}\theta_i)\, U^* + \\ &\quad + (C_{x,5,z} + D_{x,5,z}\theta_i)\, MSS, \\ \Delta T_{Bv} &= (C_{x,1,z} + D_{x,6,z}\theta_i)\, U_{10} + (C_{x,2,z} + D_{x,7,z}\theta_i)\, SWH + \\ &\quad + (C_{x,3,z} + D_{x,8,z}\theta_i)\, \Omega + (C_{x,4,z} + D_{x,9,z}\theta_i)\, U^* + \\ &\quad + (C_{x,5,z} + D_{x,10,z}\theta_i)\, MSS. \end{aligned} \tag{2.19}$$

C and D will be defined using SMOS measurements and in situ data collected during the Commissioning Phase.

2.3 Atmospheric contribution

L-band radiometric measurements are generally not very sensitive to atmospheric conditions. As shown in Fig. 2.6, the trasmissivity is in fact very high in this particular range of the microwave spectrum and, for some applications, it can be considered even transparent. Nevertheless, when the goal is so challenging as in SMOS (retrieving 1-psu *SSS* firm in a single overpass [cfr. chapter. 3]), this contribution cannot be neglected.

In clear air conditions, microwaves are absorbed primarly by oxygen and water vapor, for both of them resonant frequencies are quite far from the L-band (60 GHz and 118.75 GHz for the O_2 and 22.235 GHz and 183.31 GHz for the water vapor), nevertheless the sum of their cues can reach the non-negligible equivalent of 2 Kelvins at 1.4 GHz.

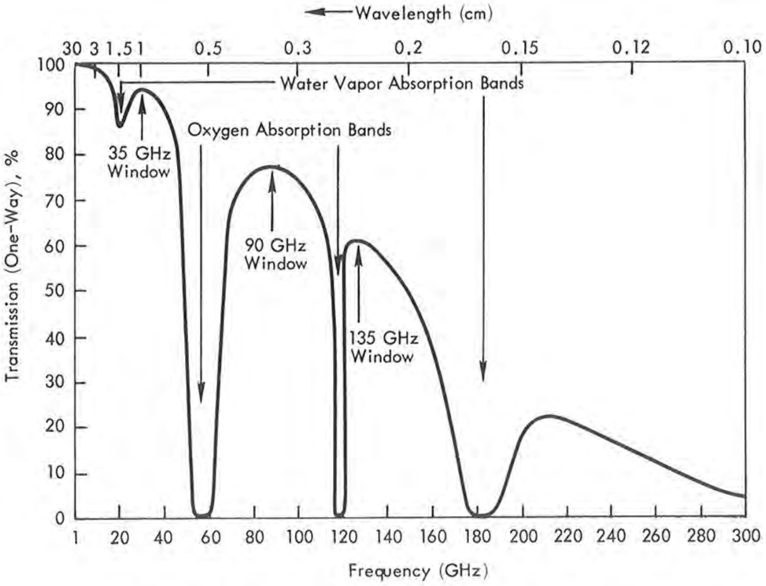

Figure 2.6: Transmissivity of the atmosphere as a function of the frequency (*Ulaby et al.*, 1982)

When rain events occur, rain drops and clouds interact with the microwave radiation. The effect of clouds and rains and its contribution to the total emission is shown in Fig. 2.7 as a function of the layer thickness. As can be noticed, until 2- 5-km thickness the effect of clouds and rain consists of an increasing of the brightness temperature (the so-called *brightening*), whereas if the clouds layer is thicker than that, the contribution becomes negative (*darkening*).

To include the atmosphere in the apparent temperature (cfr. 1.28, 1.32, and 1.33) calculation, the radiative transfer theory must be applied as explained in section 1.5. Following this approach and considering a non-scattering atmosphere, the elemental volume dV is caracterized by the absorption coefficient $k_a(z)$, expressed as a function of the height. The factor k_a permit to calculate the optical thickness of the medium τ_{atm} and the attenuation coefficient for a wave propagating from z_1 and z_2 (L) as:

$$\tau(z_1, z_2) = \int_{z_1}^{z_2} k_a(z) dz, \tag{2.20}$$

$$L(\theta, z_1, z_2) = e^{\tau(z_1, z_2) sec(\theta)}, \tag{2.21}$$

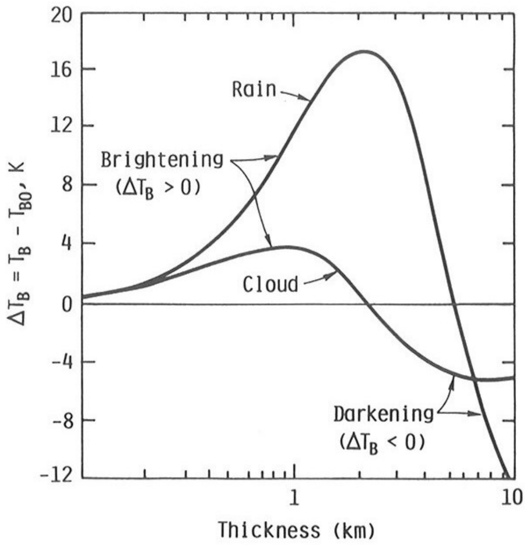

Figure 2.7: Brightening and darkening effects as a function of layer thickness for clouds and rain models at 94 GHz (*Ulaby et al.*, 1982)

and the brightness temperature emitted T_B in the same volume as:

$$T_B(\theta, z_1, z_2) = sec(\theta) \int_{z_1}^{z_2} k_a(z) T(z) e^{-\tau(z_1,z_2) sec(\theta)} dz, \tag{2.22}$$

where θ is the zenith angle, $T(z)$ is the physical temperature at the height z. The brightness temperature T_B is emitted in the $\overrightarrow{z_1 z_2}$ direction.

In the same way, two different brightness temperature can be defined, namely the *upwelling* (T_{UP}) and *downwelling* (T_{DN}) brightness temperatures, considering the volume from the Earth's surface to the point of observation in the first case and the one from the upper limit of the atmosphere to the same point in the second one. Equations 2.23 and 2.24 express this concept, defining H the height of the point of observation:

$$T_{UP}(\theta, H) = sec(\theta) \int_{0}^{H} k_a(z) T(z) e^{-\tau(z,H) sec(\theta)} dz, \tag{2.23}$$

$$T_{DN}(\theta, H) = sec(\theta) \int_{H}^{\infty} k_a(z) T(z) e^{-\tau(H,z) sec(\theta)} dz. \tag{2.24}$$

Considering the case of observing the Earth's surface from a satellite, the apparent temperature collected by the satellite in the unrealistic situation of measuring only the atmosphere is given by Eqn. 2.25:

$$T_{ap}(\theta) = T_{UP}(\theta, \infty) + [\Gamma_{surf} \cdot T_{DN}(\theta, 0)] \cdot L(\theta, 0, \infty). \tag{2.25}$$

Generally, within the atmospheric contribution, the cosmic radiation is also included as an additional term to the T_{DN} expression, which becomes $T_{DN} + T_{COS}e^{-\tau(0,\infty)sec\theta}$ leading to a new apparent temperature:

$$T_{ap}(\theta) = T_{UP}(\theta, \infty) + \left[\Gamma_{surf} \cdot \left(T_{DN}(\theta, 0) + T_{COS}e^{-\tau(0,\infty)sec\theta}\right)\right] \cdot L(\theta, 0, \infty), \tag{2.26}$$

As a first consideration, the "∞" in Eqn. 2.24 - 2.26 can be substituted by 32 km without loss of accuracy, being the atmosphere at this height so ***rarefact*** to be harmlessly considered transparent (*Ulaby et al.*, 1982). Entering in the details of the atmospheric and cosmic microwave emission modelling is considered out of the scopes of this thesis so that only the general reference of (*Ulaby et al.*, 1982) is given in this context. In the case of SMOS, the models used in the level 2 inversion for both atmosphere and cosmic radiation can be found in (*Zine et al.*, 2008).

2.4 Ionospheric contribution

The ionosphere is the most external layer of the atmosphere, it entends from a height of about 50 km to more than 1000 km. The gas density is very low in the ionosphere, and when the solar radiation (mainly ultraviolet and X-ray radiation) succeeds in ionizing gas molecules, the probability of reversing the process (recombination) is very weak. The lack of recombination leads to the creation of the so-called "plasma". Being due to solar radiation, ionosphere presents both a diurnal and seasonal cycles. The amount of ionization is measured in number of free-electrons along a path between two points (TEC - Total Electrons Content) and is expressed in TECU (TEC Unit = 1016 electrons / m^2).

MAPAS TEC SMOS

Ionosphere ionization produces anisotropies in the refraction index of the medium, which causes attenuation (and then emission) and the rotation of the polarization plane of the crossing wave.

Ionosphere also sum its contribution to the final emission measured at L-band, it has effect on both the modulus and the phase of the signal, and, as enphasized in *Le Vine and Abraham* (2002), even though the dominant effect is on the phase, ionospheric emission can be important.

2.4.1 Attenuation and emission

The atenuation induced by ionosphere can be described by an optical thickness (τ_{io}) expressed as in Eqn. 2.27:

$$\tau_{io}(h) = \int_0^h \beta(z)dz, \tag{2.27}$$

being h the height, and β, derived by the Appleton-Hartree equation, equal to:

$$\beta = \frac{2\pi}{\lambda} \cdot \left[\frac{1}{2} \left(\frac{1}{2\pi f} \sqrt{\frac{Ne^2}{\epsilon_0 m}} \right)^2 \frac{\nu}{2\pi f} \right] \cdot \left[1 + \frac{1}{2} \left(\frac{1}{2\pi f} \sqrt{\frac{Ne^2}{\epsilon_0 m}} \right)^2 \right] \tag{2.28}$$

In Eqn. 2.28 $\lambda = c/f$ is the electromagnetic wavelength, c is the speed of light in vacuum, f is frequency, N, e, and m the number, charge, and mass of the electron, respectively, and finally ν is the electron collision frequency.

The aforementioned τ_{io} can be included in the brightness temperature calculations as for the atmospheric contribution, producing the attenuation ΔT_B (Eqn. 2.29) and the upwards and downwards contributions (T_{io}^{up} and T_{io}^{dn}, respectively Eqns. 2.30 and 2.31):

$$\Delta T_B(\theta) = T_0 \left[1 - exp\left(-\tau sec(\theta) \right) \right], \tag{2.29}$$

$$T_{io}^{dn} = \int_0^h T_{io}(z) 2\beta(z) \cdot exp\left[-sec(\theta) \int_0^x 2\beta(x)dx \right] dz, \tag{2.30}$$

$$T_{io}^{up} = \int_0^\infty T_{io}(z) 2\beta(z) \cdot exp\left[-sec(\theta) \int_0^x 2\beta(x)dx \right] dz, \tag{2.31}$$

The total ionospheric contribution has been estimated in *LeVine and Abraham* (2002) and can reach up to 0.055 K.

2.4.2 Faraday rotation

The most important consequence of the anisotropy of the refraction index is the phase shifting that induces in a wave crossing the medium, this shifting is proportional to the TEC accoding to:

$$\begin{bmatrix} T_h^*(\Omega_F) \\ T_v^*(\Omega_F) \end{bmatrix} = \begin{bmatrix} cos^2(\Omega_F) & sin^2(\Omega_F) \\ sin^2(\Omega_F) & cos^2(\Omega_F) \end{bmatrix} \times \begin{bmatrix} T_h \\ T_v \end{bmatrix} \tag{2.32}$$

being Ω_F defined as:

$$\Omega_F = \frac{\pi}{c \cdot f^2} \int \left(\frac{1}{2\pi f} \sqrt{\frac{Ne^2}{\epsilon_0 m}} \right)^2 \frac{eB}{2\pi m} cos(\theta_B(s)) ds \tag{2.33}$$

Variables in Eqn. 2.33 are defined as in Eqn. 2.28, B is the magnetic field strength, and θ_B is the angle between the magnetic field vector and the wave vector. According to *LeVine and Abraham* (2002), the impact of Faraday rotation on the brightness temperature can reach up to 2 K (at noon and at an incidence angle of 50°). Faraday rotation is considered in SMOS data processing as presented in (*The SMOS L2OS Team*) and (*Ribo and Martin-Neira*, 2004).

2.5 Geometric rotation

The last step in order to obtain the brightness temperatures as measured by a satellite-based radiometer is the change of reference frame. Being due just to the misallignment between the plane tangent to the Earth's surface in the emission source point and the antenna plane, it is a pure geometrical problem completely described by the attitude vector of the satellite.

Faraday and geometric rotations are approached in SMOS as a unique rotation, assuming perfect knowledge of the TEC. A schematic view of the problem is shown in Fig. 2.8 (*Waldteufel and Caudal*, 2002):

In Fig. 2.8 the points $\boldsymbol{S}$, $\boldsymbol{O}$, and $\boldsymbol{P}$ indicate the satellite, its projection on the Earth surface, and the observed point, respectively. The antenna frame is referred as $\boldsymbol{XYZ}$ with the origin in $\boldsymbol{S}$, and characterized by the tilt angle t, while the Earth-frame, defined by the geometry of the observation, is represented by the $\left(E_H, E_V, \overrightarrow{PS}\right)$ axis. According to *Claassen and Fung* (1974) the passage from the $\mathbf{E}_\theta \mathbf{E}_\phi$ to the $\mathbf{E_H E_V}$ frame can be obtained through a rotation by an angle ψ around the axis $\overrightarrow{PS}$. The angle ψ is calculated as:

$$\psi = \arcsin \left[\frac{\cos t \sin \theta_g - \sin t \cos \theta_g \sin \phi_g}{\sin \theta} \right]. \tag{2.34}$$

Once $\mathbf{E}_\theta$ and $\mathbf{E}_\phi$ are calculated, the coordinates θ and ϕ can be computed using Eqns. 2.35 and 2.36 (*Waldteufel and Caudal*, 2002):

$$\theta = \arccos \left[\sin t \sin \theta_g \sin \phi_g + \cos t \cos \theta_g \right], \tag{2.35}$$

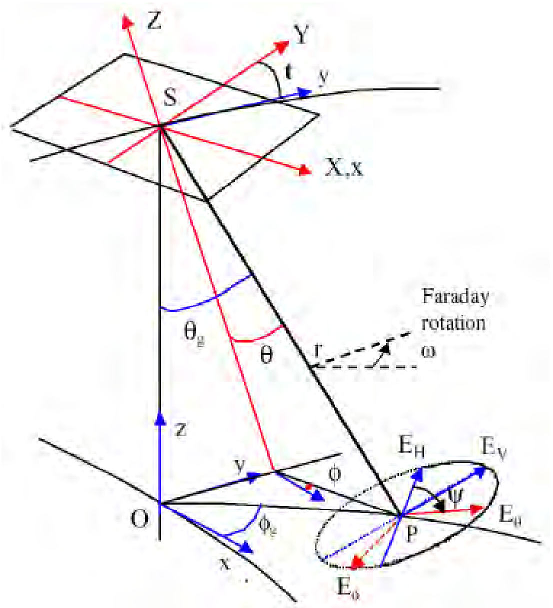

Figure 2.8: Schematic view of the rotation passing from Earth to Antenna reference frame (*Waldteufel and Caudal*, 2002)

$$\phi = -\arcsin\left[-\frac{\sin t\cos\theta_g + \cos t\sin\theta_g\sin\phi_g}{\sin\theta}\right]. \tag{2.36}$$

The angle ψ is applied to the electric field in the reference frame as expressed by Eqn. 2.37:

$$\begin{bmatrix} E_X \\ E_Y \end{bmatrix} = \begin{bmatrix} \cos\psi & -\sin\psi \\ \sin\psi & \cos\psi \end{bmatrix} \cdot \begin{bmatrix} E_H \\ E_V \end{bmatrix}. \tag{2.37}$$

If brightness temperatures are considered instead of electric field, the square power of the rotation matrix must be calculated, the complete rotation matrix for the Full Polarization mode is expressed in Eqn. 2.38, for Dual Polarization mode is sufficient to take the 2-by-2 upper corner of the matrix.

$$\begin{bmatrix} T_X \\ T_Y \\ T_3^* \\ T_4^* \end{bmatrix} = \begin{bmatrix} \cos^2\psi & \sin^2\psi & -\cos\psi\sin\psi & 0 \\ \sin^2\psi & \cos^2\psi & \cos\psi\sin\psi & 0 \\ \sin 2\psi & -\sin 2\psi & \cos 2\psi & 0 \\ 0 & 0 & 0 & 1 \end{bmatrix} \cdot \begin{bmatrix} T_H \\ T_V \\ T_3 \\ T_4 \end{bmatrix}. \tag{2.38}$$

2.6 Conclusions

A quick review of the most accepted and used forward emissivity models at L-band has been carried out in this chapter. Only the main concept have been sketched to give to the reader a quick but overall view of the topic, more detailed analysis have been left to the avaible referenced documents.

3

The SMOS mission

The SMOS (Soil Moisture and Ocean Salinity) mission was approved by the European Space Agency (ESA) in May 1999. Its objective is to provide global and frequent Soil Moisture and Sea Surface Salinity (SSS) maps. SMOS was launched on November 2, 2009, and after the first calibration and checkout period (the so-called Commissioning Phase), SSS Level 3 products will be distributed; the expected accuracy is 0.1 - 0.4 psu (practical salinity unit) over 100 x 100 200 x 200 km^2 in 30 - 10 days, respectively (*Font et al.*, 2004). The unique payload embarked on SMOS is the Microwave Imaging Radiometer by Aperture Synthesis (MIRAS) (*McMullan et al.*, 2008), it is a 2D interferometric radiometer operating at the protected L-band with a nominal frequency of 1413.5 MHz and a bandwidth of 27 MHz.

This chapter is devoted to the application of the microwave radiometry to the measurement of the sea surface salinity with particular attention to the case of the SMOS mission and the MIRAS radiometer.

3.1 Applying microwave radiometry to the measurement of sea surface salinity

As stated in “Consultative meeting in soil moisture ocean salinity: Measurement requirements and radiometer techniques”, (ESA, 1995), microwave radiometry is probably the best mean to remotely measure sea surface salinity. Microwave radiometry is characterized by a relatively good sensitivity to SSS (Figs. 3.1a and 3.1b) and, at the same time, by a quasi-complete independence to atmospheric conditions (Fig. 2.6).

Figures 3.1a and 3.1b show the brightness temperature for flat sea surface at 1.413 GHz, calculated using the Frenel reflection coefficient and the Klein and Swift model for the dielectric constant of seawater; SST is $20°C$, while SSS ranges between 0 and

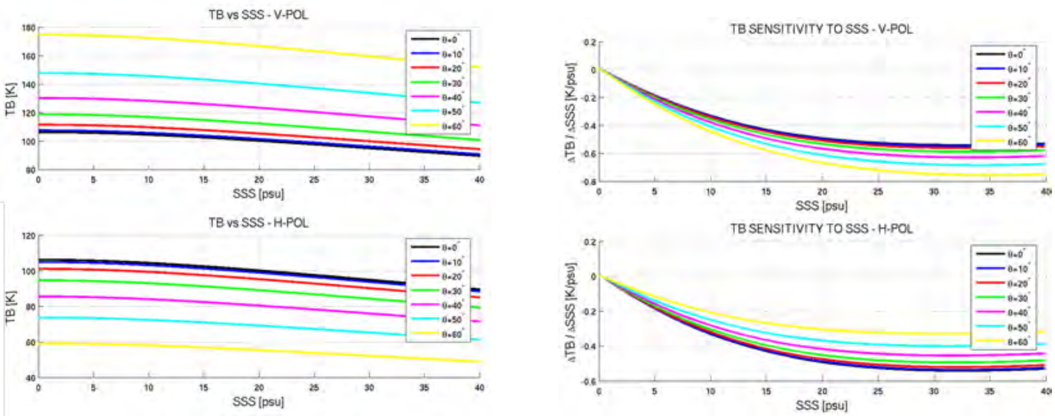

(a) (b)

Figure 3.1: (a) Brightness temperature and (b) its sensitivity to SSS at 1.413 GHz, calculated using Klein and Swift model for the dielectric constant of seawater, SST = **20**°, incidence angle from 0 to 60°.

40 psu, and the incidence angle between 0 and 60°.

A radiometer is a very sensitive receiver that measures the electromagnetic radiation emitted by an object in a given frequency band. This radiation, being basically thermal noise, has generally very low power. Four types of microwave radiometers are used: the **Total Power Radiometer** (TPR), the **Dicke Radiometer** (DR), the **Noise Injection Radiometer** (NIR), and the **Interferometric Radiometer** (IR). As an introduction to the topic the first and simplest case (TPR) is presented in the next section, the basic concept of the IR are described in section 3.3, while the Dicke Radiometer is expressed in chapter 6. Noise Injection Radiometers are not presented, since considered out of the scope of this thesis.

3.2 The Total Power Radiometer

The TPR is the simplest type of radiometer, its block diagram is shown in Fig. 3.2 (*Ulaby et al.*, 1982); on the left the functional blocks are shown, while the measured voltage and the signal spectrum are plotted in the center and on the left, respectively.

A TPR basically consists of:

- An **Antenna**,
- A Radio Frequency **Low Noise Amplifier**, characterized by its Gain (G_{RF}) and bandwidth B that determines the predetection bandwidth of the radiometer,

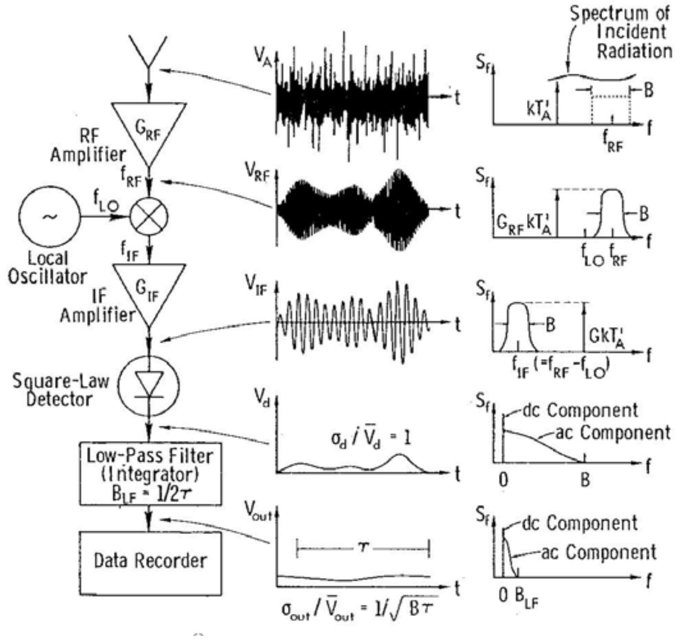

Figure 3.2: A Total Power Radiometer block diagram (*Ulaby et al.*, 1982)

- A **Mixer** to downconvert the signal to an Intermediate Frequency,
- An **IF Amplifier** characterized by its gain G_{IF},
- A **Power Detector**, the output voltage of which is proportional to the input power, characterized by its sensitivity $C_d[V/W]$, and
- An **Integrator** that acts as a Low-Pass filter with a bandwidth B_{LF}, characterized by the integration time used $\tau = 1/2B_{LF}$.

Considering a radiometer measuring an antenna temperature temperature T_A, similarly to the case of Eqn. 1.8 the power at the antenna is given by $P_A = k_B T_A B$, where k_B is the Boltzmann constant, and B the receiver bandwidth. Likewise the noise power generated by the receiver is $P_R = k_B T_R B$, where T_R is the receiver noise temperature. The radiometer's output voltage is thus given by:

$$V_0 = G(T_{ant} + T_{rec})k_B \tag{3.1}$$

where $G = G_{RF} \cdot G_{IF}$ is the total receiver's gain. Due to the random nature of the noise, the estimated antenna temperature a standard deviation (*radiometric resolution*) equal to (*Ulaby et al.*, 1982):

$$\Delta T = \frac{T_{ant} + T_{rec}}{\sqrt{B\tau}} \tag{3.2}$$

where τ is the integration time. According to Eqn. 3.2, the radiometric sensitivity decreases with the square root of the integration time.

Let us now consider the use a TPR in the case of SMOS ($\lambda = 0.2123m$). Assuming a Low-Earth orbit at 800 km (h), a 1000-km wide swath, a spatial resolution (Δs) of 30 Km, and a conical scan to spatially cover the Earth's surface, the resulting antenna should have the prohibitive diameter of $D \sim [\lambda \cdot h] / [\Delta s \cdot cos(\theta)] \simeq 7.5$ m (considering a $\theta = 32°$ tilting angle) and the maximum integration time of $\tau = 0.118$ $s = [\Delta s / v_{sat}] \cdot [\Delta s / FOV]$ would be permitted. To avoid the engineering problems associated with placing large scanning antennas of this size in orbit and the poor performances due to the use of such a small integration time, the option of launching a two-dimensional interferometric radiometer was proposed by the "Consultative meeting in soil moisture ocean salinity: Measurement requirements and radiometer techniques" (ESA, 1995).

3.3 Interferometric Radiometer

The basic concept of interferometric radiometry is to synthesize a large aperture using a number of small antennas. The output voltages of a pair of antennas (e.g. located at (X_1, Y_1) and (X_2, Y_2)) are cross-correlated to obtain the so-called "visibility samples", as expressed by the following equation:

$$V(u, v) = \frac{1}{k_B \sqrt{B_1 B_2} \sqrt{G_1 G_2}} \frac{1}{2} \langle b_1(t) b_2^*(t) \rangle, \tag{3.3}$$

where u and v are the spatial frequencies of visibility sample: $(u, v) = (X_2 - X_1, Y_2 - Y_1) / \lambda = (\Delta x, \Delta y) / \lambda$, k_B is the Boltzmann constant ($k_B = 1.3806 \times 10^{-23}$ $JK^{-1}Hz^{-1}$), B_1 and B_2 the receivers' noise bandwidths, G_1 and G_2 the available power gains, and $b_1(t)$ and $b_2(t)$ the signals measured by elements 1 and 2, respectively.

The complete set of the visibility samples is called a visibility map, and it is approximately the Fourier transform of the brightness temperature distribution of the scene. To invert this process the inverse Fourier transform can be applied as a first approximation (*Camps et al.*, 1997) or a more sophisticated G-matrix inversion (*Anterrieu and Camps* (2008); *Camps et al.* (2008a)), can be used. The result is a potential degradation of the radiometric sensitivity in terms of a higher rms noise, on the other hand a complete image is acquired in one snapshot, permitting to increase the integration time and improve the measurement quality. Nevertheless, the major advantage of interferometric radiometry is the multi-angular measurement: the output of an IR is, in fact, an image; this permits having several views under different incidence angles of the same point on the Earth before it exits from the Field of View. For these reasons, interferometric radiometry has been preferred by ESA over real aperture radiometers, leading to the design and implementation of the MIRAS instrument aboard the SMOS mission.

3.4 MIRAS radiometer

In 1998, a team of scientists from 10 European countries and USA proposed to the European Space Agency (*ESA*) the SMOS mission (SMOS website). After successfuly passing all the development phases, the final full approval was given by ESA in 2003. Six years later, on November 2, 2009 at 2.50 GMT SMOS satellite was launched from the Russian cosmodrome of Plesetsk (Fig. 3.3).

(a) (b) (c)

Figure 3.3: Three snapshots from the SMOS launch from the cosmodrome of Plesetsk, 2/11/2009 at 2.50 GMT. Courtesy of ESA.

Under ESA management, SMOS development has been funded mainly by the Spanish Centro para el Desarrollo Tecnologico Industrial (*CDTI*, (CDTI)) and the French Centre National dEtudes Spatiales (*CNES*, (CNES)). SMOS satellite, launched with a ROCKOT Breeze KM (a “low-cost” launcher based on a SS-19 ballistic missile operated by EUROCKOT (EUROCKOT)), is now on a low Earth polar Sun-syncronous dawn-dusk orbit, at 763 km of altitude, covering a complete orbit around the Earth in approximately 100 minutes. It is characterized by a 3-day revisit time at Equator and a spatial resolution ranging between 32 and 100 km.

According to the SMOS Mission Requirement Document (SMOS MRD) the overall goal for SSS retrievals from SMOS data is 0.1 psu (practical salinity units) for a ten-day average and $2° \times 2°$ resolution, Global Ocean Data Assimilation Experiment (GODAE) recommendations (*Smith and Lefrèbvre*, 1997).

The single payload of the SMOS mission is the **Microwave Imaging Radiometer by Aperture Synthesis** (MIRAS, *McMullan et al.* (2008)), it is a 2D interferometric radiometer operating at the protected L-band with a nominal frequency of 1413.5 MHz and a bandwidth of 27 MHz. It consists of three deployable arms connected to a central hub (8-m diameter radiometer when completely deployed). The arms are equally spaced with an angular separation of 120°. Each arm encompasses three segments, each one containing six L-band radiometers (LIghtweight Cost-Effective Front-end, *LICEF*), four more radiometers are situated in the central hub, for a total of 66 radiometers. In addition to that, there are three Noise Injection Radiometers (NIRs) located in the central hub, each of which consists of two LICEF receivers coupled to a single antenna. The total number of elements is therefore 69 antennas and 72 receivers, arranged as shown in Fig. 3.4.

The integration time used in MIRAS is 0.158 s, with an interval between snapshots of 1.2 s, allowing a snapshot radiometric sensitivity of 3.5 - 5.8 K over land and 2.5 - 4.1 K over ocean. Every 1.2 seconds data provided by the Control and Monitoring Network (CMN), by the Noise Injection Radiometer (NIR), by the LICEF units, plus additional information from the platform (attitude information) are recorded in the Raw-Data product. Raw Data are downloaded through the X-band channel when a ground contact is established. MIRAS can operate according to two different observation modes:

1. ***Dual-Polarization mode:*** Brightness temperatures are alternately measured in each polarization every 1.2 s, all the LICEFs measure the same polarization.

2. ***Full-Polarization mode:*** Brightness temperatures in H- and V- pol as well

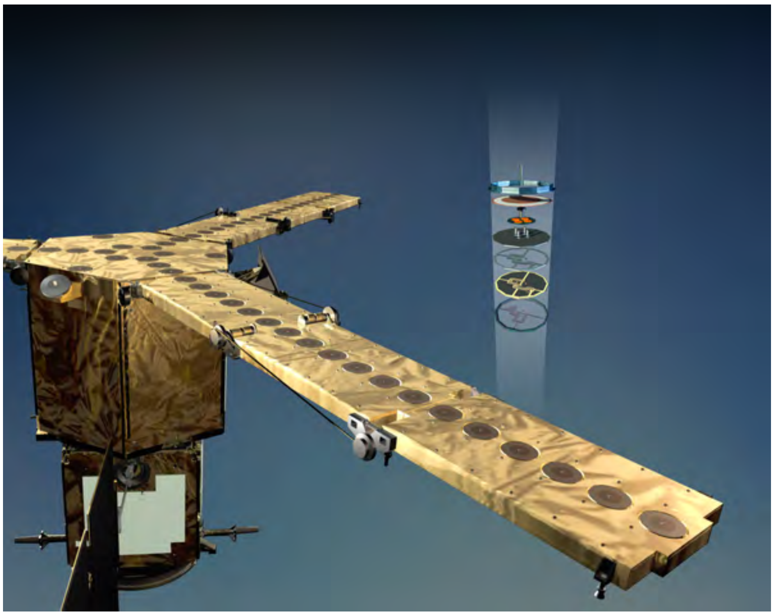

Figure 3.4: MIRAS arm and LICEF detail. Courtesy of ESA.

as the third and fourth Stokes parameters. Four consecutive integration times are used for each measurements. During the first integration time, all receivers measure the X polarization and during the third integration time, the Y polarization. In the other two integration times the polarization of one arm is the opposite of the other two arms to perform measurements of the cross-polarisation terms $\left(T_{XY/YX}\right)$. The arm in the alternative polarization rotates in a clockwise direction completing 4 rounds in each integration time.

Brightness temperatures are reconstructed in the director cosines domain (ξ, η):

$$(\xi, \eta) = (sin\,(\theta)\,cos\,(\phi)\,, sin\,(\theta)\,sin\,(\phi))\,, \tag{3.4}$$

where θ is the angle from the normal to the instrument plane $(0 \leq \theta \leq \pi/2)$ and ϕ is the angle in the instrument plane $(0 \leq \phi \leq 2\pi)$. Theoretically, the maximum visible space is the area inside the unit circle $\left(\xi^2 + \eta^2 = 1\right)$, even though non-zero antenna pattern backlobes also contribute to the TB image in the unit circle. Geometric conventions are sketched in Fig. 3.5.

The different phases of the ideal SMOS' image reconstruction process are shown in Fig. 3.6, pictures are taken from Professor Camps' lectures on "Imaging for microwave remote sensing" held at the Universitat Politècnica de Barcelona in 2008. As can be observed in Fig. 3.6:

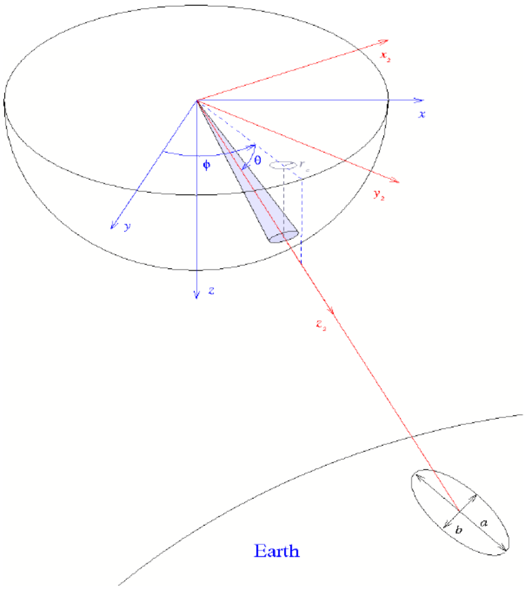

Figure 3.5: Geometric conventions for the definition of the (ξ, η) coordinates. Spatial resolution is defined as $\Delta x = \sqrt{a \cdot b}$

- visibility samples are measured and plotted as a function of the distance between antennas in the horizontal *(u)* and vertical *(v)* components;
- the visibility map is properly repeated to compute the Inverse Fourier Transformation (F^{-1}) leading to the brightness temperatures map (T_B) in the cosines domain, and finally
- the periodic extension is removed from the brightness temperatures map.

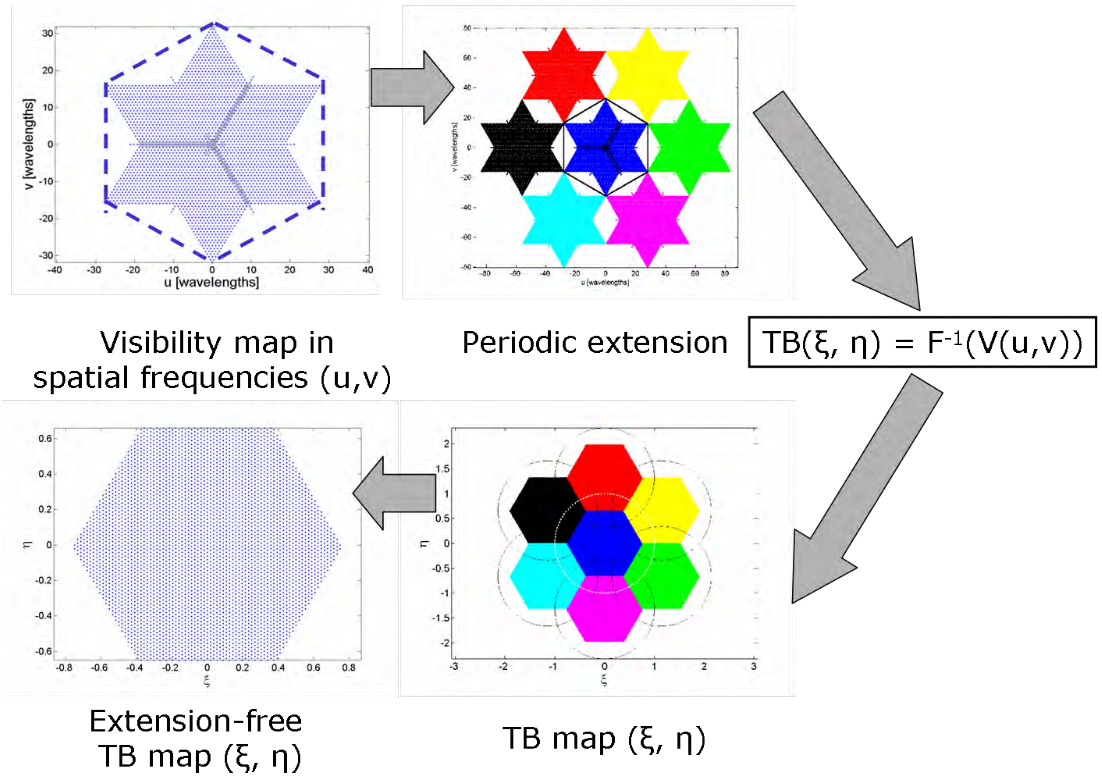

Figure 3.6: Phases of the ideal SMOS' image reconstruction process (from Professor Camps' lectures on "Imaging for microwave remote sensing").

According to the MIRAS instrument design the distance between antennas (d) does not satisfy the Nyquist criterion ($d \leq \lambda/3$) (*Camps et al.*, 1997) and part of the Field of View (FOV) is affected by aliasing, the six closest aliases circles are shown in Fig. 3.7, where the black dots stand for the theoretical maximum FOV, the red ones are the aliasing circle borders, and the central green zone is the Alias-Free Field of View (AF-FOV).

The AF-FOV can be extended considering that sky has low, stable, and known emission. This contribution can be modelled and its aliasing effects compensated, leading to the definition of the so-called Extended Alias-Free FOV (EAF-FOV), (Fig. 3.7b). In Fig. 3.7b, the black dots are the theoretical largest FOV, and the yellow zone in the center of the figure is the EAF-FOV.

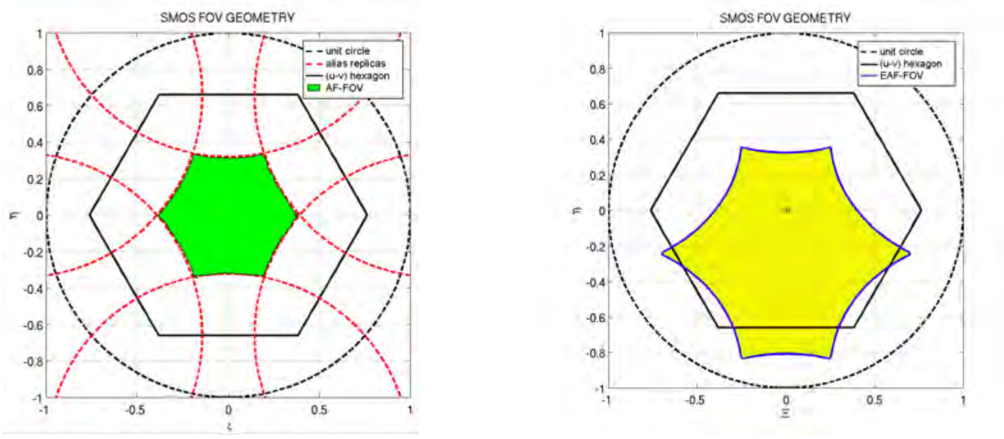

(a)

(b)

Figure 3.7: SMOS (a) AF- and (b) EAF-FOV in the cosines domain: (black) unit circle, (red) SMOS aliased zone borders, and (green) SMOS (a) AF-FOV and (b) EAF-FOV.

Due to this particular feature and to the dimensions of the FOV (aproximately 1000 x 1000 km) instrument parameters change according to their position in the FOV, among them the radiometric accuracy and sensitivity, the incidence angle, and spatial resolution (Fig. 3.8). Namely radiometric accuracy and sensitivity ranges in the intervals 2.5 - 4 K and 3.5 - 7 K, respectively, while incidence angle can assume values between 0° and 60° giving a spatial resolution ($\Delta x = \sqrt{a \cdot b}$) is bound between 32 and 100 km.

In Fig. 3.8a the radiometric accuracy (blue line) and sensitivity (red line) are shown, while in Fig. 3.8b the geometric parameters incidence angle (blue line) and spatial resolution (red line) are presented.

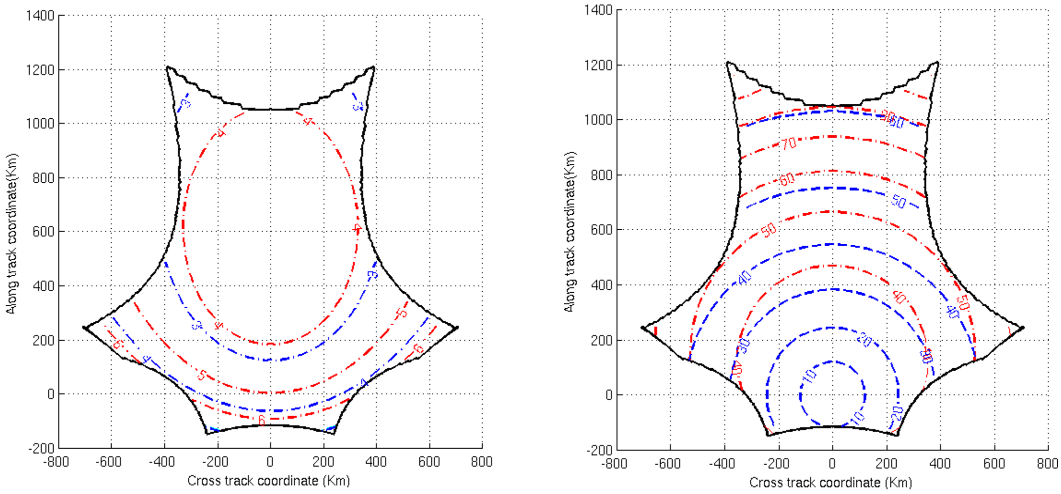

(a) (b)

Figure 3.8: .
](a) Radiometric (blue) Accuracy and (red) Sensitivity, and (b) (blue) Incidence Angle and (red) Spatial Resolution [calculated using SEPS].

3.5 SMOS data processing chain

Following CEOS (Committee on Earth Observation Satellites) (CEOS) conventions, SMOS products are distributed according to their level of "abstraction". Data are organised as follows:

- ***Raw Data:*** SMOS Payload data in their original format (CCSDS (Council of the Consultative Committee for Space Data Systems) packets) comprised of instrument observation data and housekeeping telemetry, as received from the satellite.
- ***Level-0 data products:*** SMOS Payload data in so-called Source Packets with added Earth Explorer product headers. These are chronologically sorted by Source Packet type: Observation Data and Housekeeping Telemetry.
- ***Level-1a data products:*** SMOS reformatted and calibrated Observation and Housekeeping data in engineering units. Level-1a products are physically consolidated in pole-to-pole time-based segments. Scientific SMOS level-1a products are the so-called "Calibrated Visibilities".
- ***Level-1b data products:*** The SMOS level-1b products are the output of the image reconstruction of the SMOS observation measurements and consist of Fourier

Components of Brightness Temperatures in the antenna polarisation reference frame.

- ***Level-1c data products:*** Since level-1b products are arranged as snapshots and not geographically sorted, SMOS level-1c products constitute reprocessed level-1b, which are geographically sorted, that is swath-based maps of brightness temperatures.
- ***Level-2 data products:*** Soil Moisture and Ocean Salinity swath-based maps.

Out of the responsibility of ESA, level 3 and 4 data products will be released by two institutions: *CP-34*-Spain, (CP-34) and *CATDS*-France. Level 3 and 4 processing includes spatial and temporal averaging as well as data from different sources.

- ***Level-3 data products:*** Global and regional maps of averaged soil moisture and ocean salinity. Only SMOS data can be used at this level.
- ***Level-4 data products:*** Global and regional maps of soil moisture, ocean salinity, and other derived magnitudes on the basis of the data provided by the SMOS satellite, data from other sources are supposed to be used at this level.

3.6 SMOS retrieval algorithm

SMOS level 2 retrieval algorithm has been defined according to a Bayesian approach to the problem: it embodies prior information to ease the retrieval. Assuming normal statistics on both the priors and the observations, the general Maximum Likelihood Estimation (MLE) reduces to a Least-Squares problem, the solution of which can be found through the minimization of a so-called *cost function*, expressed by:

$$\chi^2 = \sum_i \left[y_i - f\left(x_i\right)\right]^2, \tag{3.5}$$

being x_i the parameter to retrieve, y_i the measurement, and $f()$ the function that relates x and y.

The most general expression for the cost function in the case of SMOS is presented in Eqn. 3.6:

$$\begin{aligned} \chi^2 &= \left(\mathbf{F}^{\mathbf{meas}} - \mathbf{F}^{\mathbf{model}}\right)^T \mathbf{C_1}^{-1} \left(\mathbf{F}^{\mathbf{meas}} - \mathbf{F}^{\mathbf{model}}\right) + \\ & \left(\mathbf{p} - \mathbf{p}^{\mathbf{prior}}\right)^T \mathbf{C_2}^{-1} \left(\mathbf{p} - \mathbf{p}^{\mathbf{prior}}\right), \end{aligned} \tag{3.6}$$

where $\left(\mathbf{F^{meas}} - \mathbf{F^{model}}\right)$ is a vector containing all the misfits on the observables (brightness temperature in T_H or T_V polarization, or in the first Stokes' parameter in brightness temperature T_I) as detailed in the next section, p is a vector containing all the auxiliary parameters used in the retrieval, and $\mathbf{C_1}$ and $\mathbf{C_2}$ are the covariance matrices of the misfits and auxiliary parameters, respectively.

If both the measurements and the auxiliary parameters are considered completely uncorrelated, matrices $\mathbf{C_1}$ and $\mathbf{C_2}$ become diagonal, being the element on the diagonal proportional to the noise of the i-th measurement for the first matrix and to the uncertainty associated to the auxiliary field in the second one. In this case Eqn. 3.6 turns into:

$$\chi^2 = \sum_{i=1}^{N_{obs}} \frac{\left[F_i^{meas} - F_i^{model}\right]^2}{\sigma_{F_i}^2} + \sum_n \frac{\left[p_n - p_n^{prior}\right]^2}{\sigma_{p_n}^2} \ , \tag{3.7}$$

The error budget for the *SSS* retrieval in SMOS has been comprehensively studied by Dr. Roberto Sabia and is presented in *Sabia* (2008) and *Sabia et al.* (2010). Summarizing the results of this study, *SSS* retrieval error in the SMOS Level 2 product is mainly due to:

- TB (NIR) estimation inaccuracies;
- Imperfect Sun and foreign sources removal;
- Image reconstruction errors;
- Inaccuracies in the forward modelling of the TB dependence on the sea state;
- Inaccuracies in the sea water dielectric constant modelling.

In the next chapter two techniques aiming at mitigating these error sources are presented.

4

The external calibrations

Sea surface salinity retrieval can be improved using pre- and/or post-processing techniques and using both geophysical models and in situ data. Two techniques are presented in this chapter. Both have been tested using simulations: an ideal case, and two more realistic simulations of an open ocean zone and a coastal region. Results of these simulations are presented and discussed.

4.1 Introduction

As discussed in chapter 3, measuring *SSS* from space was not achievable until recently (*LeVine et al.*, 1998), and even now is considered a very challenging goal. Very strict requirements are imposed by oceanographical and meteorological models on salinity, and thus on both the radiometric sensitivity and the spatial resolution of the instrument, leading to a very difficult job from both the technological and the theoretical points of view.

Much effort has been spent in the last 15 years to improve microwave emission models on one side, and radiometer performances on the other side, resulting in the proposal definition, and launch of the SMOS mission in Europe and the Aquarius mission in US. In section 3.4 the innovative SMOS' single payload (MIRAS) is described and the theoretical basis of the retrievals are explained in section 3.6. The instrument must be very well calibrated and the retrieval procedures must be perfectly tuned to obtain useful *SSS*. For these reasons, to guarantee the fulfilment of the mission requirements auxiliary data has to be introduced (*Sabia et al.*, 2006), as well as both pre- and post-processing techniques. As stated in *Zine et al.* (2008) in fact, the level 2 processing foresees the use of auxiliary *SSS*, *SST*, and U_{10} fields during the inversion algorithm, apart from ancillary maps for the galactic contribution (*Reul et al.* (2008)

and *Tenerelli et al.* (2008)), the atmospheric contributions, and the TEC estimation (*LeVine and Abraham*, 2002).

In this chapter two techniques are presented:

- The first technique (*"External Brightness Temperature Calibration"*) was introduced in *Camps et al.* (2005a) and can be considered a sort of pre-processing of the brightness temperatures.
- The second technique (*"External Sea Surface Salinity Calibration"*) is a new, additional, post-processing technique proposed for the first time in this PhD thesis. It is proposed as a complement to the external brightness temperature calibration.

In sections 4.2 and 4.3 the theoretical basis of the external brightness temperature and sea surface salinity calibrations are described, while in sections 4.5 and 4.6 the effect of introducing those in the processing chain is assessed for an ideal case (section 4.5), and a realistic case in both an open ocean zone and a coastal region (section 4.6).

To simulate SMOS-like brightness temperature:

- the SMOS End-to-end Performance Simulator SEPS (*Camps et al.*, 2003) has been run in its light-mode (all the antenna pattern assumed to be equal) for the ideal case and full-mode (including measured antenna patterns for each antenna, all instrument errors, G-matrix image reconstruction, and so on...) for the two realistic ones; and
- the UPC SMOS L2PS (*Talone et al.*, 2007b) has been used, instead, to process the SEPS' outputs and return Sea Surface Salinity level 2 maps.

4.2 The external brightness temperature calibration

According to *Camps et al.* (2005a) errors in the reconstructed SMOS brightness temperature should be expected due to inaccuracies in the antenna pattern estimation, the image reconstruction algorithm, and the NIR brightness temperature measurements. This bias is scene-dependent (*Camps et al.*, 2008a), varying from snapshot to snapshot and polarization. As a possible mitigation of that phenomenon, the external brightness temperature calibration was proposed by *Camps et al.* (2005a). For each snapshot and for all the points in the Extended Alias-Free FOV, pseudo-brightness temperatures are calculated using auxiliary data and the same forward models used in the retrieval algorithms. The calculated pseudo-brightness temperatures are then subtracted from the measured ones, and the mean of this difference is considered as the mean bias introduced by the instrument errors. The "corrected brightness temperature" is then defined as the measured brightness temperature minus the mean bias. The algorithm can be summarized with the following expressions, where $\langle\rangle$ stands for mean value over the pixels in the Extentended Alias-Free Field of View:

$$\Delta T_B = \langle T_B^{meas} \left(SSS_{or}, SST_{or}, U_{10_{or}}, \theta\right) - T_B^{mod} \left(SSS_{aux}, SST_{aux}, U_{10_{aux}}, \theta\right)\rangle, \tag{4.1}$$

$$T_B^{corrected} = T_B^{meas} - \Delta T_B. \tag{4.2}$$

In Eqns. 4.1 and 4.2 the subscripts *"or"* and *"aux"* stand for original (value to be retrieved) and auxiliary parameter, respectively, while superscripts *"meas"* stand for measured, and *"mod"* for modelled parameter.

4.3 The external sea surface salinity calibration

As explained in section 3.6 the retrieval procedure within the SMOS mission is iterative. In this context one of most significant contributions to the success of the retrieval is given by the reliability and accuracy of the forward models. At present, the scientific community has not still completely agreed about the impact in the retrieved *SSS* of the inaccuracies in the current forward models, both for sea-water dielectric constant and sea surface roughness contribution to the brightness temperature. Meanwhile this issue is not entirely assessed, in the official SMOS-OS level 2 Operational Processor the Klein & Swift model (*Klein and Swift*, 1977) is used to calculate the dielectric constant of seawater and three different models are used for sea surface roughness: the two-scale model (*Yueh* (1997) and *Dinnat et al.* (2003)), the Small Slope Approximation model (*Irisov* (1997), *Johnson and Zhang* (1999), and *Reul et al.* (2001)), and the semi-empirical model by Gabarró et al. (*Gabarró et al.*, 2004). As mentioned in chapter 2, none of these models has proven so far better than the others. The external sea surface calibration aims at correcting for the mean uncertainty introduced by the forward model inaccuracies and implements a technique similar to the one used in rain radar calibration (*Seo and Breidenbach*, 2002) using as ancillary in-situ database the ARGO array of buoys. The algorithm consists of calculating a so-called *Calibration Factor* (*CF*) as the ratio between the auxiliary in-situ *SSS* mean value and the retrieved *SSS* one. The algorithm is simply implemented through the following expressions:

$$CF = \frac{\langle SSS_{in\_situ} \rangle}{\langle SSS_{ret} \rangle}, \tag{4.3}$$

$$SSS_{corr} = CF \cdot SSS_{ret}, \tag{4.4}$$

When computing the CF, a filtering based on the number of observations is applied: the pixels observed less than 40 times are not taken into account because of the large instrumental errors (Fig. 4.1). Figure 4.1 shows the error in the retrieved *SSS* as a function of the number of observations, more details on this figure are given in paragraph 4.6. The corrected retrieved salinity is then given by the product between CF (Eqn. 4.3)and the retrieved salinity.

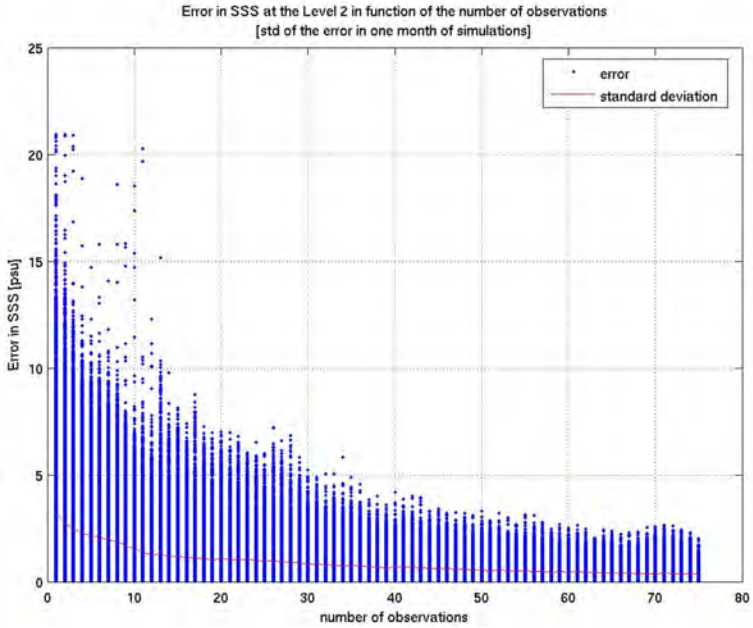

Figure 4.1: Error in the retrieved *SSS* in function of the number of observations

4.4 Methodology

Even if the geographic zone as well as the auxiliary parameters used change among the experiments, the procedure followed is the same and it is explained in the following paragraph.

As sketched in Fig. 4.2, the simulations involve both the external brightness temperature calibration and the external sea surface salinity calibration. The first technique can be considered a sort of pre-processing of the data before being ingested by the SMOS-L2PS and aims at improving the retrieval by eliminating the bias introduced by instrument errors. Moreover, since the relationship between salinity and the brightness temperature is non-linear, this bias mitigation helps linearising the retrieval (section 4.2). The second one is a post-processing of the *SSS*: in-situ salinity measurements are used to correct the biases introduced by the *SSS* retrieval algorithm itself and the eventual inaccuracies of the forward model (e.g. mainly dielectric constant model and sea state impact) and auxiliary data.

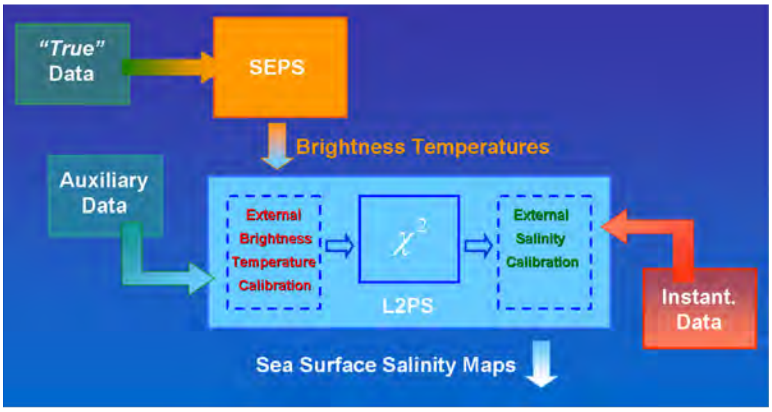

Figure 4.2: Flow chart of the external sea surface calibration testing procedure

As can be noticed in Fig. 4.2 three different databases are needed to carry out one test:

- **Original Data database:** Data used by SEPS in the forward modelling.
- **Auxiliary Data database:** Data used by L2PS as auxiliary parameter within the inversion cost function.
- **In-Situ Data database:** In-situ *SSS* measurements used during the external *SSS* calibration to improve the retrieval.

As mentioned in section 4.3, as source of in-situ auxiliary data the ARGO buoy array (*The ARGO Science Team*) has been chosen, being at the moment the best source of in-situ near real-time *SSS* measurements (*Boutin and Martin*, 2006). ARGO consists of almost 3,000 floats and provides 100,000 temperature/salinity profiles and velocity measurements per year, distributed over the global oceans at an average 3°

spacing. Data come from battery-powered autonomous floats that spend most of their life drifting at a depth called “parking depth”, where they are stable by having a density equal to the ambient pressure and a compressibility that is less than that of sea water. Floats cycle to 2000-m depth every ten days, with four- to five-year lifetimes for individual instruments. All ARGO data are publicly available in near real time via the Global Data Assembly Centers (GDACs) in Brest (France) (CORIOLIS) and Monterey, CA (U.S.) after an automated quality control and in scientifically quality-controlled form (delayed-mode data) via the GDACs within six months of collection. A pre-selection of the ARGO data has been made before performing the retrieval and, to have enough samples, data collected between the sea surface and the maximum depth of 10 m have been taken into account. For each satellite overpass a temporal window of one month, centered in the day of measurement, is considered and, with all the data available in this interval, a continuous map of the whole simulated zone is computed by spatial interpolation (*Burgees and Webster*, 1980).

4.5 Ideal case

4.5.1 Scenario

To test the potential of the external sea surface salinity calibration, an ideal scenario has been generated using ad-hoc geophysical parameters to simulate three different *SSS* fronts in the South Atlantic Ocean (*Talone et al.*, 2007b). The following Original, Auxiliary, and Instantaneous data have been used:

- **Original Data database:** A gradient in *SSS* of 5, 2, and 1 psu/10° of latitude (with values bound by 35 and 40, 37, and 36 psu, respectively), centered at 15°S have been generated, both *SST* and U_{10} are considered constant at 5, 15, and 25°C and 0, 7.5, and 15 m/s, respectively.

- **Auxiliary Data database:** Auxiliary *SSS* and *SST* are the same constant fields used as original *SST* and U_{10} perturbed by a 0.5°C and 2.5 m/s standard deviation Gaussian noise, respectively.

- **In-Situ Data database:** the instantaneous *SSS* comes from the ARGO database. For consistency only buoys between the sea surface and 10-m depth (*Boutin and Martin*, 2006) are selected, ARGO *SSS* values are overwritten by the original *SSS*; and a linear kriging interpolation (*Burgees and Webster*, 1980) provides the complete *SSS* field.

The simulation consists of 250 consecutive snapshots between latitude 37°S and 7°N and longitude 20°W and 0°.

4.5.2 Results and discussion

In total 71 simulations have been run, testing the 27 possible retrieval configurations without external calibrations, using the external temperature calibration and using both external temperature and salinity calibration. As mentioned, in this case the SEPS has been used in its Light Mode: it basically consists of assuming that all the 69 antennas of SMOS are equal (the measured antenna pattern of the first antenna is then used for all of them). Hence the Fast Fourier Trasformation can be used instead of the G-Matrix to compute visibilities and to perform the image reconstruction, largely reducing the computational time required for each simulation. The drawback is the presence of systematic structures in the simulated brightness temperature due to the particular features of the antenna pattern used (e.g. the higher salinity bands on the edges of the swath, as seen in Figs. 4.3 - 4.5).

Due to the scope of this first study, the accuracy of the SMOS-light has been considered acceptable for the ideal case, whereas for the realistic case SEPS full mode has been used. Figures 4.3 - 4.5 show the more remarkable results.

Retrieving without using any external brightness temperature calibration is very hard, even in the easiest case (with 5 psu /10°-gradient, 25°C of temperature, and no wind) the SSS front can barely be discriminated (Fig. 4.3).

When applying the external calibrations, the situation largely changes. Comparing the retrieved SSS results for the same scenario, the impact of the external calibrations is evident: using both of them the SSS front can always be distinguished in the cases of 5 and 2 psu/10° gradient. Figures 4.4 a - b show the worst configuration ($U_{10} = 15m/s$ and $SST = 5$°C, unrealistic value in this region for both cases.

In the case of having only 1 psu salinity gradient the retrieval is much harder and the SSS front is distinguishable only when climate conditions are favorable, i.e. low wind and/or high temperature scenarios and only at center of the swath, where the radiometric sensitivity is the best one (Fig. 4.5).

4.6 Real case

Encouraged by the results of the first study, two other scenarios, closer to the real SMOS mission expectations, have been defined and tested, including a numerical model of the ocean as real geophysical parameter provider. A whole month of complete simulations

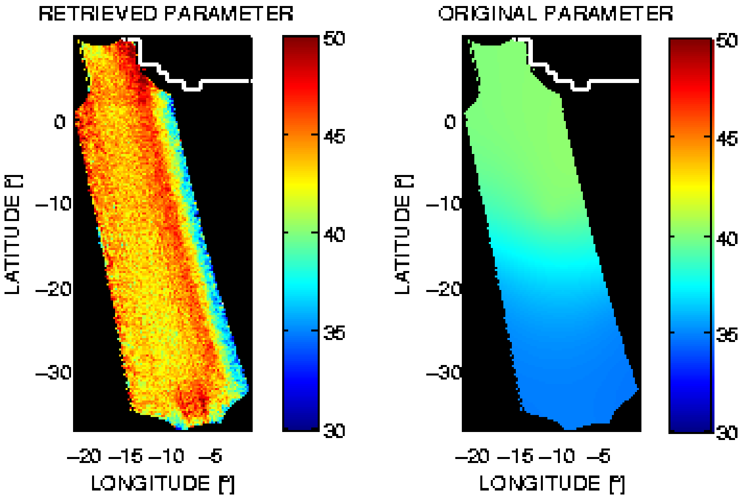

Figure 4.3: Retrieval result for a 5 psu/10° *SSS* gradient, at 25°C, with no wind and without any external calibration

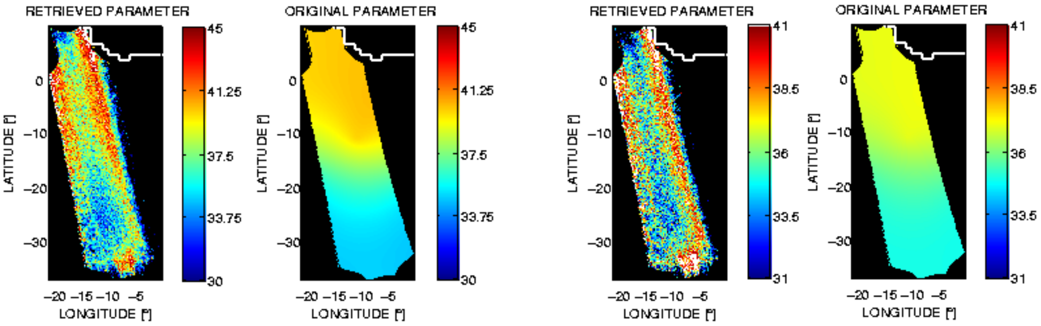

(a) (b)

Figure 4.4: Retrieval result for a (a) 5 and (b) 2 psu/10° *SSS* gradient, at 5°C with winds of 15 m/s, using both external calibrations

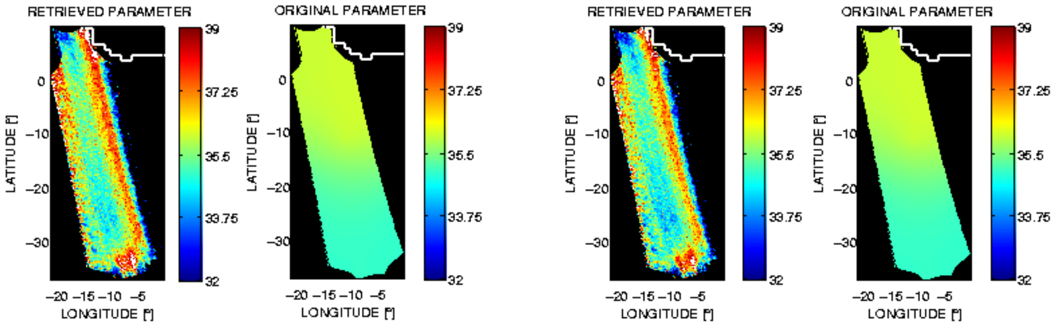

(a) (b)

Figure 4.5: Retrieval result for a 1 psu/10° *SSS* gradient, at 25°C, with no wind and (a) using the temperature calibration and (b) both calibrations

has been run for both scenarios in order to assess the quality of both level 2 and level 3 products.

Both scenarios are within the so-called Subtropical Gyre, a region of large *SSS* and *SST* gradients, very interesting from the oceanographical and biological points of view. Moreover, the second one is part of the region selected as Calibration and Validation zone by the SMOS and Aquarius mission teams. In the next paragraphs, both the scenarios as well as the procedure followed in this study will be presented. Results at both level 2 and level 3 are analysed in paragraphs 4.6.2 and 4.6.3.

4.6.1 Scenarios

As mentioned, two different scenarios have been simulated: one in open ocean and the other one closer to the coast to assess whether or not, and if so, how much auxiliary data can be included to improve the *SSS* retrieval quality and mitigate the coastal effects. It is well known that the coast vicinity induces errors in the retrieved *SSS* (*Zine et al.*, 2007) due to the particular image processing applied in SMOS (which is very sensitive to the sharp transition between sea (90 - 150 K) and land (~300 K) (*Camps et al.*, 2008a)).

The Open-Ocean scenario is a zone in the North Atlantic Ocean, bound in latitudes by $(9°N, 27°N)$ and in longitudes by $(27°W, 40°W)$. Figure 4.6a shows the zone and the "real" geophysical parameters, in the clock-wise direction the GoogleMaps view, the *SSS*, U_{10}, and *SST* fields for the 1st of March (59th day of the year). A total of 64 satellite overpasses (more than 1,500 snapshots) have been simulated and both ascending and descending orbits have been considered in the retrieval.

For the coastal region, a similar size region have been considered, but with a small shift towards the North-East, in order to include in the simulation the effect of the proximity of the coast on quality of the the retrieved *SSS* at levels 2 and 3. For this scenario latitudes are bound between 20 and 40 degrees North, and longitudes between 5 and 20 degrees West, making a box of 20x15 degrees. As for the Open-Ocean scenario, Figure 4.6b shows the zone and the original geophysical parameters for March, 1^{st}. In this case 69 satellite overpasses have been required to cover the zone (more than 1600 snapshots), once again both ascending and descending orbits have been considered for the retrieval.

Concerning the simulations settings three databases have been defined, as sketched in Fig. 4.7, namely:

- **Original Data database:** Daily outputs of a 0.5° configuration of the NEMO-OPA ocean model (*Madec* (2008) and *Mourre et al.* (2008)) are used as original *SSS* and *SST* data, 10-m-height wind-speed (U_{10}) fields come from the European Centre for Medium-Range Weather Forecast (ECMWF) ERA40 reanalysis (*Uppala et al.*, 1996).

- **Auxiliary Data database:** Auxiliary *SSS* and *SST* come from Levitus climatology (*Levitus* (1998)), and (U_{10}) are extracted from the National Centers for Environmental Predictions (NCEP) NCAR reanalysis (*Kalnay et al.*, 1996).

- **In-Situ Data database:** Due to the lack of measurements in the selected zones (Figs. 4.8 and 4.9), volunteer observing ships (VOS) have been added to the ARGO database. VOS data are available at the CORIOLIS FTP server (CORIOLIS). In order to ensure consistency between original and instantaneous data, for both ARGO and VOS, only temporal and spatial information are kept, whereas salinity measurements have been overwritten by the OPA-output *SSS* (original data); no error has been added. Finally, kriging interpolation (*Burgees and Webster*, 1980), based on the modified ARGO and VOS measurements, provides the complete instantaneous *SSS* field.

4.6.2 Results at level 2

As explained in chapter 3, the level 2 product is defined as the retrieved salinity for each satellite overpass; the number of points used in the retrieval depends on the position of the point in the field of view. The requirements for the level 2 product are a retrieved *SSS* error rms < 1 psu.

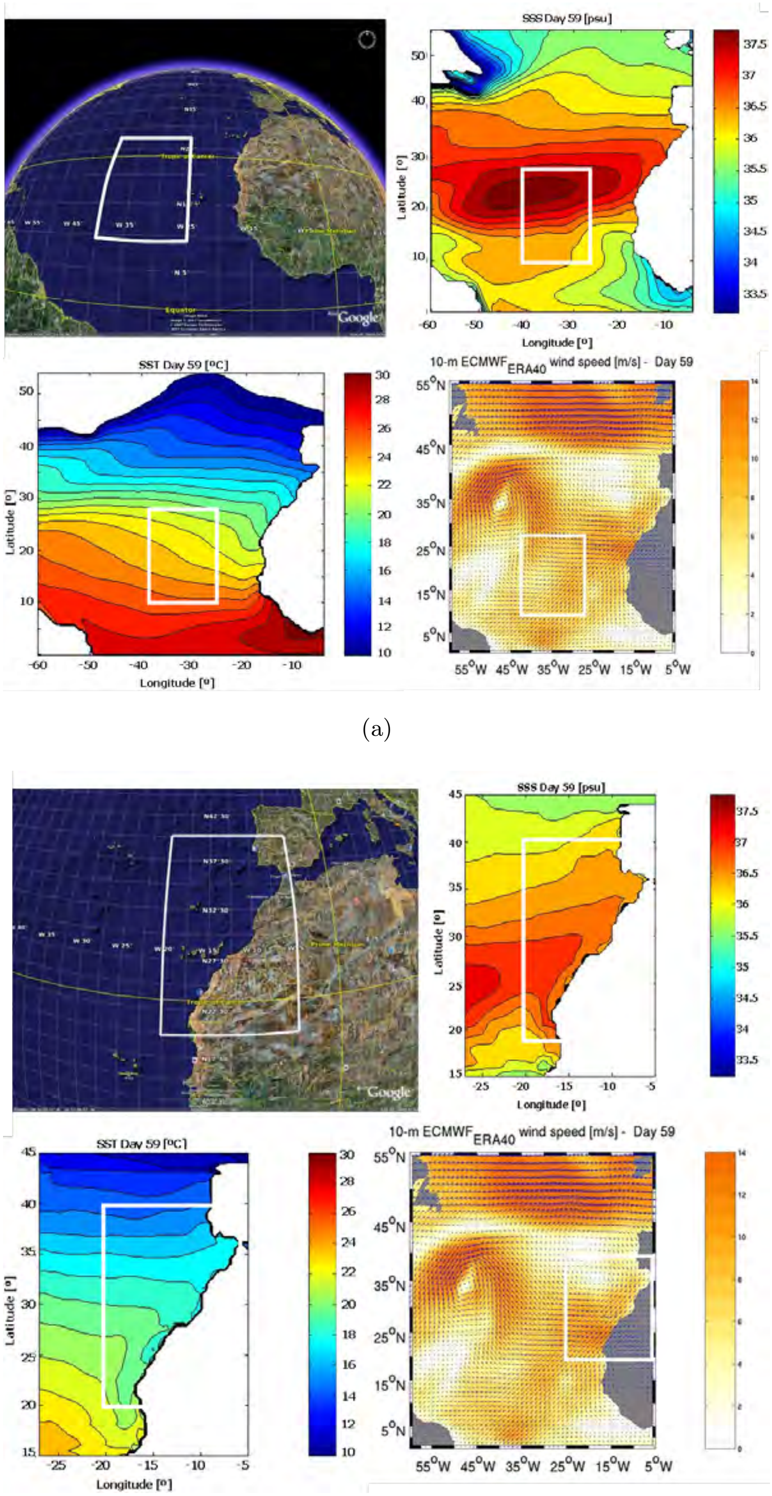

(a)

(b)

Figure 4.6: (a) Open-Ocean and (b) Coastal-Region scenario, in the clock-wise direction: GoogleMaps view, OPA *SSS*, ECMWF-ERA40 U_{10}, and OPA *SST* fields

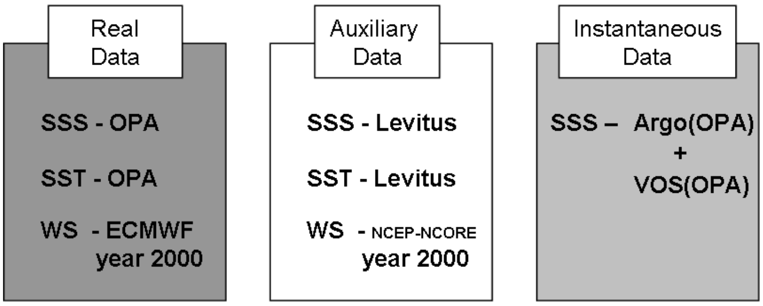

Figure 4.7: Databases used for the realistic case

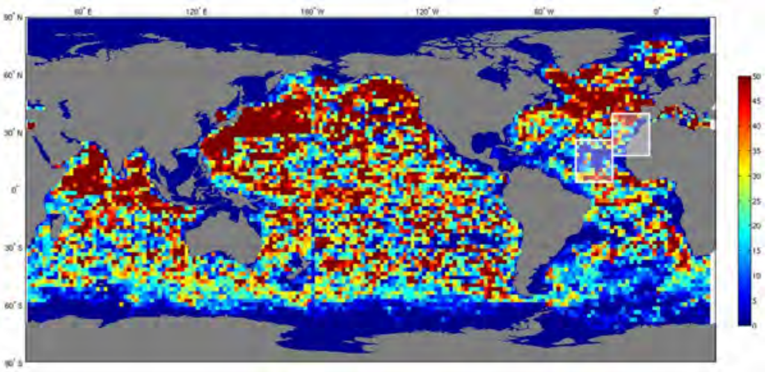

Figure 4.8: Total ARGO buoys observations beetween 2001 and June 2007 in a uniform 2 x 2 grid, the simulated zone are highlighted

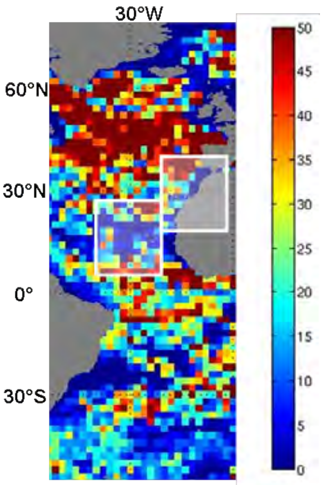

Figure 4.9: Zoom of the total ARGO buoys observations map in Fig. 4.8, the simulated zone are highlighted

Figures 4.10 (a) and (b) summarize the performance of the retrieval algorithm for all the 64 overpasses simulated over the Open-Ocean zone, when only the brightness temperature calibration is applied or both of them are, respectively. In both figures the number of overpass is indicated in the abscises, while in the ordinates is the error in psu; the mean error, its standard deviation, and the rms are shown in the upper, middle and bottom plots, respectively. As a general comment, it can be said that the majority of the retrievals are within the specifications (the lower plot shows the rms for each of the overpasses, as well as the 1-psu limit marked in red) even using only the external brightness temperature calibration; using both techniques however the quality clearly improves, highly reducing the mean bias of the retrieved *SSS*. The objective of the technique is in fact to reduce the bias, but preserving the local variations within the image; as expected the bias goes near to zero and the standard deviation results unaffected by the calibration (changes are of the order of 10^{-4}). The SSS_{err} mean value passes from having a peak-to-peak amplitude of more than 0.7 to 0.2 psu after the external salinity calibration in the case of open ocean (Figs. 4.10a and 4.10b).

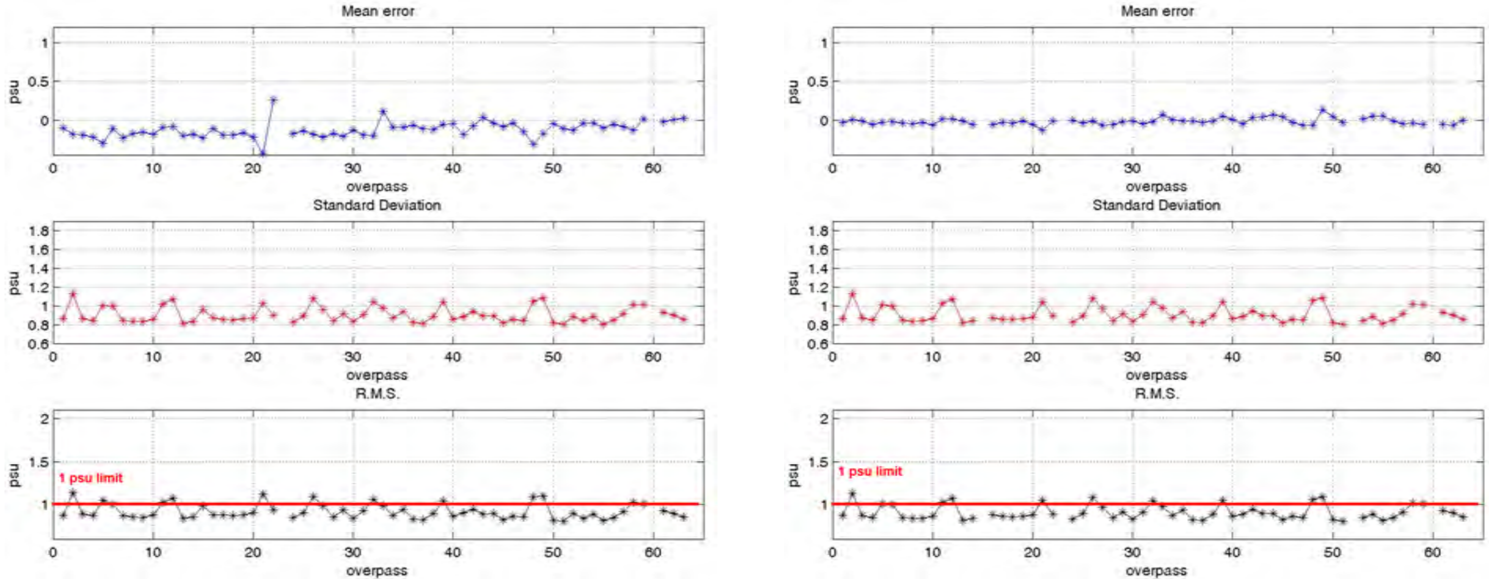

(a)

(b)

Figure 4.10: Retrieval performance at level 2 using (a) only the external brightness temperature calibration and (b) both the external brightness temperature and sea surface salinity calibrations - OPEN OCEAN

Results for the coastal region show a similar trend but, as plotted if Fig. 4.11, being closer to the coast than in the first scenario, the general performance of the retrieval is poorer than in the open ocean: the standard deviation of the error is 1.5 - 2 times larger (from 0.8 - 1.2 to 1 - 2 psu) than in the Open-Ocean case (Figs. 4.11a vs. 4.10a). However, once again, the external salinity calibration improves definitely the quality of the retrieval, especially in the mean error (passing from having the 20% of overpasses with a mean SSS_{err} larger than 1 psu (Fig. 4.11a) to having just 8% of the overpasses in that condition after the external salinity calibration (Fig. 4.11b)). As in the open ocean case, the bias is reduced, while preserving the local variations within the same image.

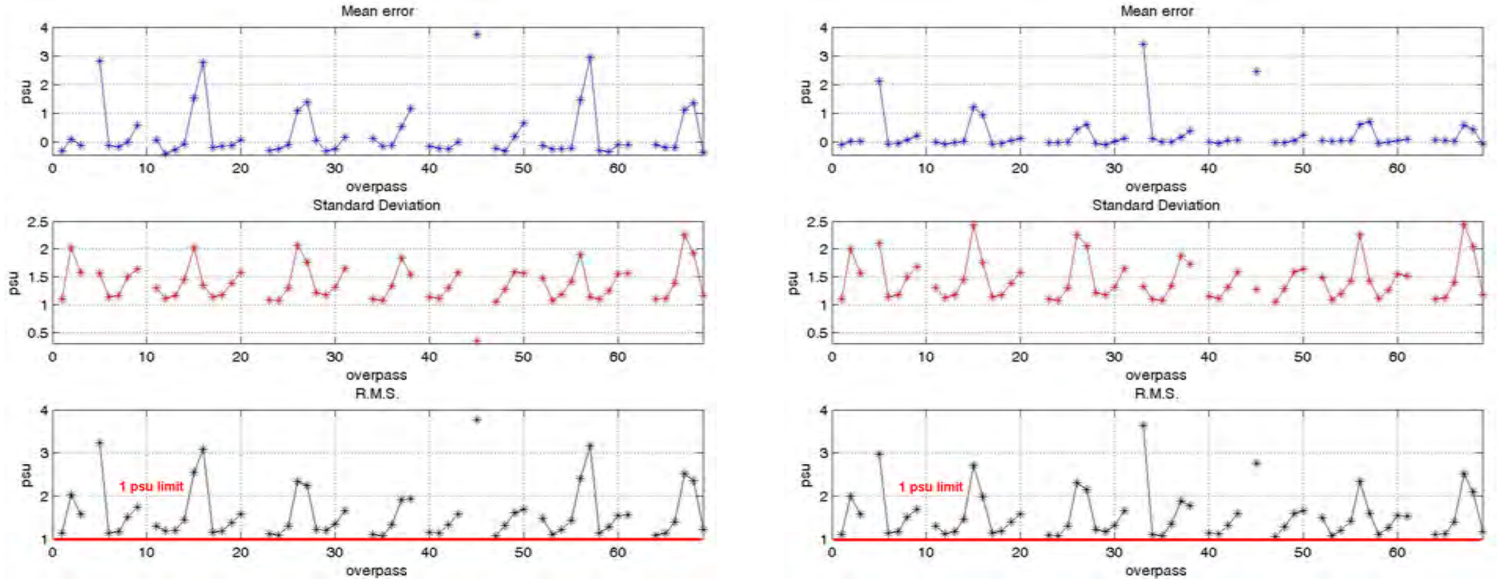

(a)

(b)

Figure 4.11: Retrieval performance at level 2 using (a) only the external brightness temperature calibration and (b) both the external brightness temperature and sea surface salinity calibrations - COASTAL REGION

As can be noticed, some of the overpasses in both the open ocean and the coastal region scenarios are missed in Figs. 4.10 and 4.11 because of the filter applied to the points before computing the mean and standard deviation: in this calculation only points observed more than 40 times (40 Tx-Ty pairs) are taken into account, due to the error variability within the SMOS Field Of View. The error is in fact strongly dependent on the number of observations as depicted in Fig. 4.12, where all the retrieved points in the whole simulated month are considered and the error in *SSS* is plotted as a function of the number of observations; the red line stands for the standard deviation of the error absolute value as a function of the number of observations. Very large errors are found for points observed less than $N = 20$ times (from 5 to 22 psu); it is still larger than 4 psu for pixel with up to 40 observations, and above 40 observations it becomes nearly constant and bound between 0 and 3 psu.

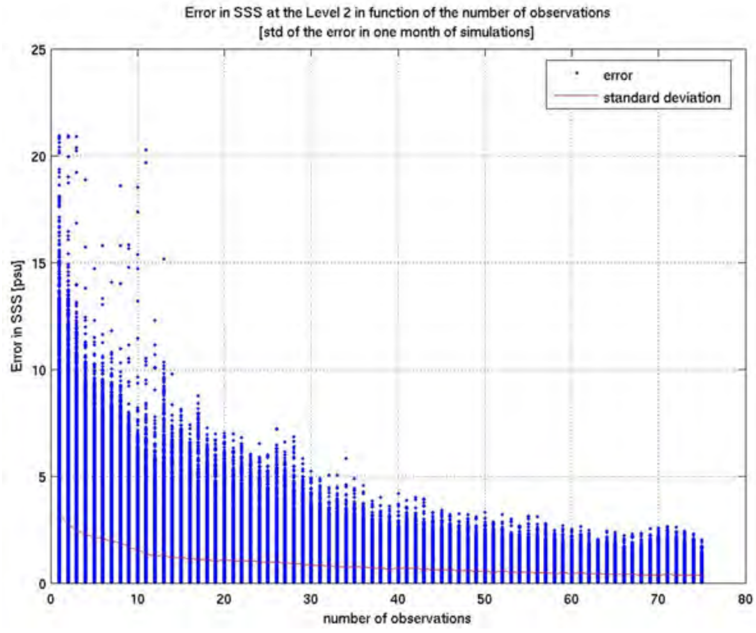

Figure 4.12: Error in the retrieved *SSS* in function of the number of observation in the whole simulated month - OPEN OCEAN

In Fig. 4.13 the same plot is shown for the coastal region case, the analysis is not as easy as in the open ocean simulation; the error in fact decreases with the number of observations, but is also dependent on the proximity to the coast and generally larger than in the open ocean case. These effects will be discussed in more detail in Fig. 4.20.

It has to be noticed that in all the statistical tests, for the Open-Ocean scenario as well as for the coastal Region, the measurements pass throught a filter before the

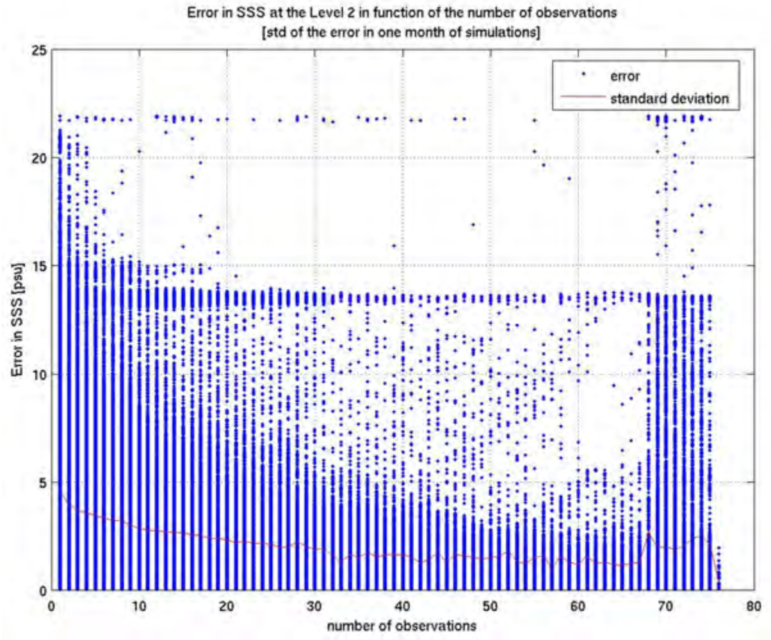

Figure 4.13: Error in the retrieved *SSS* in function of the number of observation in the whole simulated month - COASTAL REGION

calculations in order to eliminate the artifacts in the transition region (Fig. 4.14) at the beginning and at the end of the overpass. In Fig. 4.14b the number of observations is plotted as a function of the cross-track distance.

In Fig. 4.15 (a) the mean value and (b) the standard deviation of the error in the retrieved *SSS* after applying both external brightness temperature and sea surface salinity calibration are shown as a function of the cross-track distance; as it can be noticed, the bias is almost equal to zero, with fluctuations on the order of 0.5 psu in both the so-called “Narrow Swath” (640 km) (*Barré et al.*, 2008). A similar trend is followed by the standard deviation of the retrieved *SSS* error, which is approximately constant and lower than 1.5 psu, in the same zone.

For the sake of completeness, for two selected overpasses the original, retrieved , auxiliary and error in the retrieval of *SSS* are shown (Figs. 4.16 and 4.17), as well as the histograms of the retrieval errors (Figs. 4.18 and 4.19). The first overpass is taken from the open ocean simulation and corresponds to a descending orbit on March, the 2^{nd} (4^{th} simulated overpass), whose first of 205 snapshots is acquired at 20.37 GMT. The second one is the 26^{th} overpass of the coastal region simulation (March, the 12^{th}), and consists of 241 consecutive snapshots of a descending orbit starting at 18.54

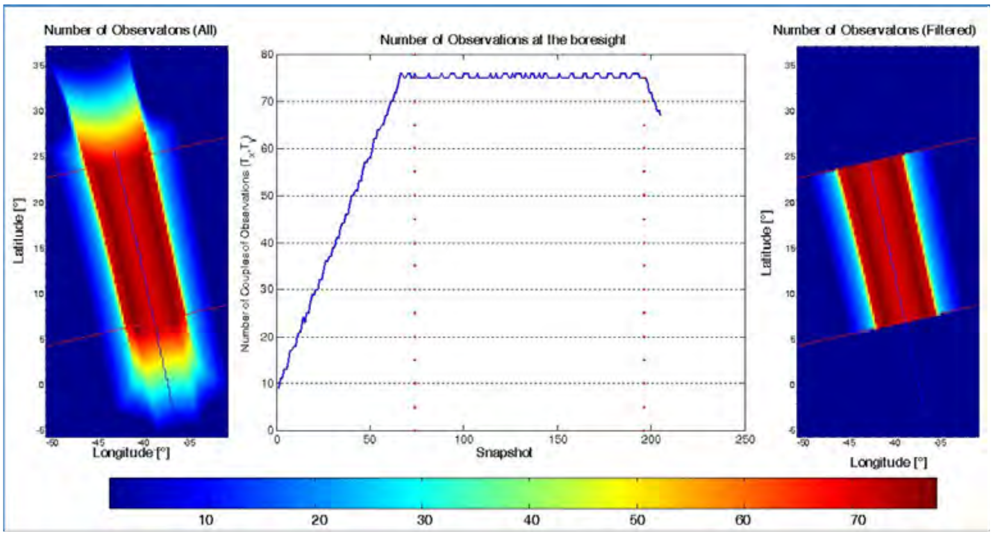

(a)

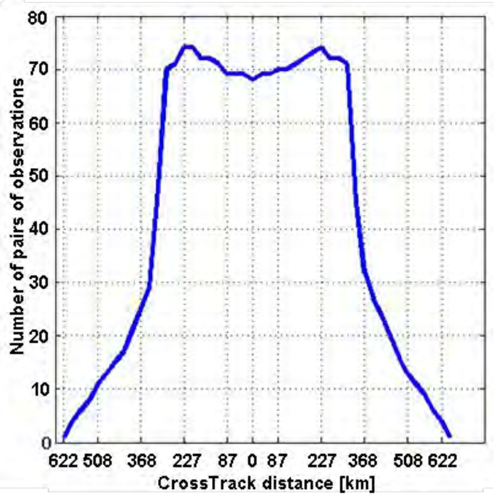

(b)

Figure 4.14: (a) Filter applied to eliminate the transitions at the beginning and at the end of the overpass and (b) number of observations as a function of the cross-track distance

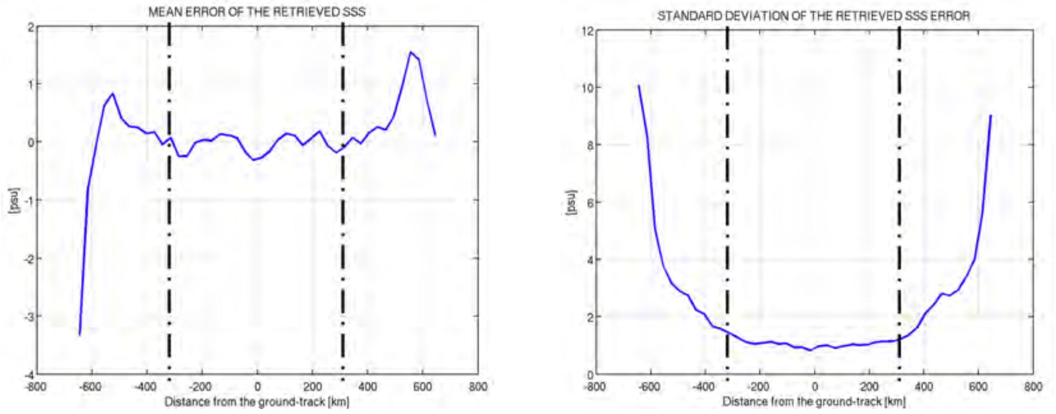

(a) (b)

Figure 4.15: (a) Mean value and (b) standard deviation of the error in the retrieved *SSS* as a function of the distance from the ground track using both external brightness-temperature and salinity calibrations. The dash-dot line indicates the so-called "Narrow-swath".

G.M.T.. In both cases the retrieved, original, and auxiliary salinity fields, and the error for the retrieved *SSS* are shown in the case of using (a) only the external brightness temperature calibration, and (b) both calibrations. Figures 4.18 and 4.19 instead show the histogram for the retrieved *SSS* error, including the values for mean bias and standard deviation when (a) only the external brightness temperature calibration is used, or (b) both are used. In this particular cases the mean error passes from -0.222 to -0.058 psu for the open-ocean simulation, and from -2.152 to -1.067 psu for the coastal-region one. In terms of rms, the final gain applying the external *SSS* calibration is just a 3% (0.846 compared to 0.873) for the open-ocean simulation, and 13.5% (3.521 compared to 4.073) for the coastal-region one, which was somehow expected since the good of the external calibration is the cancellation of the instrumental and modelling biases.

Coast-proximity effect

In Figs. 4.20a, b, the mean and, in Figs. 4.20c, d, the rms values of SSS_{err} are shown as a function of the distance from the coast (absises) and of the number of observations (ordinates). On the left panel (Figs. 4.20a and c) only brightness-temperature calibration has been used, whereas on the right one (Figs. 4.20b and d) the results of using both calibrations are presented.

Large errors (34 psu) are found up to 150 km away from the coast even for points

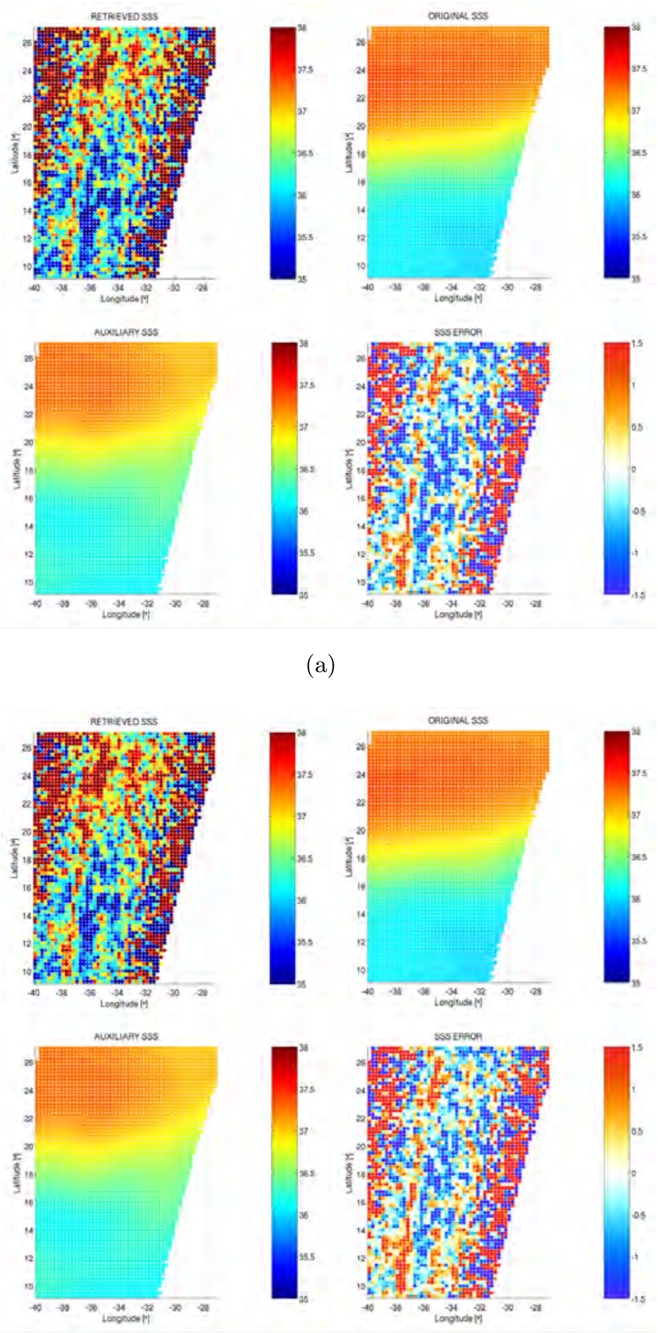

(a)

(b)

Figure 4.16: Level 2: OPEN OCEAN SIMULATION - Retrieved, original, auxiliary, and SSS error for the 4^{th} overpass using (a) only the external brightness temperature calibration and (b) both the external brightness temperature and sea surface salinity calibrations.

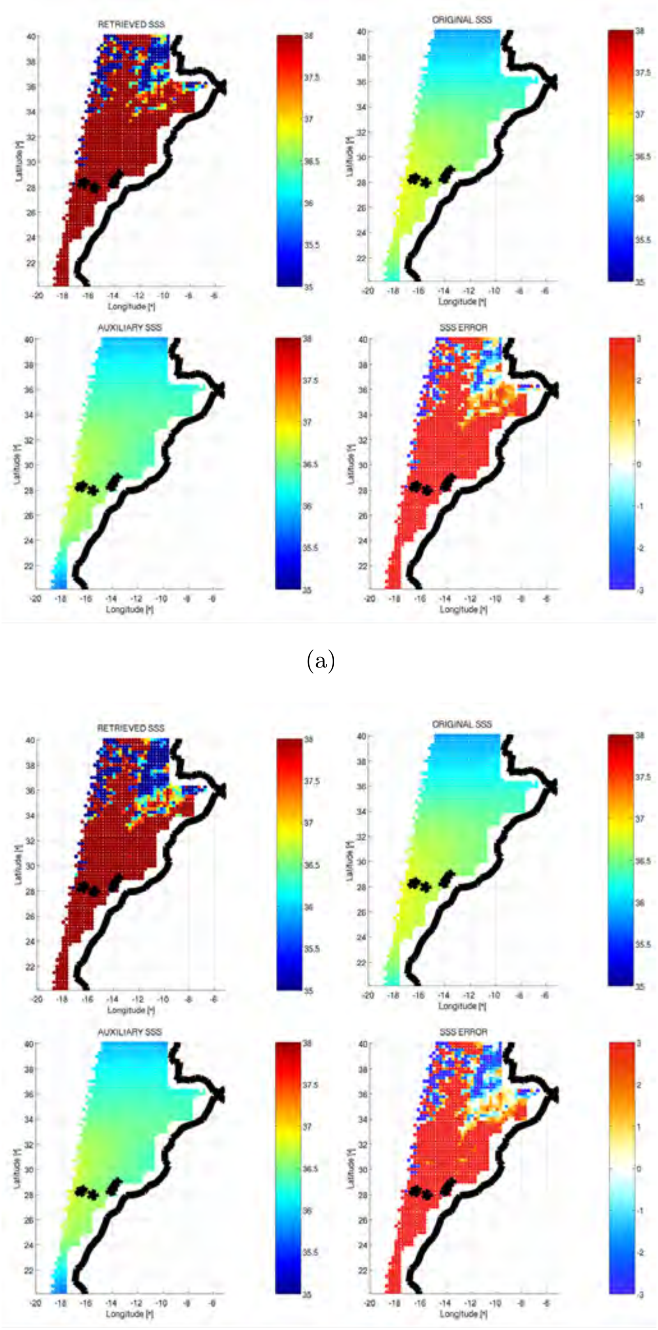

(a)

(b)

Figure 4.17: Level 2: COASTAL REGION SIMULATION - Retrieved, original, auxiliary, and *SSS* error for the 26^{th} overpass using (a) only the external brightness temperature calibration, and (b) both the external brightness temperature and sea surface salinity calibrations.

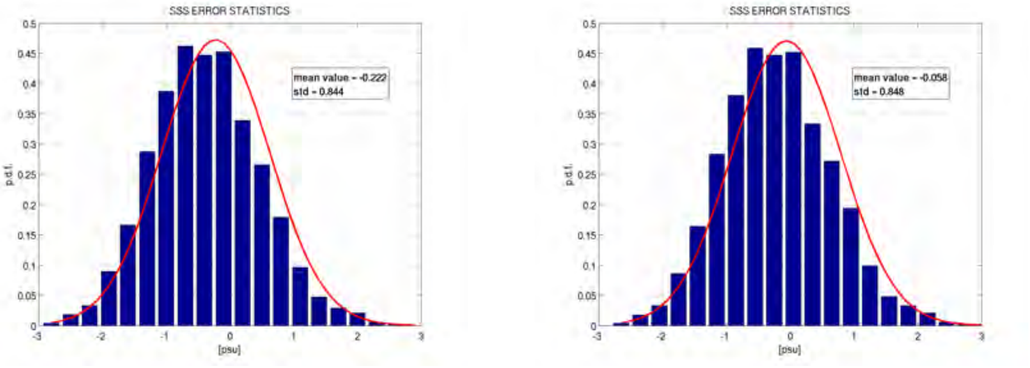

(a) (b)

Figure 4.18: Retrieved *SSS* error histogram of the 4^{th} overpass of the open ocean simulation using (a) only the external brightness temperature calibration and, (b) both external calibrations.

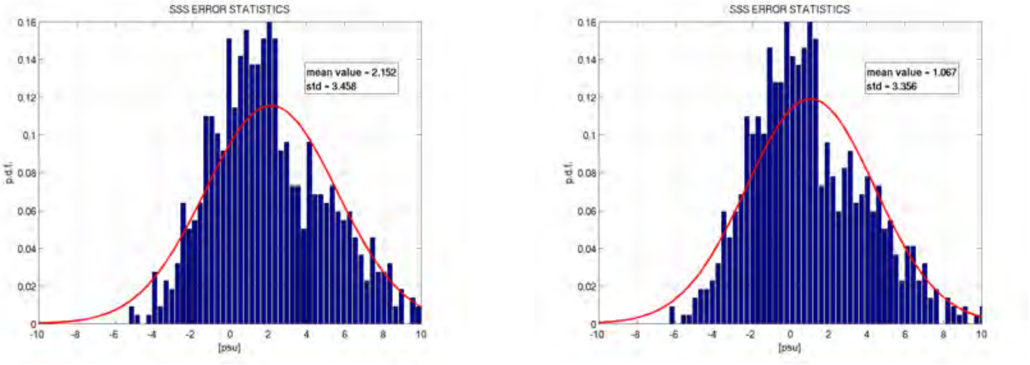

(a) (b)

Figure 4.19: Retrieved *SSS* error histogram of the 26^{th} overpass of the coastal region simulation using (a) only the external brightness temperature calibrationand, (b) both external calibrations.

observed more than 60 times. The external salinity calibration improves the quality of the retrieval: mean SSS_{err} reduced by 25% (0.5 over 2 psu) and rms by 10% (0.5 over 5 psu), particularly in the zones with largest errors (low number of observations).

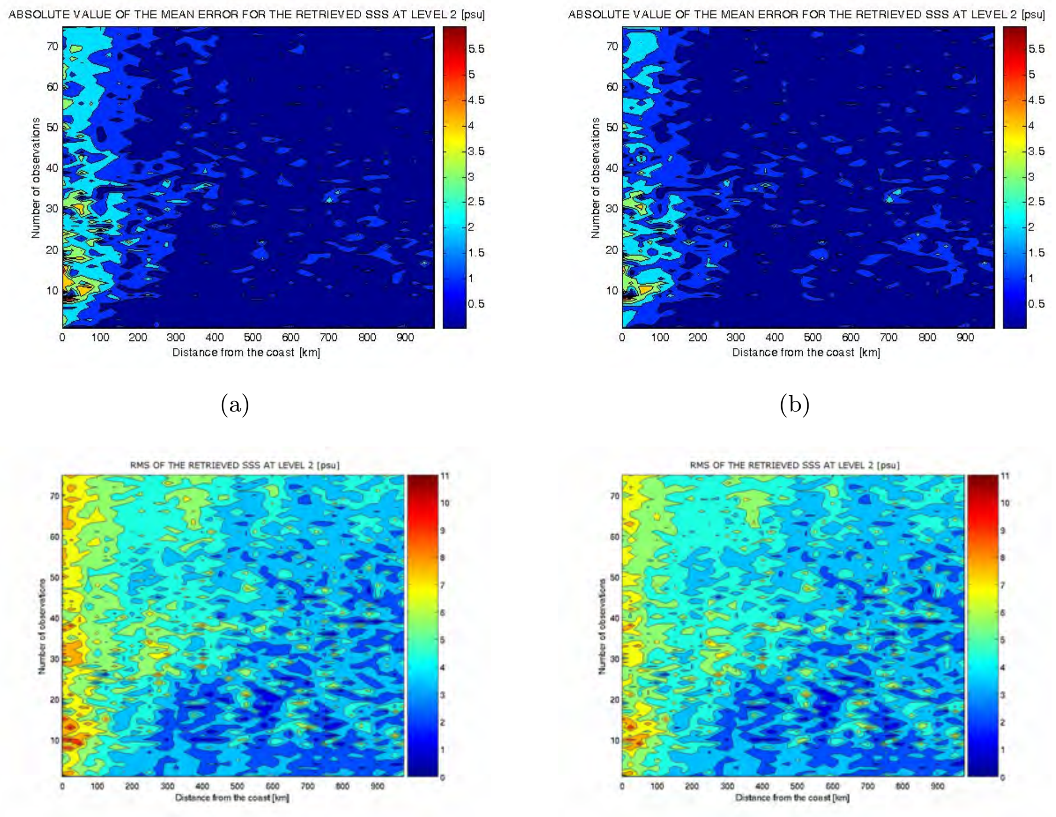

(a) (b)

(c) (d)

Figure 4.20: Mean and rms values of the retrieved *SSS* error as a function of the distance from the coast and of the number of observations, using (a) and (c) only the brightness-temperature calibration or (b) and (d) both external calibrations.

4.6.3 Results at level 3

At level 3 two products have been produced:

- The first one is a 10-day average of the retrieved *SSS* in a 200 x 200 km grid and it is expected to fulfill the specification of an accuracy better than 0.4 psu.
- The second one is the 30-day average of the retrieved *SSS* in a 100 x 100 km grid and its expected to reach the accuracy of 0.1 psu.

Table 4.1: Retrieval performance at level 3

[psu]	$\mu(SSS_{err})$		$\sigma(SSS_{err})$		$rms(SSS_{err})$	
External Salinity Calibration	NO	YES	NO	YES	NO	YES
Open-Ocean						
30-day	-0.0579	0.0652	0.1526	0.1358	0.1632	0.1506
10-day	-0.1362	0.0282	0.2239	0.2043	0.2621	0.2062
Coastal Region						
30-day	0.2467	0.3297	0.7361	0.6898	0.7763	0.7645
10-day	0.0559	0.1581	0.6835	0.5555	0.6858	0.5776

Level 3 products have been defined as a weighted mean of the level-2-retrieved *SSS*. The weights have been calculated as inversely proportional to the standard deviation of the error in the level 2 retrieval, sorted as a function of the number of observations, as expressed in Eqns. 4.5 and 4.6, where the subscript i stands for the number of measurements at level 2 used to synthesize the correspondent one at level 3.

$$SSS^{L3} = \frac{\sum w_i \cdot SSS^{L2}}{\sum w_i}, \tag{4.5}$$

$$w(n_{obs}) = 1/std(SSS_{retr}(n_{obs}) - SSS_{orig}). \tag{4.6}$$

Three 10-day products have been generated. The performance is very similar and only the products referred to the first decade (1^{st} - 10^{th} of March) are presented. In order to better quantify the improvement induced by the external salinity calibration technique for each product the retrieved *SSS* error histogram is shown.

For both the level 3 products, quality improves after using the external salinity calibration. The SSS_{err} mean value (μ), standard deviation (σ), and rms are reported in Table 4.1.

A decrease of 1.5% - 7.7% and a 15.7% - 21.3% of the SSS_{err} rms is found for the 30- and 10-day products, respectively, being larger in the open-ocean case. Results indicate that SSS_{err} at level 3 is dominated by the standard deviation of the error at level 2, which is actually limiting the benefits of the external salinity calibration. In Figs. 4.21 and 4.22, the resulting level 3 10-day and 30-day (Figs. 4.23 and 4.24) products and the corresponding error when applying both external brightness temperature and salinity calibrations for the open ocean (Figs. 4.21 and 4.23) and coastal zone (Figs. 4.22 and 4.24) are shown,respectively.

Applying both external calibrations, for the open-ocean zone, error at level 3 is almost included between -0.4 and 0.4 psu for the 10-day product and -0.2 and 0.3 psu for the 30-day product. The rms error are 0.20 and 0.15 psu, respectively, (Table 4.1), fulfilling the SMOS mission requirements in the first case and very close to that in the second one. Performance is, instead, very different in the coastal region, where the rms error is far away from the requirements. As expected, larger errors are found close to the coast, where it exceeds 2 psu. The very low retrieved *SSS* in Figs. 4.22 and 4.24 at (28°N - 29° N, 14°W - 16° W) are caused by the presence of the Canary Archipelago, that, even if masked, strongly affects the neighbour pixels.

Finally, as for level 2 products, statistics are shown in Figs. 4.25 - 4.28 for the 10-day and 30-day products applying (a) only the external brightness-temperature calibration or (b) both the external brightness-temperature and sea surface salinity calibrations. Figures 4.25 and 4.26 are referred to the open ocean scenario, whereas Figs. 4.27 and 4.28 to the coastal region simulation.

Coast-proximity effect

Coast-proximity dependence of the error at level 3 is more apparent from Fig. 4.29, where retrieved *SSS* error as a function of the distance from the coast is presented for the 10-day (Fig. 4.29a and 4.29b) and 30-day (Fig. 4.29c and 4.29d) products, applying only the brightness-temperature calibration (Fig. 4.29a and 4.29c), or both (Fig. 4.29b and 4.29d).

The triangle-, square-, and circle-marked lines stand for the mean value, rms, and standard deviation of the error, respectively. Large errors, up to 1 psu at 300 km from the coast are found. Further away (> 400 km), the rmse remains approximately constant at 0.5 psu, for both 10- and 30-day products. Applying the external salinity calibration partially corrects for the coastal-vicinity effect at level 3, particularly in the zone nearer to the coast (Fig. 4.29), helping in the discrimination of shallow-water processes.

4.7 Conclusions

As a conclusion of the first study, the need of using auxiliary data in the *SSS* retrieval from SMOS measurements has been once more remarked. Simulations show that, without any calibration technique, *SSS* gradient of even 5 psu/10° is difficult to discriminate,

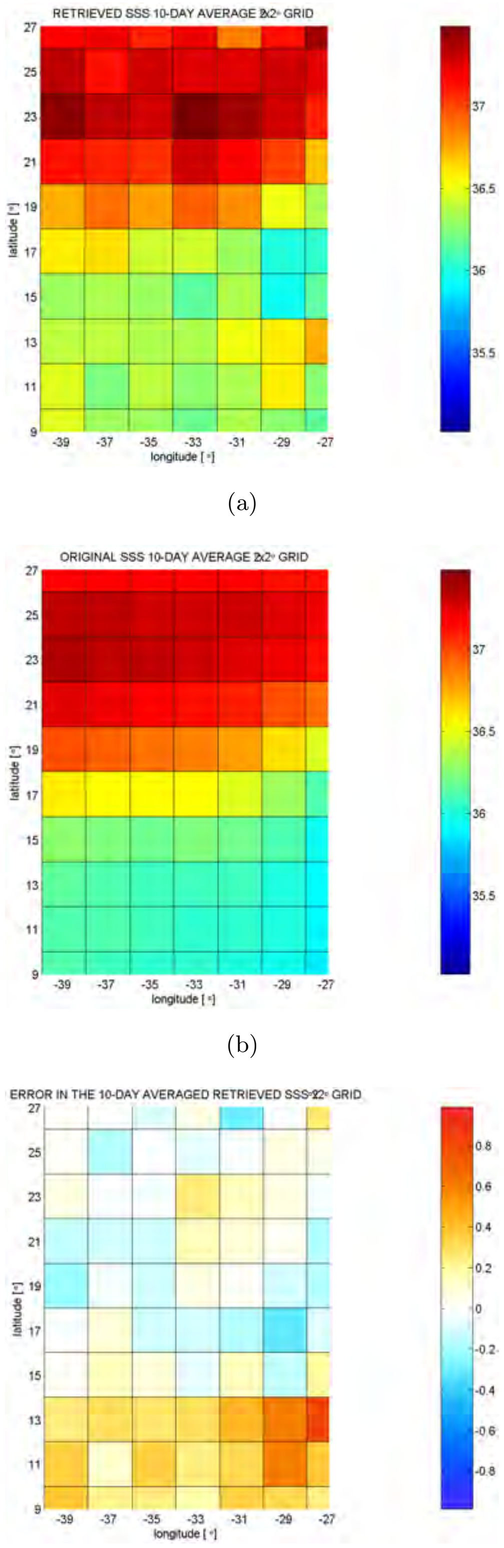

(a)

(b)

(c)

Figure 4.21: Level-3 10-day product: OPEN OCEAN SIMULATION - (a) original values averaged, (b) retrieved salinities averaged, and (c) corresponding error when applying both the external brightness-temperature and salinity calibrations.

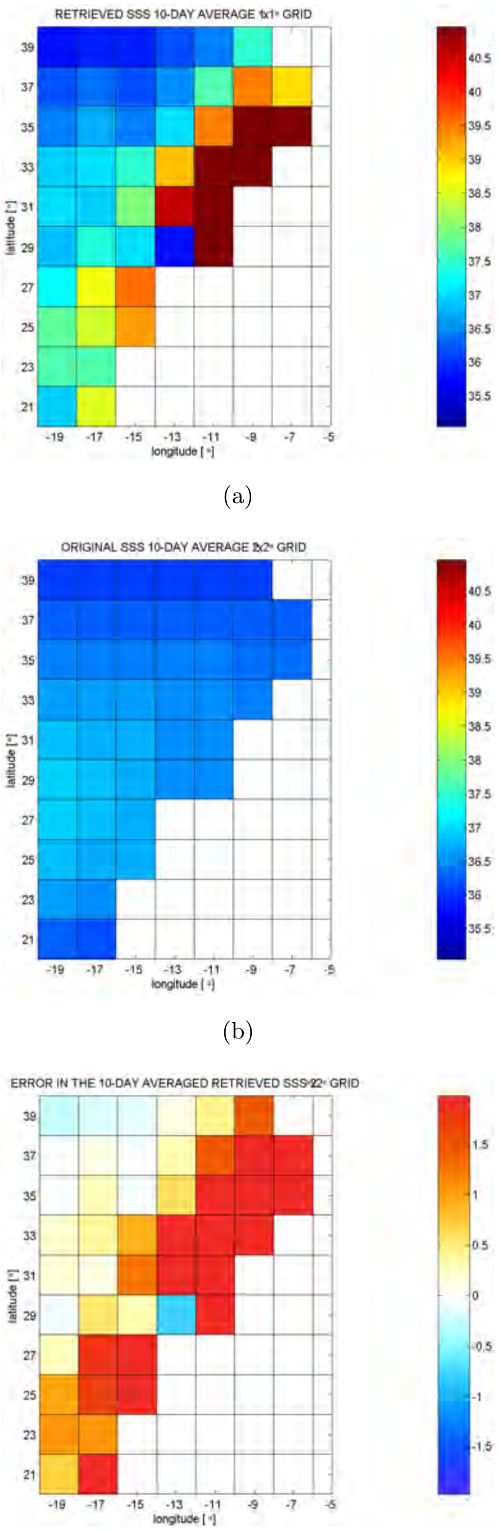

(a)

(b)

(c)

Figure 4.22: Level-3 10-day product: COASTAL REGION SIMULATION - (a) original values averaged, (b) retrieved salinities averaged, and (c) corresponding error when applying both the external brightness-temperature and salinity calibrations.

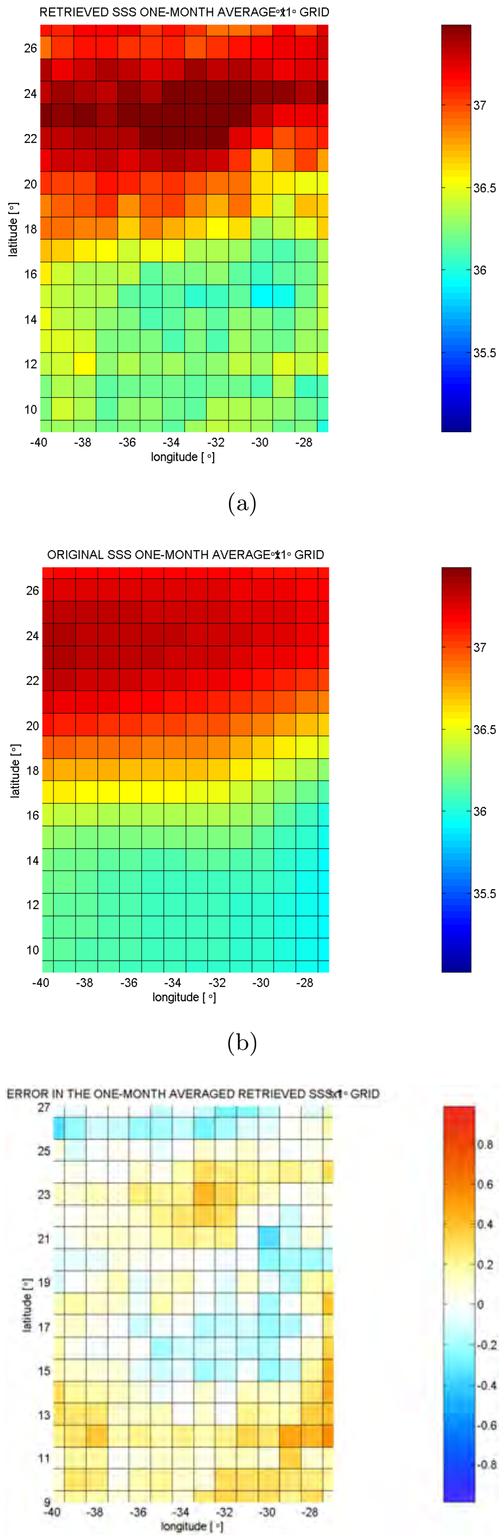

(a)

(b)

(c)

Figure 4.23: Level-3 30-day product: OPEN OCEAN SIMULATION - (a) original values averaged, (b) retrieved salinities averaged, and (c) corresponding error when applying both the external brightness-temperature and salinity calibrations.

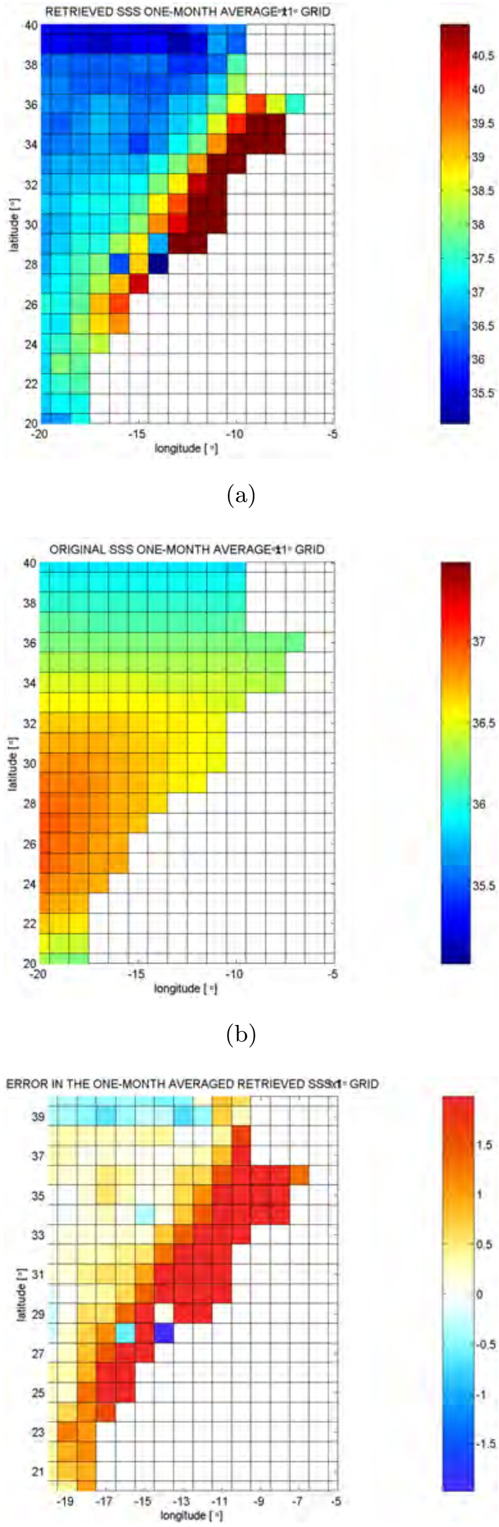

(a)

(b)

(c)

Figure 4.24: Level-3 30-day product: COASTAL REGION SIMULATION - (a) original values averaged, (b) retrieved salinities averaged, and (c) corresponding error when applying both the external brightness-temperature and salinity calibrations.

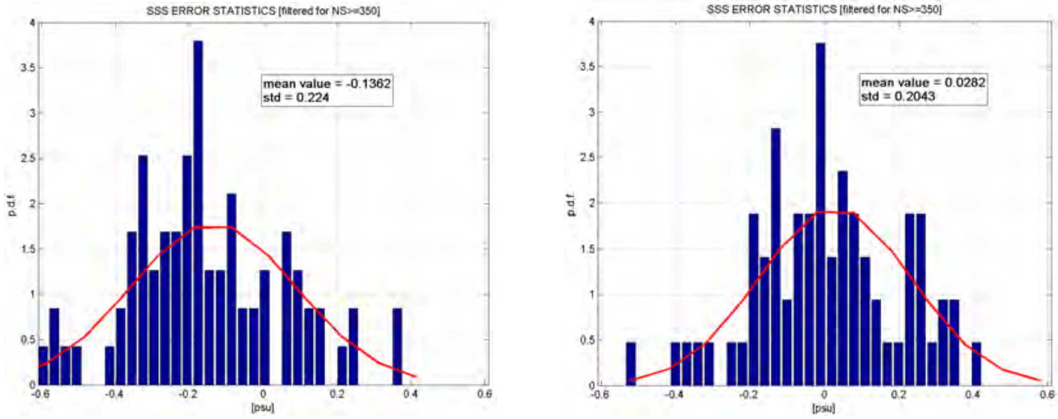

(a) (b)

Figure 4.25: OPEN OCEAN SIMULATION - Histogram of the level 3 retrieved *SSS* error for the 10-day product using (a) only the external brightness temperature calibration and, (b) both external calibrations.

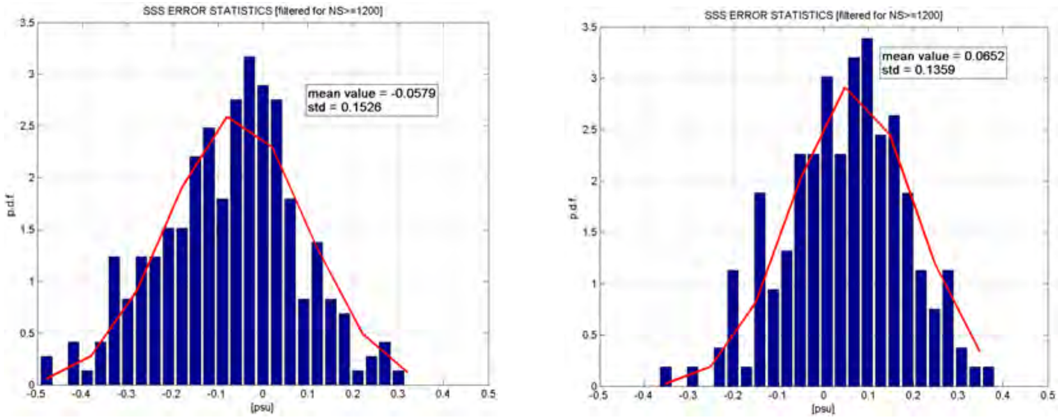

(a) (b)

Figure 4.26: OPEN OCEAN SIMULATION - Histogram of the level 3 retrieved *SSS* error for the 30-day product using (a) only the external brightness temperature calibration and, (b) both external calibrations.

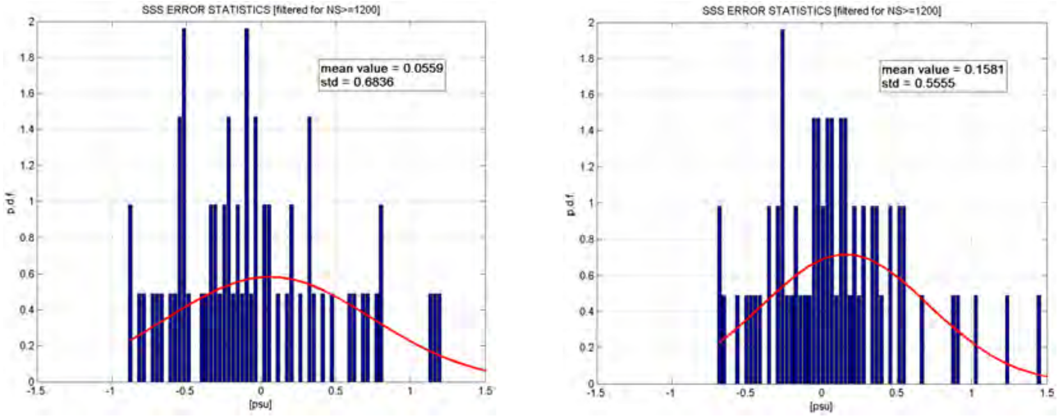

(a) (b)

Figure 4.27: COASTAL REGION SIMULATION - Histogram of the level 3 retrieved *SSS* error for the 10-day product using (a) only the external brightness temperature calibration and, (b) both external calibrations.

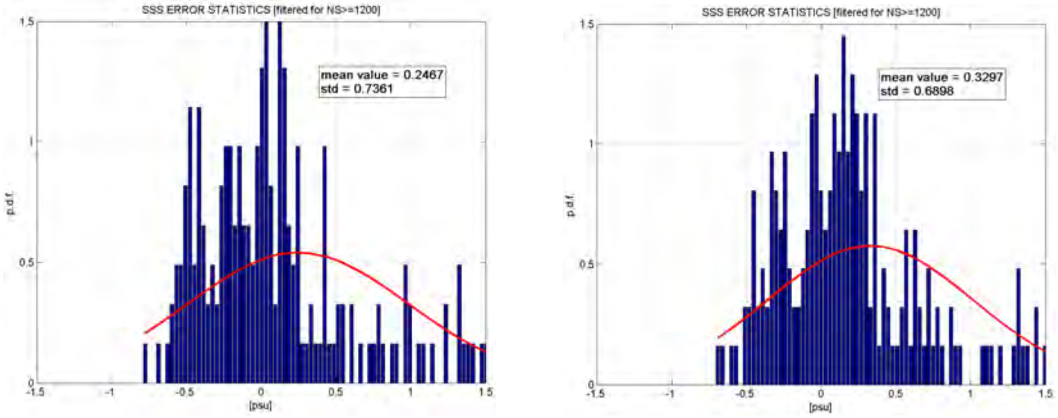

(a) (b)

Figure 4.28: COASTAL REGION SIMULATION - Histogram for the level 3 retrieved *SSS* error for the 30-day product using (a) only the external brightness temperature calibration and, (b) both external calibrations

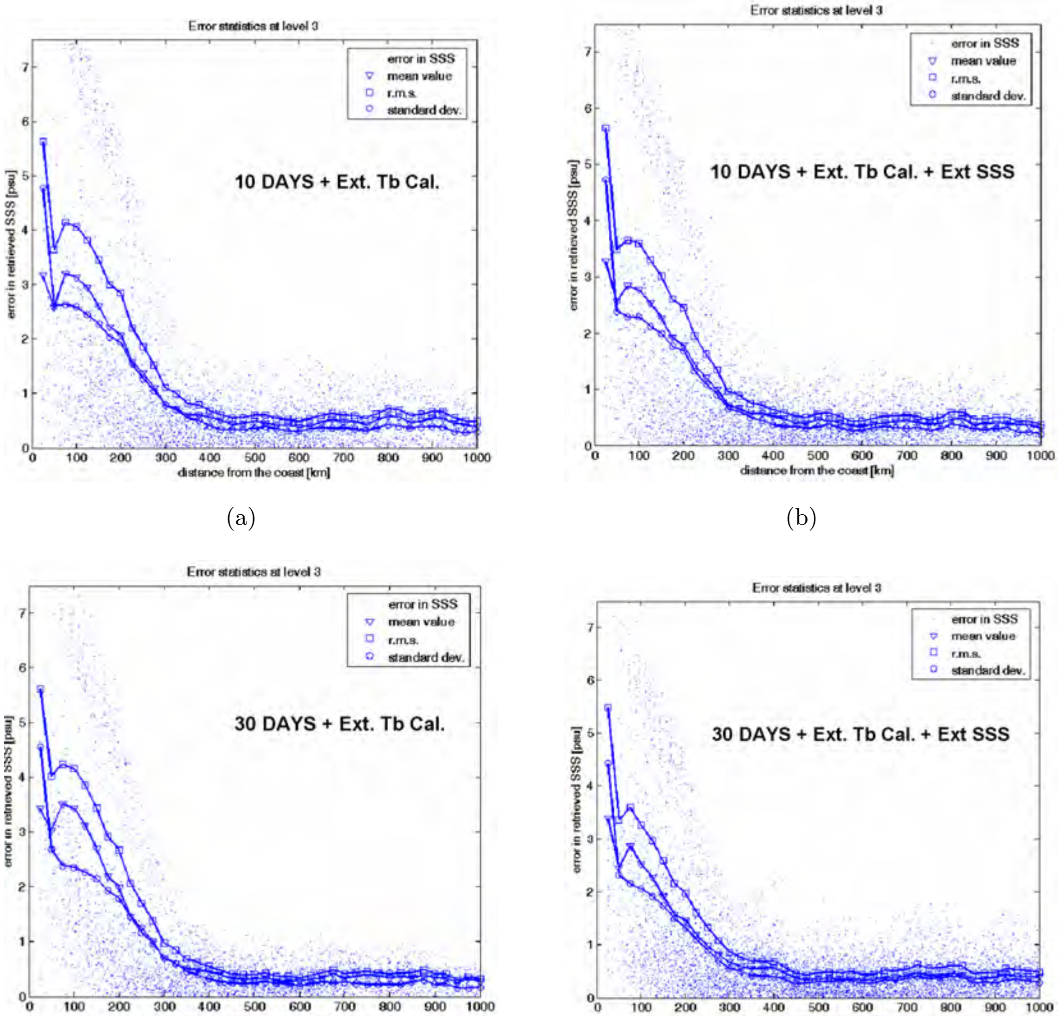

(a)

(b)

(c)

(d)

Figure 4.29: Retrieved *SSS* error as a function of the distance from the coast for (a) and (b) the 10-day and (c) and (d) 30-day Level-3 product, using (a) and (c) only the brightness-temperature calibration or (b) and (d) both calibrations.

even in the most favorable climate conditions (no winds, $SST = 25°C$). On the other hand, helping the retrieval by performing a pre-processing of the SMOS measurements (external brightness temperature calibration (*Camps et al.*, 2004a) and (*Talone et al.*, 2007b)) and/or a post-processing of the retrieved salinity (external salinity calibration (*Talone et al.*, 2007a) and (*Talone et al.*, 2007b)) based on auxiliary data allows discriminating *SSS* gradients as small as 1 psu/10° in a wide range of climatological conditions.

Fostered by the results of the ideal scenario, the two algorithms have been tested in a more realistic environment. Their impact on the Levels 2 and 3 products as well as the coast-proximity effect have been assessed. A complete month has been simulated, using SEPS (*Camps et al.* (2003) and SEPS ADDD) in its full mode and the L2PS, for two different scenarios: one in open ocean and another one in a coastal zone. The *SSS* has been retrieved applying only the external brightness temperature calibration or both the brightness temperature and the salinity calibrations, and the performance of the retrieval has been analyzed and compared to previous studies.

According to the results, it can be concluded that:

At level 2:

1. The external salinity calibration remarkably reduces the retrieved *SSS* mean error, while keeping unchanged the standard deviation, preserving in this way the local variation of salinity within the same snapshot.
2. The mean value of the retrieved *SSS* error is approximately equal to zero, with fluctuations on the order of 0.5 psu, while its standard deviation is almost constant and lower that 1.5 psu within both the so-called “Narrow Swath”.
3. The proximity of the coast degrades the performance of the *SSS* retrieval, increasing the standard deviation of the error by a factor of between 1.5 and 2. Large errors (3 - 4 psu) are found up to 150 km from the coast, and ~1 psu up to 300 km.
4. External salinity calibration slightly decreases the error induced by the coastal proximity: the mean error by 25% (0.5 over 2 psu) and the rms by 10% (0.5 over 5 psu), particularly in the zones with the largest errors (lowest number of observations).

At level 3:

1. The mean error is reduced by more than 15% for the 10-day product and by 5% in the 30-day one.

2. The external salinity calibration only partially mitigates the error caused by the coast proximity for both for the 10- and the 30-day products.
3. Level-3 mean error is dominated by the standard deviation of the Level-2 error, and therefore, averaging does not significantly reduce the *SSS* retrieval error.

5

Cost function improvement: characterization of the misfits covariance matrix

One of the most important topics in the optimization of the level 2 retrieval algorithm is the characterization of the cost function. In this context, the weight to be given to the radiometric measurements with respect to the weight of the auxiliary data is still a pending issue. Two different approach have been followed in litterature, both of them simplifications of the most general formulation. The latter is used to retrieve *SSS* and the results are compared to results of using the two cost funtion in litterature and to another approximation (N_{eff}) based on the analysis of the misfits covariance matrices.

5.1 Introduction

5.1.1 *SSS* retrieval in SMOS

As explained in Section 3.6, the SMOS *SSS* retrieval problem is stated as a Maximum Likelihood Estimation (MLE) method. Considering Gaussian error statistics, the MLE reduces to a least-squares problem leading to the following formulation (Eqns. from Section 3.6 are repeated for the sake of convenience):

$$X^2 = \overline{(F^{meas} - F^{model})}^T \, \overline{\overline{C_1^{-1}}} \, \overline{(F^{meas} - F^{model})} \tag{5.1}$$

where $\left(F^{meas} - F^{model}\right)$ is the misfit (measurement minus model) on the observables (brightness temperatures in T_H or T_V polarizations, or the first Stokes' parameter in brightness temperature T_I), and $\overline{\overline{C_1}}$ is the covariance matrices of the misfits.

Until a proper estimation of $\overline{\overline{C_1}}$, in the official Ocean Salinity Level 2 Processor it is defined as a diagonal and the misfits are considered completely uncorrelated. This consideration is equivalent to write Eqn. 5.1 as:

$$X^2 = \sum_{i=1}^{N_{obs}} \frac{\left[F_i^{meas} - F_i^{model}\right]^2}{\sigma_{F_i}^2}\ , \tag{5.2}$$

where $F_i^{meas,model}$ is the i-th element of $\overline{F_i^{meas,model}}$.

Previous studies (e.g. *Gabarró et al.* (2009)) showed that defining the optimal cost function is not straightforward and that auxiliary external information, in particular wind speed U_{10}, sea surface temperature SST, and possibly modeled or climatological SSS must be added to Eqn. 5.2. Two different cost functions are currently used within the SMOS community, (*Zine et al.*, 2008) and (*Camps et al.* (2005a); *Talone et al.* (2009)) respectively:

$$\begin{aligned} X^2 \ &= \ \sum_{i=1}^{N_{obs}} \frac{\left[F_i^{meas} - F_i^{model}\right]^2}{\sigma_{F_i}^2} + \frac{(SSS - SSS_{aux})^2}{\sigma_{SSS}^2} + \\ &\quad + \frac{(SST - SST_{aux})^2}{\sigma_{SST}^2} + \frac{(U_{10} - U_{10_{aux}})^2}{\sigma_{U_{10}}^2} \end{aligned} \tag{5.3}$$

and

$$\begin{aligned} X^2 \ &= \ \frac{1}{N_{obs}} \sum_{i=1}^{N_{obs}} \frac{\left[F_i^{meas} - F_i^{model}\right]^2}{\sigma_{F_i}^2} + \frac{(SSS - SSS_{aux})^2}{\sigma_{SSS}^2} + \\ &\quad + \frac{(SST - SST_{aux})^2}{\sigma_{SST}^2} + \frac{(U_{10} - U_{10_{aux}})^2}{\sigma_{U_{10}}^2} \end{aligned} \tag{5.4}$$

In both formulations the cost function is composed by two main contributions (or information providers):

- The first term ($\sum_{i=1}^{N_{obs}} \frac{\left[F_i^{meas} - F_i^{model}\right]^2}{\sigma_{F_i}^2}$) is representative of MIRAS measurements and modeled observables $\left(F_i^{meas}, F_i^{model}\right)$, weighted by the radiometric noise for the i-th observation as in Eqn. 5.2;

- The constraints for the auxiliary *SSS*, *SST* and 10-meter height wind speed U_{10} (as sea surface roughness descriptor) are the second, third and fourth terms, respectively ($\frac{(SSS-SSS_{aux})^2}{\sigma^2_{SSS}} + \frac{(SST-SST_{aux})^2}{\sigma^2_{SST}} + \frac{(U_{10}-U_{10_{aux}})^2}{\sigma^2_{U_{10}}}$). These are weighted by the inverse of the variance of the misfit existing considering the corresponding auxiliary field with respect to the original one, as defined in Eqn. 5.5:

  $$\sigma_p^2 = \frac{1}{N}\sum_{i=1}^{N}\left(p_{mis} - \left(\frac{1}{N}\sum_{j=1}^{N} p_{mis_j}\right)\right)^2, \tag{5.5}$$

  where N is the total number of points taken into consideration, $p_{mis} = p_{aux} - p_{orig}$, and where *mis* stands for misfit, *aux* for auxiliary, *orig* for original, and p for *SSS*, *SST*, or U_{10}.

In the real SMOS case (not simulation), p_{orig} is not known and σ_p^2 allows weighting the *a priori* information on the value of the geophysical parameter. The value of σ_p^2 is representative of the reliability of this information: large σ_p^2 indicates that the estimation is not reliable, leading to very small weight within the total X^2 minimization, and vice-versa. In both Eqns. 5.3 and 5.4, as described in previous studies (*Font et al.* (2005); *Sabia et al.* (2006)) constraints on *SSS* are not taken into account by using a very large value for σ^2_{SSS}.

The difference between the two formulations lies in the factor weighting the observables term in Eqn. 5.4. Actually, Eqns. 5.3 and 5.4 represent two extreme cases; in the first one each misfit is assumed to provide the maximum information content, their contributions are thus summed up (once squared and normalized by the radiometric noise) to construct the brightness temperatures term in the cost function (Eqn. 5.3); the second option is appropriate for the case of completely redundant samples; the average contribution is used to define the cost function in Eqn. 5.4.

5.1.2 Expected correlation in the brightness temperatures

Due to the MIRAS characteristics, some correlation is expected between the brightness temperature errors of different grid points within the same snapshot and among consecutive snapshots. Any imaging radiometer, in fact, is affected by three types of noise:

- the radiometric sensitivity (ΔT): temporal standard deviation of the zero-mean random error due to the finite integration time;
- the radiometric bias: spatial average of all the systematic errors; and
- the radiometric accuracy: spatial standard deviation of the sum of all the systematic errors (*Torres et al.* (2005); *Font et al.* (2008)).

The first type of noise is random within the same snapshot as well as from snapshot to snapshot. The second and third types are random within the same snapshot, but systematic from one snapshot to another, and are responsible for the aforementioned correlation. In addition to that, concerning SMOS, two other sources of spatial correlation can be identified:

1. the potential systematic errors in the image reconstruction (*Butora and Camps* (2003); *Camps et al.* (2008a); *Anterrieu and Camps* (2008)); and
2. the finite spatial resolution of the instrument, which is, on average, larger than the Icosahedral Snyder Equal Area hexagonal grid of aperture 4 and resolution 9 (ISEA 4H9) (*Snyder*, 1992) in which Level 2 data will be obtained (50 km average SMOS resolution vs. 15 km ISEA 4H9 grid size).

The different phases in which correlation can be introduced in the SMOS processing chain are shown in Fig. 5.1: correlation enters at both level 0 (visibilities measurement) and level 1 (image reconstruction, and projection of the brightness temperatures).

The correlation among different grid points of the same snapshot is, in summary, due to the fact that the projected synthetic antenna pattern (which involves radiometric accuracy, radiometric bias, image reconstruction algorithm, and projection) presents a correlation length larger than its projection grid. Considering a change of reference frame, from the satellite's to the Earth's, one grid point observes the satellite, whose antenna pattern changes with a correlation length larger than the time between snapshots. Taking into account the retrieval process, it results in a loss of the information provided by the observables with respect to the background terms. As already mentioned, two different approaches have been followed so far concerning salinity retrieval from MIRAS brightness temperatures: misfits can be, once squared and normalized, summed up (Eqn. 5.3) (*Zine et al.*, 2007), or averaged (Eqn. 5.4) (*Camps et al.* (2005a); *Talone et al.* (2009)). On the other hand, the correlation induced by the instrument generates an intermediate and more complex situation between Eqns. 5.3 and 5.4.

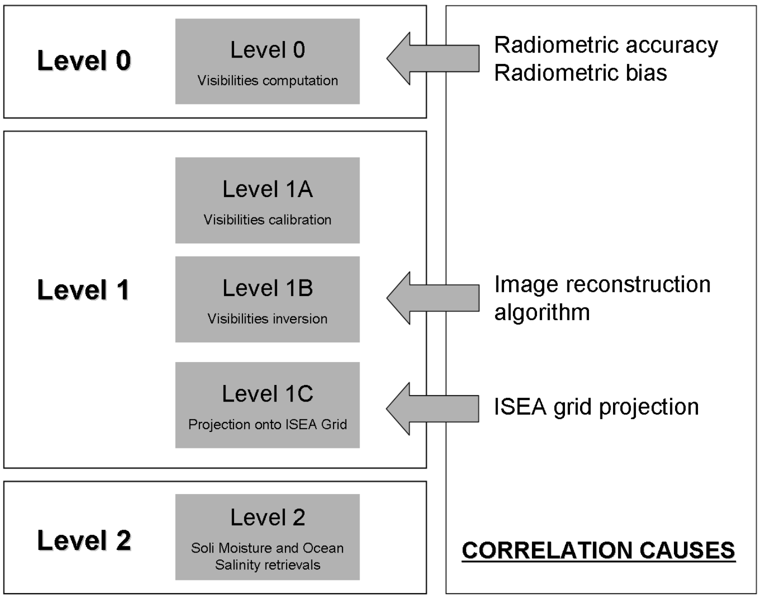

Figure 5.1: The different phases in which correlation can be introduced in the SMOS processing chain, it enters at both level 0 and level 1.

The simulation scenario is presented in Section 5.2. The level of correlation of the measurement errors, and thus the weight to be given to the observables term in the cost function is assessed in Section 5.3, where the covariance matrices are estimated, and a new weight regarded as the *"effective number of observations"* is introduced. The comparison of the retrieval results using the four formulations is presented in Section 5.4, and, finally, the main conclusions of this work are summarized in Section 5.5.

5.2 Simulation Scenario

Since at the time of performing this study SMOS outputs were not yet fully calibrated, SMOS-like brightness temperatures were simulated using the SMOS End-to-end Performance Simulator (SEPS) (*Camps et al.* (2003); SEPS ADDD) in its full mode (including co- and cross-pol measured antenna patterns for each antenna, all instrument errors, noise injection calibration and, G-matrix image reconstruction). To model sea surface emission, Klein and Swift model (*Klein and Swift*, 1977) and Hollinger's measurements (*Hollinger*, 1971) linear fitting have been used for the seawater dielectric constant and the wind speed contribution to brightness temperature, respectively. Since the objective of this study is the estimation of the correlation induced by the instrument and

in order to avoid further contributions from other sources, the radiometric sensitivity has been set to zero in the simulation, increasing the integration time to very large values (*Randa et al.*, 2008) ($\tau \rightarrow \infty \Rightarrow \Delta T \rightarrow 0K$). Sixty-four ascending and descending overpasses have been simulated during the month of March 2007 (SEPS time), and consisting, on average, of more than 200 snapshot each.
Concerning the geophysical parameters, two databases are defined:

- Original Data (used to feed SEPS and generate the Brightness Temperatures): Daily outputs of a 0.5° configuration of the NEMO-OPA ocean model (*Madec* (2008); *Mourre et al.* (2008)) are used as original SSS and SST, while fields come from ECMWF (European Centre for Medium-range Weather Forecasting) ERA-40 reanalysis (*Uppala et al.*, 1996);

- Auxiliary Data (used in the Level 2 cost function, Eqns. 5.3 and 5.4): SSS and SST come from Levitus climatology (*Levitus*, 1998), and are extracted from the NCEP (National Centers for Environmental Prediction) NCAR reanalysis (*Kalnay et al.*, 1996);

5.3 Methodology

As in chapter 4, simulations have been carried out following these steps:

- SEPS-generated brightness temperatures (Fig. 4.14a, repeated here as Fig. 5.2a for convenience) have been masked to eliminate the transition areas at the beginning and at the end of the sequence. The number of observations for one of the ascending overpasses is shown in Fig. 4.14b (repeated here as Fig. 5.2b for convenience), as an example, as a function of the distance to the ground track.

- Selected brightness temperatures have been compared to the ones resulting from running only the forward model (using the same geophysical and orbital parameters). The difference between them is the instrument-induced radiometric error (radiometric bias plus radiometric accuracy, since radiometric sensitivity has been set to zero).

- The calculated differences have been sorted and grouped by number of observations. For each of the bins, the covariance matrix has been computed: for each one of the nth observation samples, the Galton-Pearsons correlation coefficient (*Rodgers and Nicewander*, 1988) has been calculated between all the possible pairs to construct the covariance matrices (estimate of $\overline{\overline{C_1}}$ in Eqn. 5.1). Bins with number of samples smaller than the number of observations have not been taken into account because do not provide representative results.

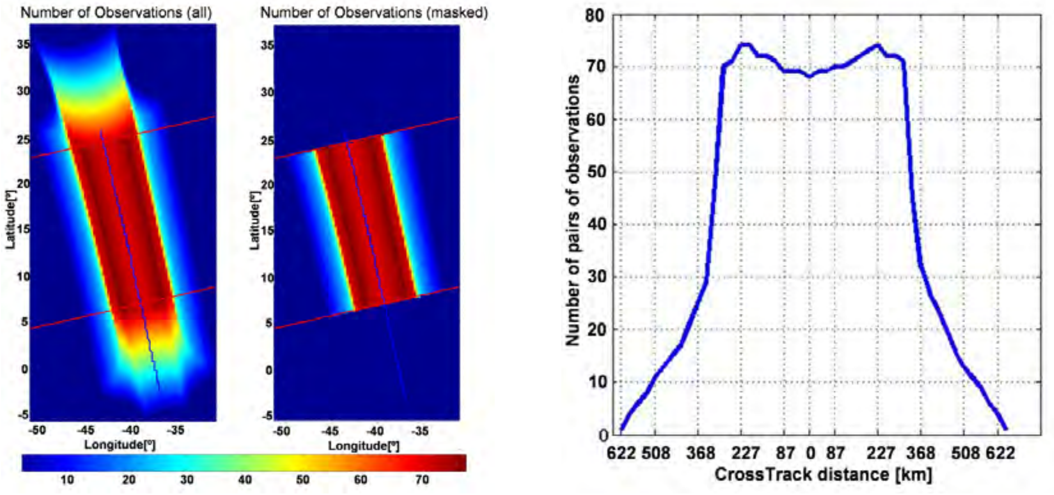

(a) (b)

Figure 5.2: Selection of the fully observed points. (a) Example of selection; and (b) Number of pairs of observations as a function of the Cross-Track position.

Sea surface salinity retrievals for all the sixty-four overpasses have been performed using the estimated covariance matrices as expressed by Eqn. 5.6.

$$\begin{aligned} X^2 &= \overline{(F^{meas}-F^{model})^T}\,\overline{\overline{C_1^{-1}}}\,\overline{(F^{meas}-F^{model})} + \frac{(SSS-SSS_{aux})^2}{\sigma^2_{SSS}} + \\ &+ \frac{(SST-SST_{aux})^2}{\sigma^2_{SST}} + \frac{(U_{10}-U_{10_{aux}})^2}{\sigma^2_{U_{10}}} \end{aligned} \tag{5.6}$$

Results have been considered as a master case to be compared with the various approximations of the cost function.

At this stage, aiming at adapting the current cost functions to the characteristics of the misfits covariance matrix, a new weight is defined. To do so, an analysis of the estimated covariance matrices has been carried out. The eigenvector decomposition has been applied to the inverse covariance matrices $\overline{\overline{C_1}}$ and the number of eigenvectors describing 99% of the variance has been defined as the effective number of measurements, N_{eff}.

To test the impact of introducing N_{eff} in the cost function, the *SSS* for the simulated scenario has been retrieved by means of the Level 2 Processor (*Talone et al.*, 2007b), the cost function in Eqn. 5.7:

$$\begin{aligned} X^2 &= \frac{N_{eff}}{N_{obs}} \sum_{i=1}^{N_{obs}} \frac{\left[F_i^{meas} - F_i^{model}\right]^2}{\sigma_{F_i}^2} + \frac{(SSS - SSS_{aux})^2}{\sigma_{SSS}^2} + \\ &+ \frac{(SST - SST_{aux})^2}{\sigma_{SST}^2} + \frac{(U_{10} - U_{10_{aux}})^2}{\sigma_{U_{10}}^2}. \end{aligned} \tag{5.7}$$

Results have been compared to the case of using Eqns. 5.3, 5.4, or 5.6 as cost function. According to (*Font et al.* (2005); *Sabia et al.* (2006)), constraints on the *SSS* have not been taken into account ($\sigma_{SSS} \rightarrow \infty$). The same forward models used in SEPS have been applied for the retrieval.

5.4 Results

Firstly, the covariance matrices have been calculated and analyzed. In Fig. 5.3 one case of covariance matrix (78 pairs of $T_H - T_V$ observations) is presented, the matrix is plotted for (a) the H-pol, (b) the V-pol, and (c) the first Stokes parameter in brightness temperature (T_I) (*Randa et al.*, 2008); the color scale is in dB ($10log_{10}$). Correlation clusters are evident in Fig. 5.3, as foreseen in *Butora and Camps* (2003).

Results concerning the effective number of observations (N_{eff}) (section 5.3) are shown in Fig. 5.4 for (a) H-pol, (b) V-pol, and (c) the first Stokes parameter in brightness temperature (T_I). The number of ($T_H - T_V$) pairs (approximately half of the number of observations) is represented on the abscissa, and the ordinate shows the ratio between the effective number of observations N_{eff} and the total N_{obs}. The ratio N_{eff}/N_{obs} is shown as a density plot, being the color the occurrence along the whole month simulated, the solid line is the linear fitting of N_{eff}. Figure 5.4d is the normalized (so that the integral is equal to 1) histogram of the number of observations.

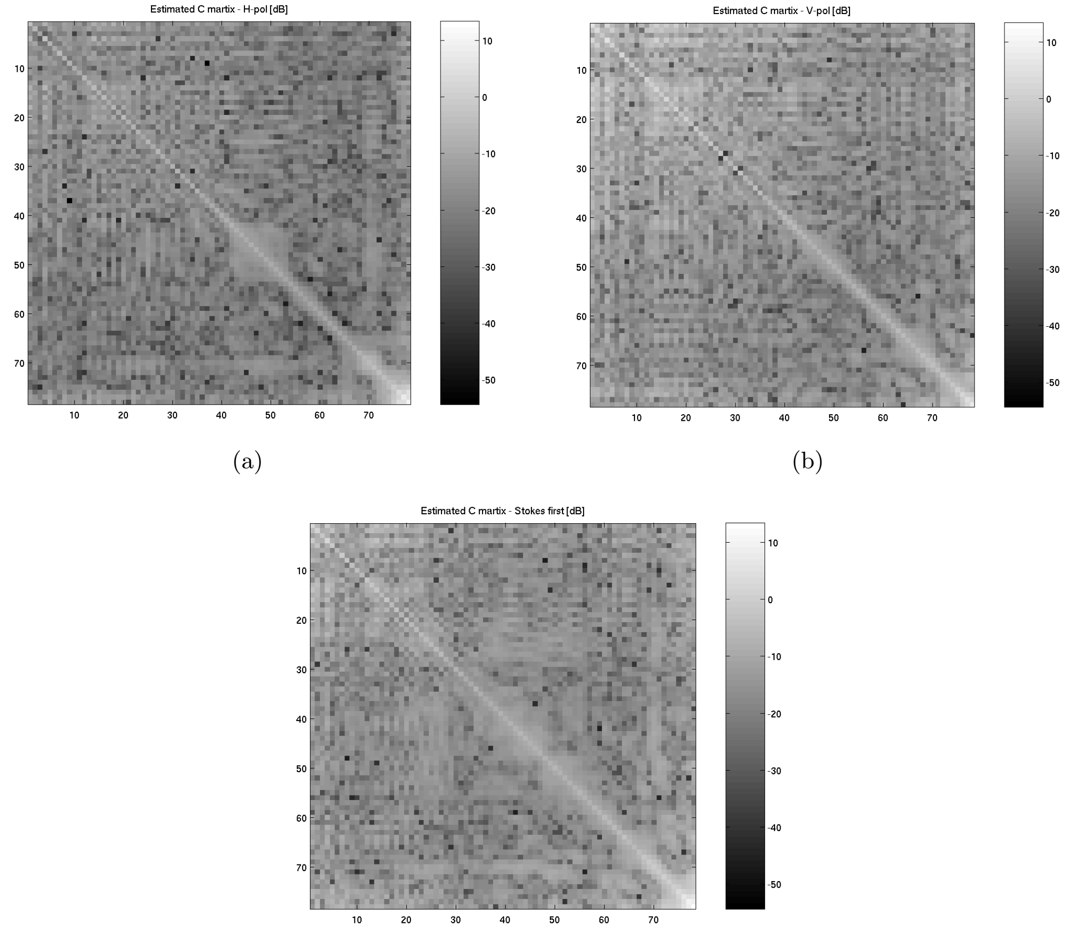

(a)

(b)

(c)

Figure 5.3: Example of estimated covariance matrix in the case of 78 observation pairs for (a) H-pol, (b) V-pol, and (c) the first parameter of Stokes in brightness temperature. Units are in dB.

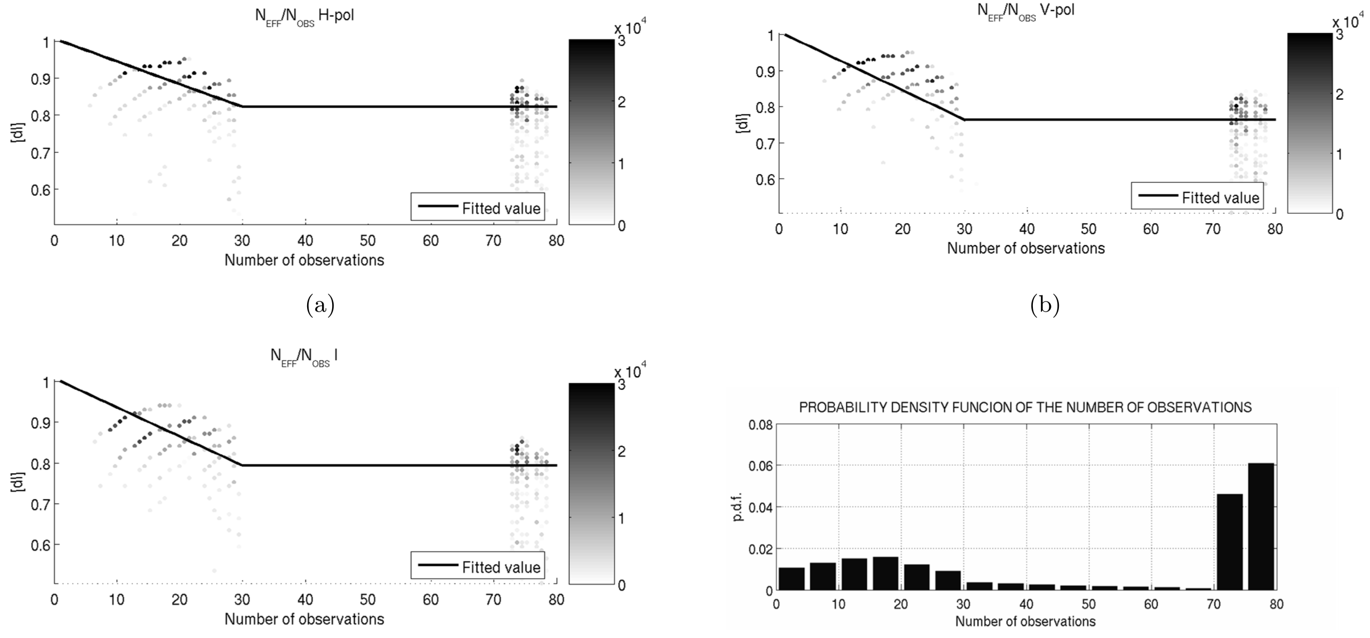

(a) (b)

(c) (d)

Figure 5.4: Ratio between the effective number of measurements and the total number of observations, for the (a) H-polarization, the (b) V-polarization, and (c) the first Stokes parameter in brightness temperature (T_I), (d) normalized histogram of the number of observation. In Figs. (a), (b) and (c) the ratio N_{eff}/N_{obs} is shown as a density plot, being the color the occurrence along the whole month simulated; the solid line is the linear fitting of N_{eff}.

Even though some differences can be noticed between T_H, T_V, and T_I (H gives higher results), the trend is very similar, and two different regimes can be observed: for $N_{obs} \in (1, 30]$, N_{eff} changes from being equal to N_{obs} to the asymptotic value of $0.82 \cdot N_{obs}$ for the H-pol, $0.76 \cdot N_{obs}$ for the V-pol, $0.79 \cdot N_{obs}$ for T_I, when is $N_{obs} \geq 31$ (distance to ground-track $<$ 350 Km) the ratio N_{eff}/N_{obs} remains almost constant. The regime change around 30 observations can be explained observing Figs. 5.4d and 5.2b: in the former figure the probability density function of the number of observations is shown, whereas in the latter figure the number of observations is presented as a function of the cross-track distance. As it can be noticed, very few points are observed between 30 and 70 times due to the very steep increase of N_{obs} shown in Fig. 5.2b. This particular behavior of the SMOS FOV is also the cause of the lack of estimates of N_{eff} between $\sim$ 30 and $\sim$ 70 pairs of observations in Figs. 5.4a, 5.4b, and 5.4c; as explained in Section 5.2, in fact, when only few measurements are available for a certain N_{obs}, the covariance matrix is not calculated since it is not considered representative. This pattern suggests an unambiguous way of defining the useful swath width of an SMOS overpass at approximately 700 km, a bit larger than the official Q-Swath or Narrow Swath (631 640 km) (SEPS SUM; *Barré et al.* (2008)).

Considering the cost function definition, the three configurations can be summarized by Eqn. 5.8, being $W \in \{N_{obs}, 1, N_{eff}\}$ in the case of equations 5.3, 5.4, and 5.7, respectively:

$$\begin{aligned} X^2 &= \frac{W}{N_{obs}} \sum_{i=1}^{N_{obs}} \frac{\left[F_i^{meas} - F_i^{model}\right]^2}{\sigma_{F_i}^2} + \frac{(SSS - SSS_{aux})^2}{\sigma_{SSS}^2} + \\ &+ \frac{(SST - SST_{aux})^2}{\sigma_{SST}^2} + \frac{(U_{10} - U_{10_{aux}})^2}{\sigma_{U_{10}}^2} \end{aligned} \tag{5.8}$$

Figure 5.5 shows W/N_{obs} as a function of the total number of observations. The N_{eff} calculated for the first parameter of Stokes in brightness temperatures is marked with the solid line, the dashed and dash-dot lines stand for the cases in Eqn. 5.3 and 5.4, respectively,

$$\left(\frac{N_{eff}}{N_{obs}}\right)' = \{ \begin{array}{ll} 1.0362 - 0.008 \cdot N_{obs} & for N_{obs} \leq 30 \\ 0.793 & for N_{obs} \geq 31 \end{array} \tag{5.9}$$

whereas the symbol $()'$ here indicates the fitting result and not the calculated N_{eff}/N_{obs}.

As can be observed, N_{eff} takes intermediate values between 1 and N_{obs}, as expected.

The four configurations (using the cost functions defined in Eqn. 5.6 (master), Eqn. 5.3 ($W = N_{obs}$), Eqn. 5.4 ($W = 1$) and Eqn. 5.7 ($W = N_{eff}$)) have been tested and results have been compared. *SSS* has been retrieved using the brightness temperature resulting from simulating the same scenarios, but applying now the SMOS nominal value for the integration time ($\tau = 158\ \ ms$).

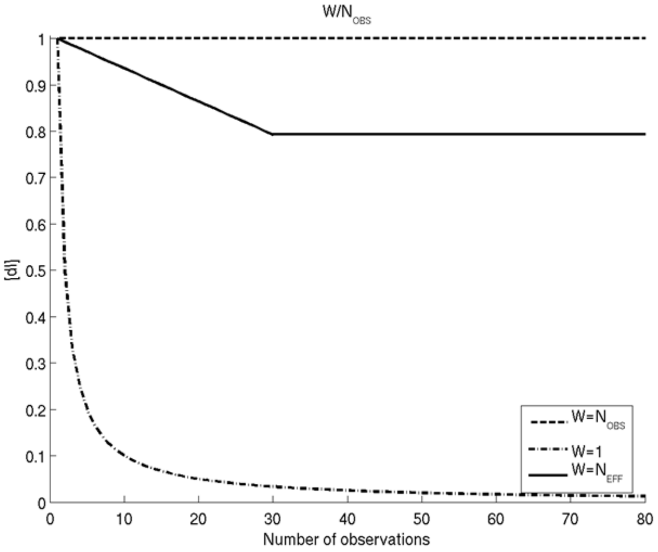

Figure 5.5: Weight given to average the observables term in the cost function as a function of the number of observations in the case of using (dashed line) Eqn. 5.3 ($\mathbf{W} = \mathbf{N_{obs}}$), (dash-dot line) Eqn. 5.4 ($\mathbf{W} = \mathbf{1}$) , and (solid line) the fitted value Eqn. 5.7 ($\mathbf{W} = \mathbf{N_{eff}}$).

Error statistics considering only the grid points fully observed for all the sixty-four overpasses are summarized in Table 5.1 through its mean value μ, standard deviation σ, and rms (defined as $\sqrt{\sum_{i=1}^{N} (SSS_{err_i})^2/N}$), (with N being the total number of grid points taken into account), and the X^2 factor. The latter is defined as the quadratic sum of the difference between the retrieved *SSS* error normalized histogram (observable) and the pdf of a normal distribution with the same mean and variance (model), weighted by the uncertainty associated to each observation, as expressed in Eqn. 5.10 (*Barlow*, 1989):

$$X^2 = \sum_{i=1}^{N} \frac{|P(SSS_{err})|^2}{\sigma_i^2}. \tag{5.10}$$

The normalized (as in Fig. 5.4, the integral is equal to 1) histograms of the *SSS* retrieval error using Eqns. 5.6, 5.3, 5.4, and 5.7 is shown in Figs. 5.6a, 5.6b, 5.6c, and

Table 5.1: Retrieval performance using C-matrix, and $W = N_{obs}$, 1, and N_{eff} as cost function in terms of mean value (μ), standard deviation (σ), rms, and X^2

SSS	μ [psu]	σ [psu]	*rms* [psu]	X^2 [dimensionless]
$C - matrix$	0.46	3.75	3.78	0.89
$W = N_{obs}$	0.06	2.39	2.39	5.45
$W = 1$	0.06	2.39	2.39	5.27
$W = N_{eff}$	0.07	2.39	2.39	5.43

5.6d, respectively. In order not to alter the results σ_i^2 in Eqn. 5.10 has been considered constant and equal to 1; to calculate X^2, both the *SSS* error and the Gaussian pdf have been quantisized in 0.1-psu bins (the expected resolution of SMOS at Level 2 in one overpass), moreover the sum, that should be calculated in the interval $(-\infty, \infty)$ has been computed only for the interval (-10 psu, 10 psu).

According to Table 5.1, retrieval results are only slightly affected by the change of W , since for all the configurations the rms error is constant at 2.39 psu, with very high X^2 ($\sim 5.2 - 5.4$). The difference is, instead, noticeable if compared with the case of using directly the covariance matrices in the retrieval. In this case, the rms error is equal to 3.78 psu (mostly due to the increase of error standard deviation σ (3.75 psu)); on the other hand, error statistics are much more Gaussian presenting a $X^2 = 0.89$. Comparing Figures 5.6a, 5.6b, 5.6c, and 5.6d it is evident how results are better when using whichever of Eqns. 5.3, 5.4 or 5.7; nevertheless, the low Gaussianity of the error is also manifest, indicating that some artifacts are introduced in the retrieval procedure which are probably due to the high weight given to the constraints of the auxiliary parameters. Previous studies (*Sabia et al.* (2010); *Gabarró et al.* (2009)) remarked the necessity of correctly balancing the different terms in the cost function. According to the results of this study, the inclusion of the brightness temperature misfit covariance matrices should be taken into account in the choice of the relative weights, since it strongly affects performance.

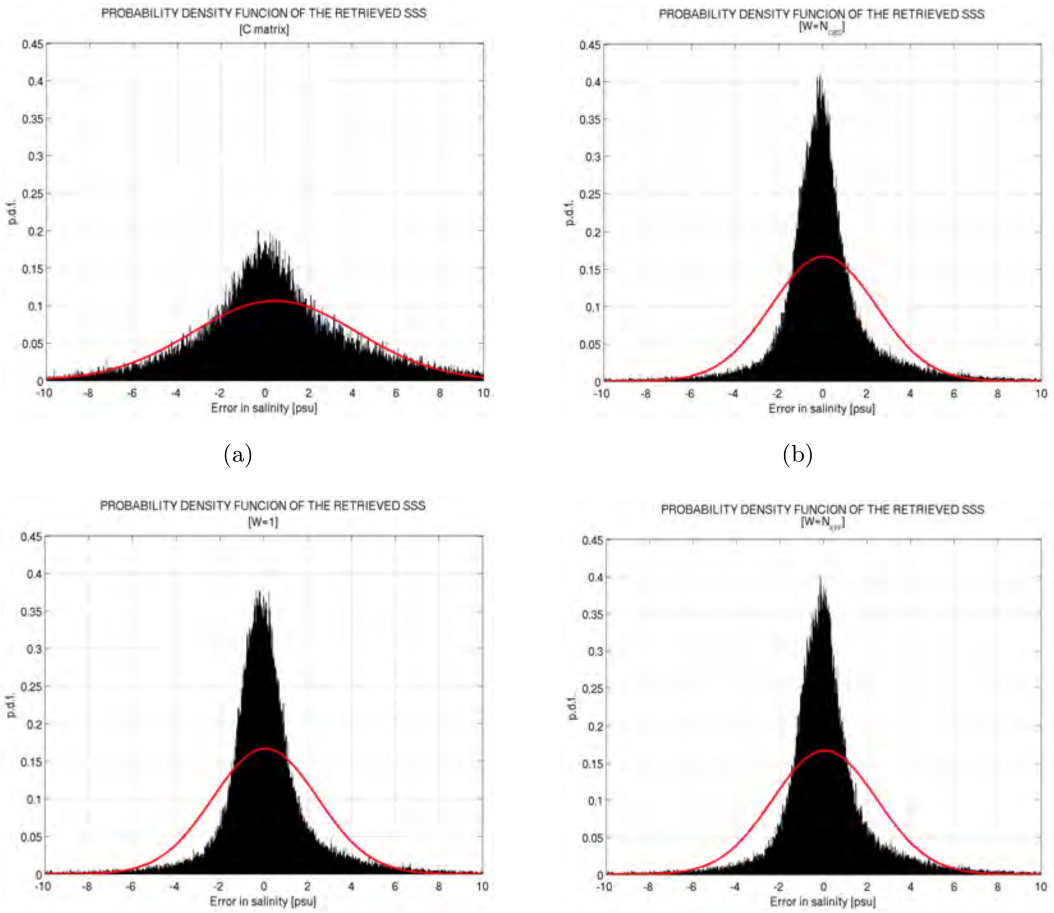

(a) (b)

(c) (d)

Figure 5.6: Retrieved *SSS* error statistics for all the sixty-four overpasses in the case of using as cost function the (a) Eqn. 5.6, (b) Eqn. 5.3, (c) Eqn. 5.4, and (d) Eqn. 5.7. The solid line stands for the normalized Gaussian pdf with the same mean value and standard deviation of the retrieved *SSS* error.

5.5 Conclusions

In order to improve the characterization of the cost function used in the SMOS Ocean Salinity Level 2 Processor, the correlation between measurement misfits has been analyzed. Correlation is expected due to the intrinsic nature of any imaging radiometer, to the possible structures induced by the image reconstruction algorithm, and, finally, to the projection of the brightness temperatures onto the ISEA grid. To assess this point, one complete month of overpasses (64 in total) in the North Atlantic Ocean have been simulated using the SMOS End-to-end Performance Simulator (SEPS) in its full mode (SMOS first measurements are, in facts, not yet fully calibrated). SMOS-Level 2 Processor Simulator (SMOS-L2PS) has been used to retrieve SSS from the brightness temperatures calculated by SEPS. As geophysical input parameters (original and auxiliary data), a North-Atlantic configuration of the NEMO-OPA ocean model and the Levitus climatology has been used for SSS and SST, while ECMWF-ERA40 and NCEP/NCAR products have been chosen for U_{10}.
The SEPS-simulated brightness temperatures have been compared to the ones obtained by directly forwarding a brightness temperature model to estimate the correlation of the radiometric errors induced by the instrument. To do so, the covariance matrices of the misfit between the SEPS-retrieved and the forward model brightness temperatures, sorted and grouped by the number of observations (N_{obs}), have been computed. In addition to that, as a test, Eigenvalues Decomposition has been applied and the number of eigenvectors required to describe the 99% of the variance has been defined as the effective number of measurements (N_{eff}). Its trend as a function of the number of observations has been analyzed, and the results suggest the presence of two regimes: the first one noise-dominated, where N_{eff} is almost equal to N_{obs}; and the second one where N_{eff} increases with N_{obs} according to the constant slope of 0.8. Introducing N_{eff} in the cost function resulted in applying a weight to the average residual term of the observational part of the SMOS Ocean Salinity Level 2 cost function equal to the factor N_{eff}/N_{obs} . The consequent impact has been assessed comparing the retrieval performance with that obtained using directly the estimated covariance matrices or both the cost function present in the SMOS literature. Conclusions can be summarized by the following three points:

- Based on the two regimes of N_{eff}, a threshold can be established to define unambiguously the useful swath of SMOS as 700 km centered on the satellite groundtrack, where the relation N_{eff}/N_{obs} is almost one.
- The cost function analysis suggests that the current configurations (Eqns. 5.4 and

5.7), although ensuring better performance, may be introducing non-linearities in the retrieval procedure if compared to the results obtained using directly the misfit covariance matrices. According to previous studies, non-linearities may be due to a non-optimum balancing of the cost function that should be modified.

- Furthermore, the inclusion of the brightness temperature misfit covariance matrices strongly modifies the error statistics and should be taken into account in the choice of the relative weights to be applied to the auxiliary parameters.

6

SSS retrievals using experimental data

As explained in the previous chapters (section 3.6, 4.2, and 6.3), several configurations of the cost function (*Zine et al.* (2008) and *Gabarró et al.* (2009)) as well as pre- and post-processing techniques (*Camps et al.* (2005a) and *Talone et al.* (2009)) have been tested on simulated brightness temperatures. However, until recently, due to the unavailability of real brightness temperature collected by aperture synthesis radiometers, no validation has been carried out, except for the processing of the measurements acquired by the SMOSillo (MIRAS Demonstrator) on June, 20th 2006, which was a first attempt to test the algorithms over a freshwater zone (lake Lohja, West of Helsinki) (*Duffo et al.* (2007) and *Camps et al.* (2008b)).

In this chapter, two experiments of processing real synthetic aperture radiometric data are presented: the first using data acquired by the Helsinki University of Technology (HUT) -2D radiometer during the SMOS Calibration and Validation Phase Rehearsal; and the second one using ten days of real SMOS' measurements.

6.1 The HUT-2D Case

6.1.1 The HUT-2D campaign in the Gulf of Finland

On August 13^{th} and 15^{th}, 2007 two series of flights (SD1 and SD2) were carried out over the Gulf of Finland, back and forth along a straight line, in a zone bounded by latitudes 60.40° and 60.30° North, and longitudes 26.45° and 26.68° East. On both days, starting at 22.00 h, and during approximately 2.30 hours, radiometric measurements and in situ data were acquired, including one ship transect and 20 and 21 flights for SD1 and SD2, respectively. Measurements were collected over the estuaries of several rivers, where fresh water coming from inland mixes with the saltier water of the Gulf of Finland, producing a strong salinity gradient (from almost 0 psu to 4 psu).

On one hand brightness temperatures were measured by the HUT-2D radiometer (*Rautiainen et al.* (2007); *Rautiainen et al.* (2008)). HUT-2D is a two-dimensional synthetic aperture radiometer designed and built by the Helsinki University of Technology. It works at L-band, with a central frequency of 1407 MHz and a bandwidth of 7 MHz. HUT-2D has a total of 36 antennas, arranged in a U shape (12 per arm) and spaced . As in any synthetic aperture radiometer, brightness temperatures are not directly measured by the instrument; in fact, it measures complex cross-correlations between antenna pairs (visibilities). To derive brightness temperatures from the measured visibilities, the Fourier transform can be applied as a first approximation or a more sophisticated G-matrix inversion (*Anterrieu and Camps* (2008); *Camps et al.* (2008a)), can be used. The result is a 2D brightness temperature image snapshot of the radiometers Field of View. Since the distance between elements does not satisfy the Nyquist Criterion ($d \geq \lambda/2$ for this type of arrray), part of the Field Of View (FOV) is affected by aliasing. In the case of HUT-2D, the Alias-Free Field Of View (AF-FOV), the only zone used in the retrieval, looks like a distorted rhombus at the center of the FOV (*Kainulainen et al.*, 2007). Using this AF-FOV, brightness temperatures can be measured under incidence angles between 0° and 40° (*Kainulainen et al.* (2007), Fig. 2). HUT-2D was mounted, nadir-looking, on the Short SC-7 Skyvan aircraft of the Laboratory of Space Technology of the Helsinki University of Technology (HUT Skyvan website: http://radio.tkk.fi/en/research/space_technology/SkyVan.html). On the other hand, on a vessel navigating at the same time along the aircraft ground-track, SST was measured using a manual digital thermometer and surface water samples were collected every 150 m. Samples were later analyzed by the Finnish Marine Research Institute and SSS was measured. Figure 6.1 shows the campaign area, together with the SSS field obtained by the vessel and interpolated to the SSS retrieval grid (dictated by the HUT-2D alias-free FOV); white stars are for the vessel measurement locations. As can be noticed, some measurements had to be masked due to the presence of islands along the flights trajectory. These points are not included in the following analysis.

6.1.2 Methodology

As stated in the previous section, HUT-2D measurements consist of brightness temperature image snapshots of the radiometers alias-free field of view. The data processing approach adopted in this study involves salinity retrieval at the so-called Level 2, which consists of converting calibrated and geo-located brightness temperatures into

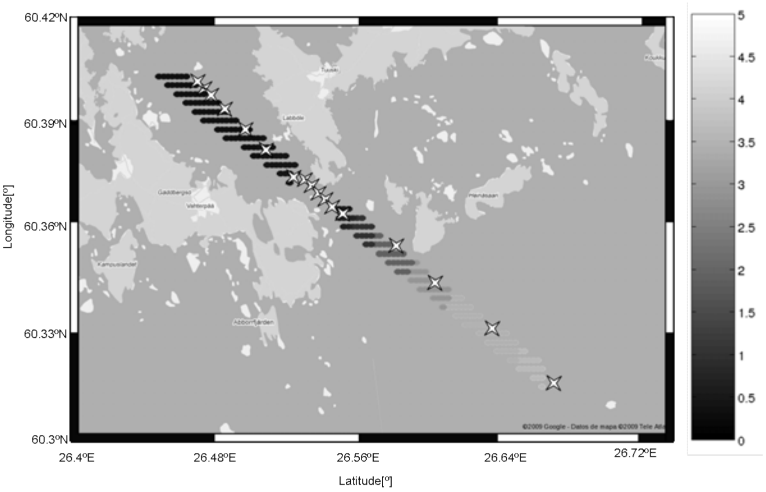

Figure 6.1: The field Campaign scenario, the *SSS* measured by the vessel and interpolated to the *SSS* retrieval grid (dictated by the HUT-2D alias-free FOV) is superimposed; white stars are for the vessel measurement locations

SSS maps. It can be described as a 3-step routine (as shown in Fig.6.2):

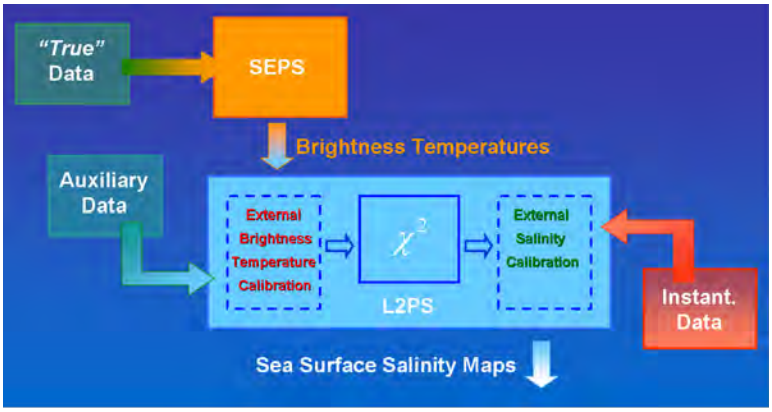

Figure 6.2: Flow chart of the retrieval procedure.

1. First, a data pre-processing step called the external brightness temperature calibration (*Camps et al.* (2005a); *Talone et al.* (2007b), *Talone et al.* (2009); section 4.2) is applied. In this study the Klein & Swift sea water dielectric constant model (*Klein and Swift*, 1977) and the WISE-derived wind speed (U_{10}) dependence model (*Camps et al.*, 2004b) are used. Both models are included in the official SMOS Level 2 Processor (*Zine et al.* (2008); section 3.6). Uniform and

specularly-reflected galactic noise (direct galactic noise equal to 3.7 K) and a linear approximation for the atmospheric contribution have been assumed (*Goodberlet and Miller*, 1997).

2. Secondly, the core of the processing is implemented: The *SSS* retrieval is performed as described in section 3.6 and using the following cost function:

$$\chi^2 = \sum_{n=1}^{N_{obs}} \left(\frac{\|F_n^{meas} - F_n^{model}\|^2}{\sigma_{F_n}^2} \right) + \frac{(SST - SST_{aux})^2}{\sigma_{SST}^2} + \frac{(U_{10} - U_{10aux})^2}{\sigma_{U_{10}}^2}, \quad (6.1)$$

where F_n^{meas}, F_n^{model} are the brightness temperatures measured by HUT-2D and obtained using the models, respectively, for the n^{th} observation. In particular F_n^{meas} can be defined as:

- $F_n = \left[\overline{T_Y}, \overline{T_X}\right]^T$, in the case of using the vertical (Y) and horizontal (X) polarizations of the measured brightness temperatures T in the antenna reference frame, or
- $F_n = \left[\overline{T_I}\right] = \left[\overline{T_Y} + \overline{T_X}\right] = \left[\overline{T_V} + \overline{T_H}\right]^T$, in the case of using the first Stokes parameter in brightness temperature (T_I), equal to the sum of the brightness temperatures in the vertical and horizontal polarizations (Y/X and V/H in the antenna and the Earth reference frames, respectively (*Randa et al.*, 2008)).

In both formulations, the line above letters T stands for vector, and each element of the vector corresponds to an incidence angle. The second and third terms in Eqn. 6.1 represent the constraints to the value of the auxiliary SST and 10-meter height wind speed as sea surface roughness descriptor, respectively. Assuming a diagonal error covariance matrix, these contributions are weighted in Eqn. 6.1 by the inverse of the variance of the misfit between the available auxiliary fields and the original ones, calculated as defined in Eqn. 6.2:

$$\sigma_p^2 = \frac{1}{N} \sum_{n=1}^{N} \left(p_{mis_i} - \left(\frac{1}{N} \sum_{n=1}^{N} p_{mis_i} \right) \right)^2, \quad (6.2)$$

where N is the total number of points taken into consideration, $p_{mis} = p_{aux} - p_{or}$, subscript *mis* stands for misfit, *aux* for auxiliary, *or* for original, and p for SST, or U_{10}. Actually, since the original geophysical values are not known, this definition cannot be applied and expected inaccuracies must be used instead (0.5 $^\circ C$ and 1.5 m/s for SST, and U_{10}, respectively)

3. Lastly, once the *SSS* is retrieved for each overpass, as described in section 6.3 the algorithm performs a calibration (External Sea Surface Salinity Calibration (*Talone et al.* (2007b); *Talone et al.* (2009)) to correct for the errors introduced by the forward emission models inaccuracies.This approach is based on the fact that once corrected for the biases in the brightness temperature (due to possible inaccuracies in the NIR brightness temperature estimation, imperfect correction of the foreign sources as the Sun, and errors in the image reconstruction, accounted for by the external brightness temperature calibration) the residual errors are small and the function to be minimized becomes more linear (*Sabia* (2008); *Sabia et al.* (2010)).

As can be seen from the above description, two external databases are needed to perform the Level 2 processing: the Auxiliary Data database which includes all the parameters involved in the minimization (*SST* and U_{10}, in this case), and the In-situ Data database embodying all the in situ measured *SSS* inside the zone of interest. For this study, the vessel measurements and ECMWF analysis results have been used for *SSS* and *SST*, and U_{10}, respectively. The measured *SSS* and *SST* ranged between 0.35 psu and 3.95 psu, and 19.4 $°C$ and 23.4 $°C$, respectively; and U_{10} was 2.76 m/s on the first day and 2.45 m/s on the second day.

6.1.3 *SSS* retrieval results

First, the brightness temperatures statistics are calculated to characterize the instrument performance in the cross-track direction, since this feature strongly affects the retrieval quality. Results are shown in Fig. 6.3 in terms of the cross-track difference between the measured brightness temperatures and the values calculated using the forward models described in Section 6.1.2 and the auxiliary data. The lines are the mean differences (solid for X-pol and dashed for Y-pol), while the error bars represent the standard deviation of these values. Systematic differences (2 - 3 K) can be noticed for the SD1 flight (Fig. 6.3a), in both X- and Y-pol, between the right and the left sides of the track, while the pattern is more uniform in the case of SD2 flight. This feature will have a negative impact on the retrieval performance of SD1.

Moving the attention from single measurements to the snapshot, the comparison between the mean values of the modeled brightness temperatures and the measured ones in the same snapshot (following the same procedure explained for the external brightness temperature calibration) is shown in Fig. 6.4 for a flight line from each flight series. In this figure, the error bars represent the standard deviation of this

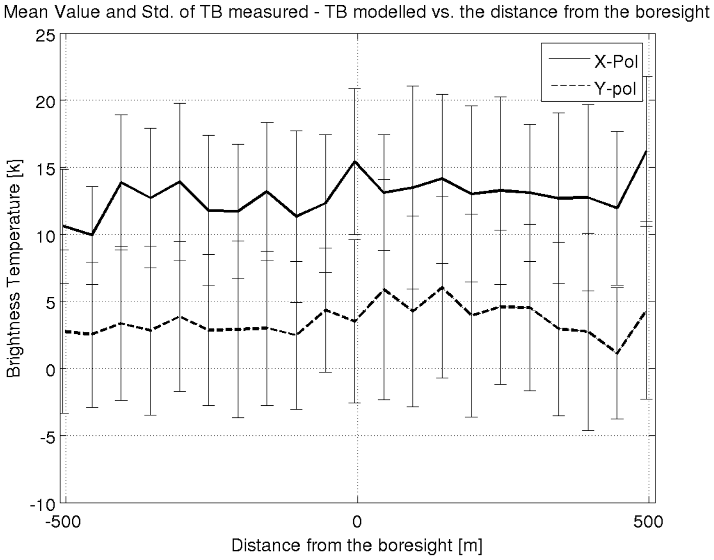

(a)

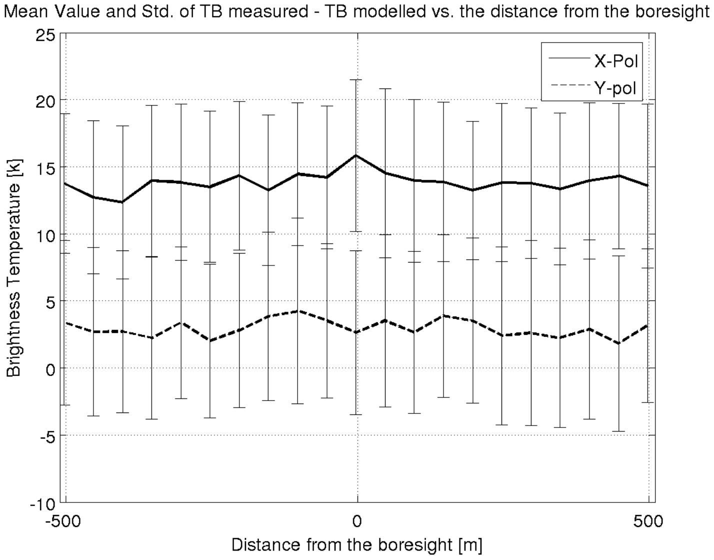

(b)

Figure 6.3: Cross-track pattern of the difference between measured and modeled Brightness Temperature for the (a) SD1 and (b) SD2 flights. The lines are the mean differences (solid for X-pol and dashed for Y-pol), while the error bars represent the standard deviation of these values.

difference and are centered on its mean value (the solid line), while the dashed one is the bias provided by Helsinki University of Technology (HUT) and calculated equating the nadir values at X- and Y-polarizations. For both Figs. 6.4a and 6.4b the X-pol is shown in the upper plot, while the Y-pol is in the bottom one. A mean difference of approximately 5 K can be observed at X-pol, while HUT and external brightness temperature calibration estimations almost agree for the Y-pol. According to the external brightness temperature calibration the resulting bias is on the order of 5 K for the Y-pol and 15 - 20 K for the X-pol.

Since the HUT-2D has a radiometric sensitivity of approximately 10 K (with the integration time used during this campaign, $\tau = 0.25s$), in order to have the closest SMOS-like results, two provisions must be made before processing the data:

1. To achieve a radiometric sensitivity comparable to the MIRAS output, all the flights of the same day (20 and 21 flight on August 13^{th} and 15^{th}, respectively) must be combined into a single overpass. In this way (considering all the successive overpasses to be independent and uncorrelated) the approximately 10 K sensitivity of the HUT-2D is changed to the 10 K$/\sqrt{20} = 2.23$ K and 10 K $/\sqrt{21} = 2.18$ K, very close to MIRAS' sensitivity at nadir for a single measurement.

2. In addition to that, all the measurements have been projected onto a regular 300-m cell grid and the incidence angles have been clustered in 2-, 4-, and 8-degree bins. More sophisticated averaging (like sliding-window weighted averaging) have not been taken into consideration to avoid the artefact of correlation introduced between adjacent brightness temperature measurements.

The effect of the incidence angle binning (in the 300-m cells) is shown in Figs. 6.5a and 6.5b in terms of the theoretical improvement considering that all the measurements are uncorrelated. The trend is similar for SD1 and SD2, as well as for X- and Y-pol, so only the X-pol for the SD2 flight is shown. The improvement by increasing the bin width is noticeable: approximately a factor of 0.75 going from 2° to 4° and 0.9 from 4° to 8°; The radiometric sensitivity is lower than 2 K for X- or Y-pol and 2.5 K for I in almost the whole FOV (between 5 and 25 degrees incidence angle). On the other hand, the drawback is an excessive quantization of the brightness temperatures with increasing bin-width, especially when retrieving with the two polarizations separately; as shown in Figs. 6.5c and 6.5d. In this case the quantization error is up to 5 K (c), while in the case of using TI the maximum is 1 K (d).

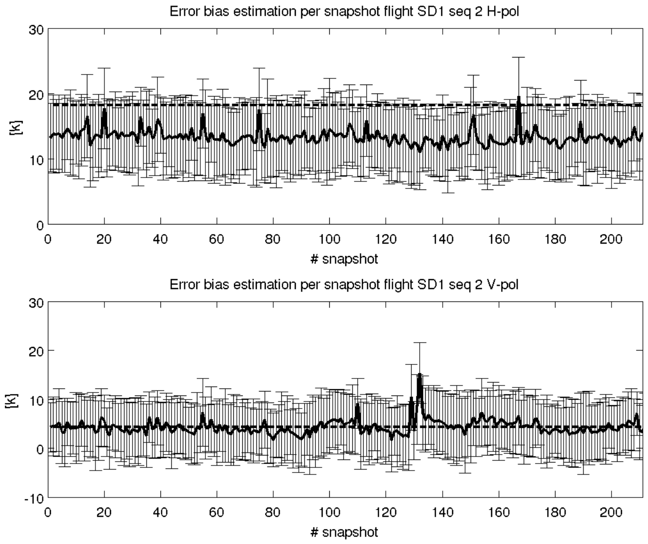

(a)

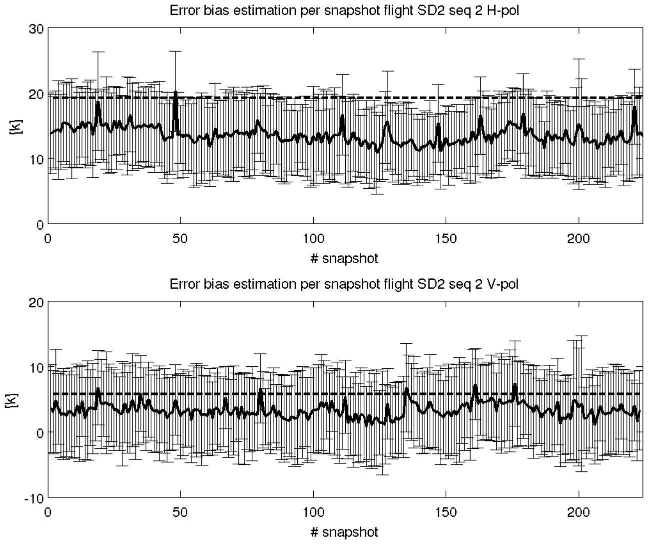

(b)

Figure 6.4: Mean value (solid line) and standard deviation (error bars) of the difference between measured and modeled Brightness Temperature, calculated for each snapshot of the (a) SD1 and (b) SD2 flights. The dashed superimposed line is the bias provided by Level 1.

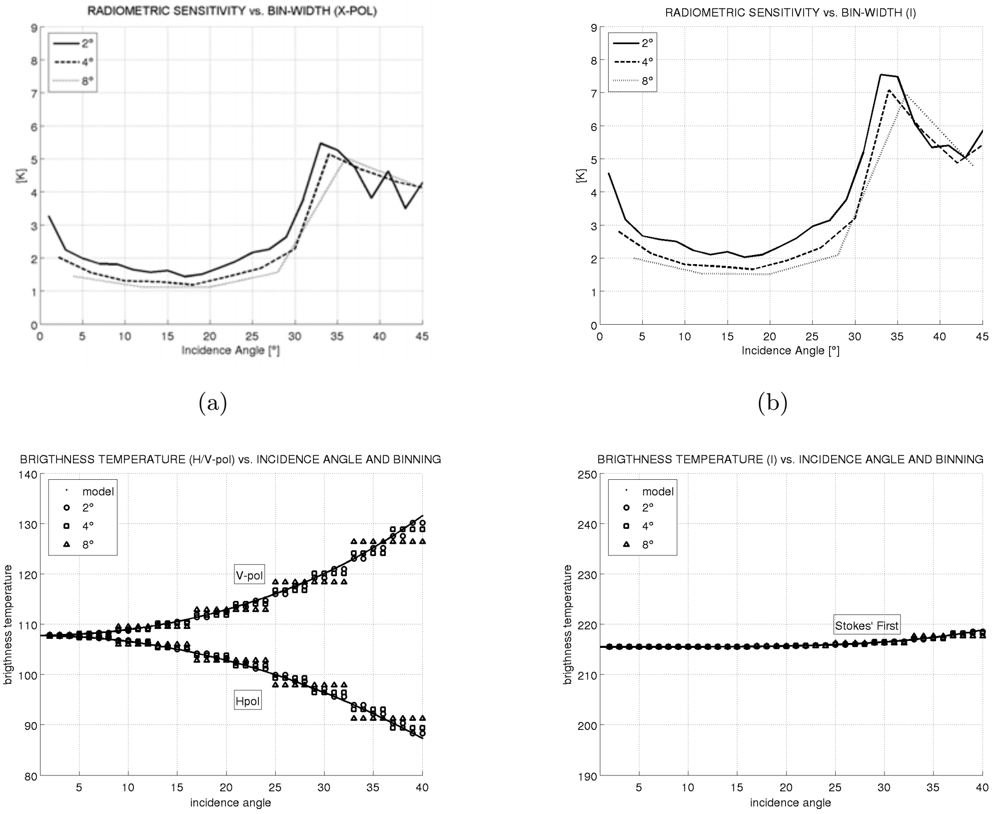

(a) (b)

(c) (d)

Figure 6.5: Effect of increasing the bin width on radiometric sensitivity for (a) the X-pol, and (b) the Stokes first parameter ($T_I = T_Y + T_X$). Accuracy of the forward model for (c) the H- and V-pol brightness temperatures, and (d) the Stokes first parameter (T_I).

The binned brightness temperatures are the inputs to the level 2 algorithm considering three different retrieval configurations:

A. No bias correction applied;

B. HUT-provided constant bias correction applied; or

C. external brightness temperature calibration applied.

Furthermore the effect of applying the External Sea Surface Salinity Calibration is assessed. Summarizing, since several combinations are possible permuting the various configurations, results have been summarized in tables, emphasizing three aspects:

1. the brightness temperature calibration effect;
2. the incidence angle binning effect; and
3. the external salinity calibration effect.

6.1.3.1 The brightness temperature calibration effect

Table 6.1 shows the mean error (μ), calculated as the average difference between the retrieved *SSS* and the measurements collected by the vessel, its standard deviation (σ), and the rms reported for both the SD1 and SD2 flights and for the case of retrieval using T_X and T_Y separately, or T_I, applying no bias correction (case A), the constant HUT-provided correction (case B), and the external brightness temperature calibration (case C). The bin-width used is 2 degrees.

The results for cases A and B can be interpreted based on the brightness temperature values. In case A the strong positive bias in the measurements is not corrected producing an underestimation of the retrieved salinity, which takes very low values (~ 0 psu) for the entire track, producing a misleading low mean value and standard deviation of the error (Figs. 6.6a and 6.6b). In case B the situation is the opposite; the bias HUT-provided bias is overestimated which entails an increase in the retrieved salinity (between 13 and 7 psu mean error, Fig. 6.6a). Bearing in mind this interpretation, case C is considered the best correction applied. Results are clearly better when using T_I, than when using $X-$ and $Y-$pol separately, since T_I is in fact less sensitive to errors in the incidence angle (*Camps et al.*, 2004b), and the best performance is obtained for the SD2 flight, as expected. Figure 6.6a shows the track-line for the flight SD2, with data retrieved using T_I. The solid line marks the *SSS* measured by the vessel while the dashed, dash-dot, and dotted lines stand for the HUT retrievals for cases A, B, and C,

Table 6.1: *SSS* retrieval results ((μ) mean error, (σ) standard deviation, and *rms*) with respect to the bias correction technique, retrieving with X- and Y- pol separately or using stokes I. case A: No Correction; case B: HUT Bias Correction; case C: Ext. Tb Calibration. 2-degree incidence angle binning is applied

[psu]		Case A			Case B			Case C		
		μ	σ	rms	μ	σ	rms	μ	σ	rms
SD1	$T_X - T_Y$	-2.04	1.56	**2.57**	13.06	4.91	**13.95**	6.79	4.16	**7.96**
	T_I	-2.04	1.55	**2.56**	7.14	4.38	**8.38**	2.09	4.01	**4.52**
SD2	$T_X - T_Y$	-1.31	1.83	**2.25**	10.93	8.65	**13.94**	5.12	5.60	**7.59**
	T_I	-1.38	1.38	**1.95**	7.36	5.43	**9.15**	1.40	2.93	**3.25**

respectively. The corresponding 1-σ error bars are superimposed to each line. A zoom of Fig. 6.6a in the range 0 - 4 psu is presented in Fig. 6.6b. Finally, the pdf of the *SSS* error for the case C of the same flight is represented in Fig. 6.6c; the superimposed dashed line representing the Gaussian p.d.f. with the same mean and standard deviation values. Particular attention must been paid to the departure of the retrieval statistics from the Gaussian pdf, which can reduce the validity of the confidence limits generally defined considering Gaussian processes.

6.1.3.2 Incidence angle binning effect

Table 6.2 shows the retrieval results as in Table 6.1, but focusing on the improvement of the performance with respect to the change in bin-width. Case C configuration has been selected. As in paragraph 6.1.3.1, flight SD2 gives better results than SD1, but within the same flight the effect of increasing the angular bin size does not seem to affect the retrieval results significantly. Just a slight improvement (a tenth of psu) can be noticed using T_X and T_Y separately when decreasing the bin-width. Considering Tables 6.1 and 6.2, it can be concluded that the best retrieval is obtained with configuration C and using a bin-width of 2° for both T_I and $T_X - T_Y$.

6.1.3.3 The external salinity calibration effect

In Section 6.1.3.2 the optimum retrieval configuration was determined (using the first Stokes parameter T_I, with a 2-degree angular binning). The External Salinity Calibration technique, as described in section 6.3, was applied. Results are summarized

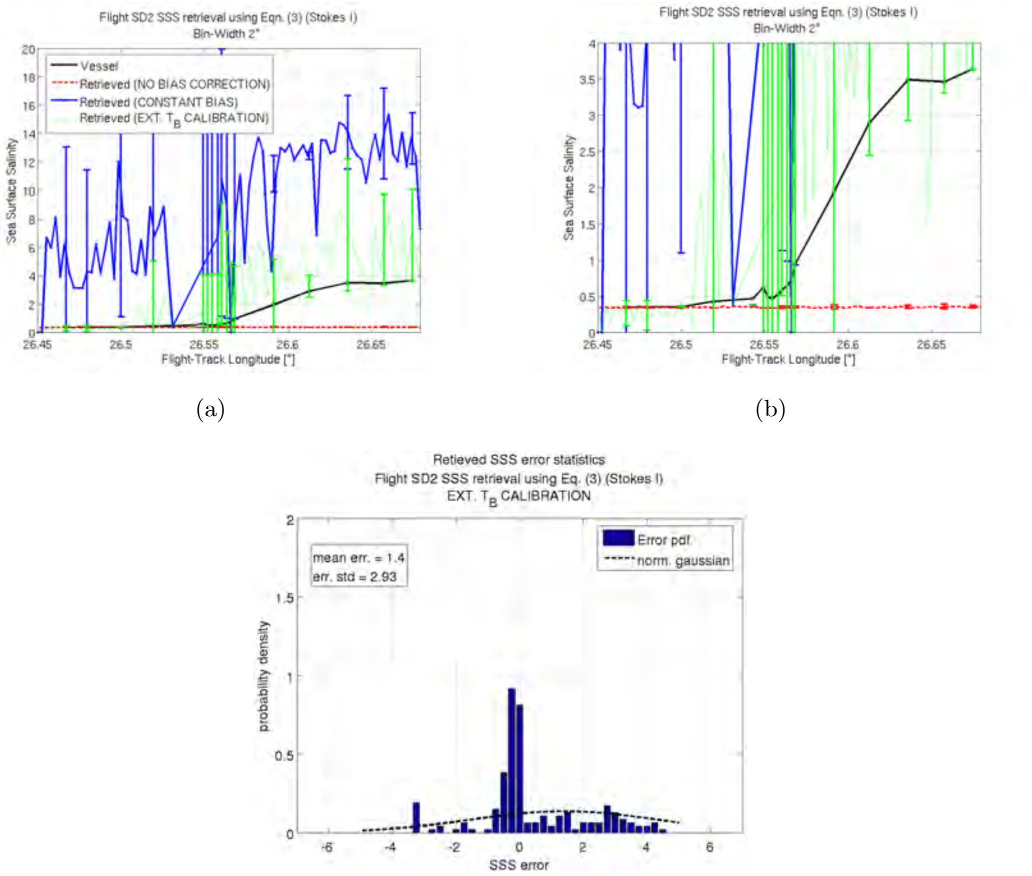

(a) (b)

(c)

Figure 6.6: (a) Track-line for the SD2 flight using a 2° bin-width and three different retrieval configurations and (b) its zoom between 0 and 4 psu. The solid line stands for the ground-truth values, while the dashed, dash-dot, and dotted lines for the retrieved ones in case of choosing the configuration A, B, and C, respectively. Error bars are superimposed to each line. (c) Normalized pdf of the retrieval error, the superimposed dashed line is the normal distribution pdf with the same mean value and standard deviation.

Table 6.2: *SSS* retrieval results ((μ) mean error, (σ) standard deviation, and *rms*) with respect to the bin width, retrieving with X- and Y- pol separately or using stokes I. Ext. Tb Calibration is applied

[psu]		2°			4°			8°		
		μ	σ	$\boldsymbol{rms}$	μ	σ	$\boldsymbol{rms}$	μ	σ	$\boldsymbol{rms}$
SD1	$T_X - T_Y$	6.79	4.16	**7.96**	6.86	4.13	**8.01**	7.20	4.01	**8.24**
	T_I	2.09	4.01	**4.52**	2.14	4.03	**4.56**	2.11	4.00	**4.52**
SD2	$T_X - T_Y$	5.12	5.60	**7.59**	5.22	5.62	**7.67**	5.37	5.69	**7.82**
	T_I	1.40	2.93	**3.25**	1.46	3.15	**3.47**	1.35	3.04	**3.33**

Table 6.3: Effect of the External Salinity Calibration ((μ) mean error, (σ) standard deviation, and *rms*) retrieving with X- and Y- pol separately or using stokes I. 2-degree incidence angle binning and Ext. Tb Calibration is applied

[psu]	*SD1*			*SD2*		
	μ	σ	$\boldsymbol{rms}$	μ	σ	$\boldsymbol{rms}$
$T_X - T_Y$	0.66	1.77	**1.89**	0.03	1.37	**1.37**
T_I	2.30	4.20	**4.79**	0.78	2.31	**2.44**

in Table 6.3. Comparing Tables 6.3 and 6.2, a clear improvement can be observed in all the cases (except SD1 flight retrieval with T_I). Very good results are obtained for the SD2 flight considering the instrument performance: rms error of 1.37 and 2.44 psu retrieving with $X - /Y-$ pol separately and T_I, respectively. This occurs despite the low sensitivity of the brightness temperatures at this range of *SSS* and the inaccuracies of the models near the coast, for both the wind speed and the effect of sea surface roughness on the total brightness temperature. Similarly to Fig. 6.6, Fig. 6.7 shows the (a) track-line and (b) histogram of the error for this case.

Finally, in addition to the aforementioned techniques (external brightness temperature calibration, incidence angle binning, and external sea surface salinity calibration), the spatial averaging of the retrieved *SSS* has been considered to mimic the SMOS spatial averaging of the retrieved salinity despite the different alias-free field of views. The track-line has been divided into eight cells of approximately 1.5 km side, as shown

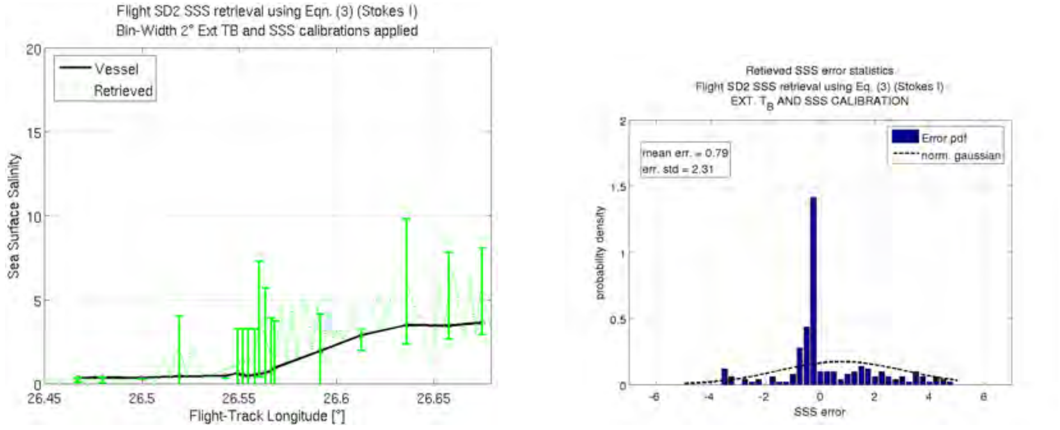

(a) (b)

Figure 6.7: (a) Track-line for the SD2 flight using a 2 bin-width and both external brightness temperature calibration and External Salinity Calibration. The solid line stands for the ground-truth values and the dotted line for the retrieved values. Error bars for the retrieved *SSS*, calculated in the vessel measurements locations are als shown. (b) Normalized pdf of the retrieval error, the dashed line superimposed is the normal distribution pdf with the same mean value and standard deviation.

in Fig. 6.8a, and both the vessel-measured and the retrieved salinities have been averaged in each of them. Results are shown in Fig. 6.8b. As can be observed, the salinity gradient is successfully retrieved, with errors on the order of 1 psu, except for a point in the middle of the transition.

6.1.4 Conclusions

Two series of flights were carried out over the Gulf of Finland during the summer of 2007 to test *SSS* retrieval algorithms using 2D microwave radiometry. The synthetic aperture HUT-2D radiometer (*Rautiainen et al.* (2007) and *Rautiainen et al.* (2008)) was used to perform *SSS* measurements, while in situ validation measurements were collected by a vessel. HUT-2D data have been processed and the results analyzed in order to test the techniques developed in past years (based on simulated brightness temperatures) to improve the *SSS* retrieval. Actually, both the external brightness temperature calibration and the External Salinity Calibration were tested in a previous work by *Talone et al.* (2009) using SMOS-like simulated data (with SEPS). Using only climatology for the external brightness temperature calibration and the ARGO buoy array for the external sea surface salinity calibration results in a good improvement

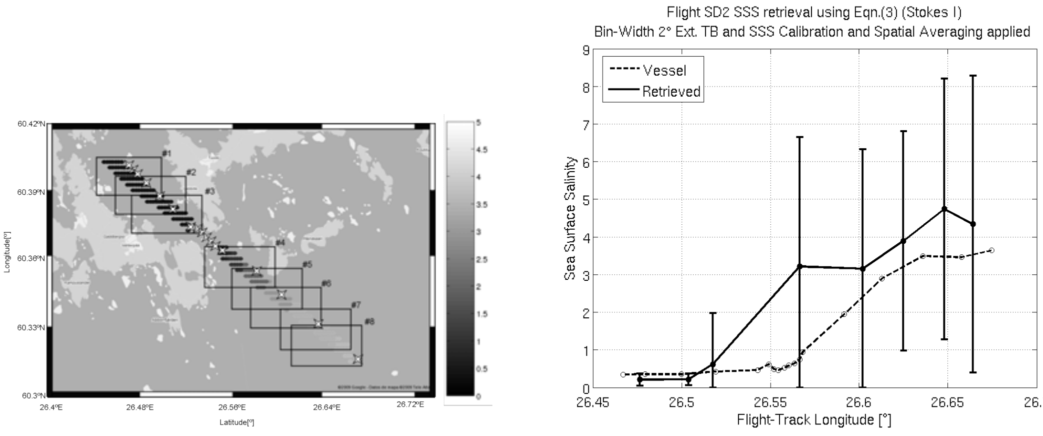

(a)

(b)

Figure 6.8: Eight cells considered in the study superimposed onto the HUT sample location; the *SSS* measured by the vessel and interpolated to the *SSS* retrieval grid (dictated by the HUT-2D alias-free FOV) is shown in the figure; white stars are for the vessel measurement locations. (b) Retrieved *SSS* after averaging (solid line) vs. the *SSS* measured by the vessel (dashed line) for the SD2 flight series.

of the performance of the *SSS* retrieval algorithm. In that case, the same auxiliary data used for the level 2 retrieval were used for the external brightness temperature calibration. However, for the external sea surface salinity calibration a sliding window of one month centred in the day of measurement was applied to select the ARGO data. The main conclusion of this study is an experimental confirmation of the validity of both the external brightness temperature calibration and the external sea surface salinity calibration. Applying both techniques, *SSS* has been retrieved with a rms error of approximately 2 psu, which is a very good result considering the instrument characteristics ($\Delta T = 10\ K$) and the geophysical conditions (coastal region with cold water and very low *SSS*). Moreover, averaging the results in larger cells (approximately 1.5 km side), the error decreases down to 1 psu, allowing to satisfactorily track the *SSS* gradient.

6.2 The SMOS case

The last of the studies with experimental data of this chapter is the processing of real SMOS data. As said, SMOS was launched on November 2, 2009; during the first months after the launch SMOS ESLs (among them UPC, ICM, and the SMOS-BEC) have been in charge of monitoring, characterizing, and improving SMOS performance, this period is the so-called “Commissioning Phase”. Processed data have been acquired from July 10^{th} to 19^{th}, 2010 in Full-Polarisation Mode. To retrieve *SSS* the official SMOS Level 2 OS Processor (*Zine et al.*, 2008) has been used and results have been compared to the World Ocean Atlas 2005 annual climatology (WOA05) and ARGO data. Since modifications are still daily introduced to the SMOS retrieval procedure, the preliminary nature of these tests must be remarked.

6.2.1 Methodology

Ten days of real L1c data from SMOS have been processed starting from July 10^{th} until July 19^{th}, 2010. To reduce the computational burden, SMOS L1c data have been scaled down from ISEA4h9 (*Snyder*, 1992) to the ISEA4h8 (twice coarser) grid. According to Chapter 5, the correlation between neighbouring gridpoints permits to assume consistency between the results obtained with ISEA 4h8 and ISEA 4h9. Nevertheless simulations required the use of 4 nodes of a computational server (8 x 2.26 GHz CPUs with 32 Gb RAM each) during 20 days.

Sea surface salinity have then been retrieved using the official SMOS Level 2 OS Processor (*Zine et al.*, 2008) according to three different cases:

A: Nominal Product without any calibration.

B: Applying the external brightness temperature calibration, as described in Chapter 4.

C: Applying the so-called ocean target transformation (*Meirold-Mautner et al.*, 2009), which will be described in section 6.3.1.

Moreover, since the official SMOS Level 2 OS Processor carries out three retrievals for each run, there is room for three different configurations namely:

SSS1: Model 2 (*Irisov*, 1997) and (*Johnson and Zhang*, 1999), in the “Dual from Full-Pol” mode, i.e. retrieving using T_X and T_Y separately, T_3 and T_4 are neglected.

SSS2: Model 2 (*Irisov*, 1997) and (*Johnson and Zhang*, 1999), in the “Stokes’ first from Full-Pol” mode, i.e. retrieving using Stokes’ first parameter in brightness temperatures: $I = T_X + T_Y$, T_3 and T_4 are neglected.

SSS3: Model 3, configuration 16 (*Gabarró et al.*, 2004), in the “Stokes’ first from Full-Pol” mode.

Model 2 has been chosen as the default mode because it is not expected to be significantly modified in future, as opposed to Model 3 which is now optimized for retrieving in the Mediterranean Sea and will be tuned for its global application using SMOS' measurements. The choice of processing 10 days, using Stokes' first parameter as default, and neglecting T_3 and T_4 has been driven, instead, by the intention of permit some comparisons with the previous simulations described in Chapter 4.

As opposed to Chapter 4, in this case real data have been processed, so a proper "retrieval error" cannot be calculated since real values are not available. Performances are thus estimated at Level 3. Level 2 retrieved *SSS* have been averaged in cells of 2×2 degrees according to Eqn. 6.3:

$$SSS_{cell} = \frac{\sum_i \left(SSS_i \cdot N_{obs_i}\right)}{\sum_i N_{obs_i}}, \tag{6.3}$$

where subscript i represents thei^{th} cell.

To allow the comparison, ARGO data have been spatially averaged in 2×2-degree cells. Moreover, to collect enough measurements the temporal window between June 10^{th} and August 19^{th} has been considered.

The quality assessment has been carried out according to two tests:

- The results of the retrievals, after performing a weighted average as described in Eqn. 6.3, are compared to climatological estimates and to the averaged ARGO.

- To someway assses the performance of the retrievals the weighted precision has been calculated for each of the cells, according to Eqn. 6.4:

  $$p_{cell} = \sqrt{\frac{\sum_i \left(\left(SSS_i - \overline{SSS_i}\right)^2 \cdot N_{obs_i}\right)}{\sum_i N_{obs_i}}}, \tag{6.4}$$

  as for Eqn. 6.3, subscript i represents the i^{th} cell.

Before computing the weighted average in Eqn. 6.3, level 2 retrieved *SSS* have been filtered according to two of the level 2 flags:

- *Fg_marq:* Indicating that the Levember-Marquardt optimization algorithm did not converge.

- *Fg_max_iter:* Indicating that no convergence has been reached before a certain number of iterations, in this case 20.

In addition to that, when computing statistics only the points farther away more than 200 km from the coast have been considered, while in figures all the points are shown.

Finally, results have been analysed using all the overpasses to construct the level 3, using only ascending overpasses, and using only descending overpasses. All the tests are shown for the case of using all the overpasses to easy the comparison with chapter 4, anyway, the cases of using all the overpasses, only the ascending ones, or only the descending ones will be also compared.

Climatological sea surface salinity and temperature, as well as the average wind speed from ASCAT are shown in Fig. 6.9a, b, and c, respectively. Sea surface salinities and temperatures for ARGO are instead shown in Fig. 6.10: all the data between July 10^{th} and August 19^{th} have been averaged in 2×2 degrees to be compared with SMOS level 3 SSS.

The total number of measurements acquired during the observed period is shown in Fig. 6.11.

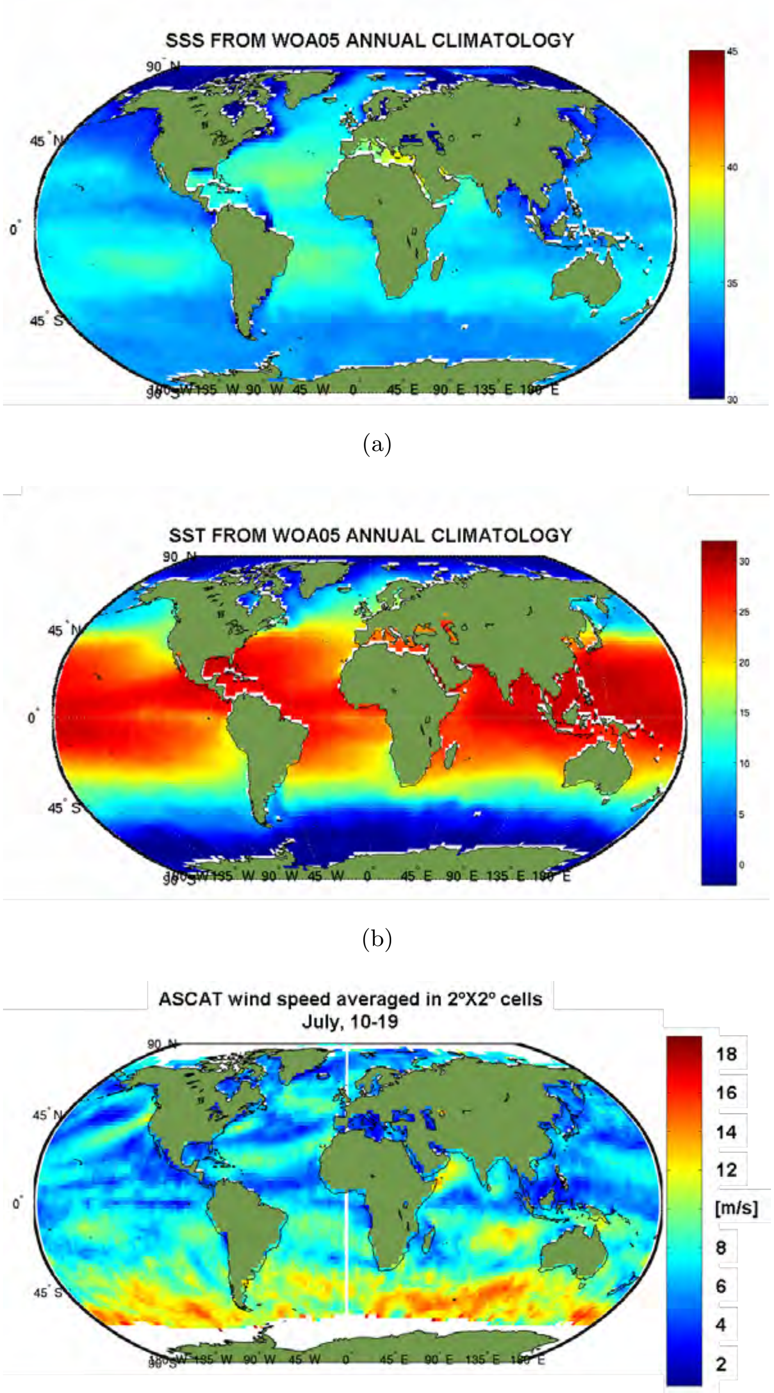

(a)

(b)

(c)

Figure 6.9: Climatologic (a) sea surface salinity, (b) temperature, and (c) average wind speed from ASCAT

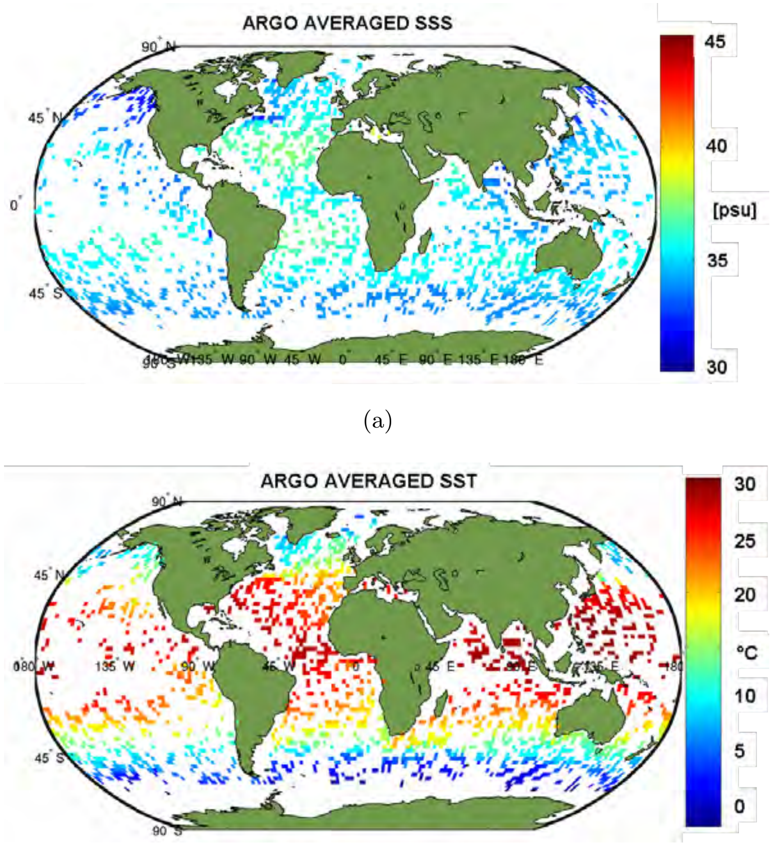

(a)

(b)

Figure 6.10: ARGO averaged (a) sea surface salinity, and (b) temperature

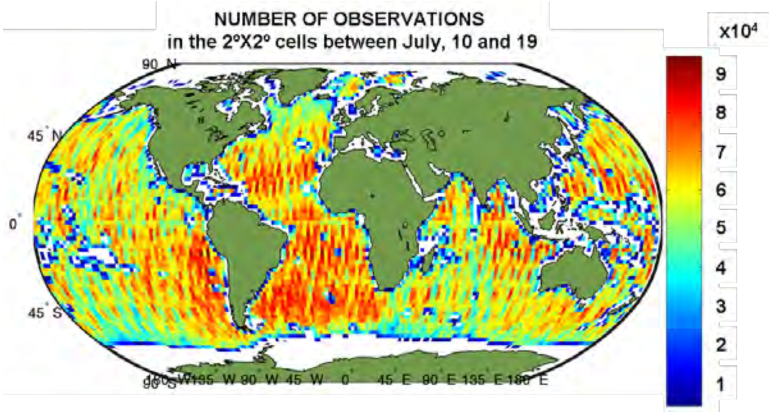

Figure 6.11: Total number of measurements acquired during the observed period

According to *Camps et al.* (2005a) errors in the reconstructed SMOS brightness temperature should be expected due to inaccuracies in the antenna pattern estimation, the image reconstruction algorithm, and the NIR brightness temperature measurements. This bias is scene-dependent (*Camps et al.*, 2008a), varying from snapshot to snapshot and polarization. As a possible mitigation of that phenomenon, the external brightness temperature calibration was proposed in the *Camps et al.* (2005a). For each snapshot and for all the points in the Extended Alias-Free FOV, pseudo-brightness temperatures are calculated using auxiliary data and the same forward models used in the retrieval algorithms. The calculated pseudo-brightness temperatures are subtracted from the measured ones, and the mean of this difference is considered as the mean bias introduced by the instrument errors. The "corrected brightness temperature" is then defined as the measured brightness temperature minus the mean bias. The algorithm can be summarized by the expressions as follows, where $\langle\rangle$ stands for mean value over the pixels in the Extentended Alias-Free Field of View:

$$\Delta T_B = \langle T_B^{meas}\left(SSS_{or}, SST_{or}, U_{10_{or}}, \theta\right) - T_B^{mod}\left(SSS_{aux}, SST_{aux}, U_{10_{aux}}, \theta\right)\rangle, \quad (6.5)$$

$$T_B^{corrected} = T_B^{meas} - \Delta T_B. \quad (6.6)$$

In Eqns. 6.5 and 6.6 the subscripts *"or"* and *"aux"* stand for original (true value to be retrieved) and auxiliary, respectively, while superscripts *"meas"* for measured, and *"mod"* for modelled.

6.3 The external sea surface salinity calibration

As explained in section 3.6 the retrieval procedure within the SMOS mission is iterative; In this context one of most significant contributions to the success of the retrieval is given by the reliability and accuracy of the forward models. At present, the scientific community has not still completely agreed about the error that the inaccuracies in the current forward models, both for sea-water dielectric constant and sea surface roughness contribution to the brightness temperature are introducing in the retrieved *SSS*. Meanwhile this issue is not entirely assessed, in the official SMOS-OS level 2 Operational Processor the Klein & Swift model (*Klein and Swift*, 1977) is used to calculate the dielectric constant of seawater and three different models are used for sea surface roughness: the two-scale model (*Yueh* (1997) and *Dinnat et al.* (2003)), the Small Slope Approximation model (*Irisov* (1997), *Johnson and Zhang* (1999), and

Reul et al. (2001)), and the semi-empirical model by Gabarró et al. (*Gabarró et al.*, 2004). As mentioned in chapter 2, none of these models has proven so far better than the others; The external sea surface calibration aims at correcting for the uncertainty introduced by the forward model inaccuracies and implements a technique similar to the one used in rain radar calibration (*Seo and Breidenbach*, 2002) using as ancillary in-situ database the ARGO array of buoys. The algorithm consists of calculating a so-called *Calibration Factor* (CF) as the ratio between the auxiliary in-situ *SSS* mean value and the retrieved *SSS* one. The algorithm is simply implemented through the following expressions:

$$CF = \frac{\langle SSS_{in\_situ} \rangle}{\langle SSS_{ret} \rangle} \tag{6.7}$$

$$SSS_{corr} = CF \cdot SSS_{ret} \tag{6.8}$$

When computing the CF, a filtering based on the number of observations is applied: the pixels observed less than 40 times are not taken into account because of the large instrumental errors (Fig. 4.1). Figure 4.1 shows the error in the retrieved *SSS* in function of the number of observations, more details on this figure are given in paragraph 4.6. The corrected retrieved salinity is then given by the product between CF and the retrieved salinity.

6.3.1 The Ocean Target Transformation

The ocean target transformation (OTT) was firstly introduced in *Meirold-Mautner et al.* (2009), then implemented and tested by Dr. Tenerelli. It is calculated by averaging the departure of the SMOS brightness temperature measurements from simulated brightness temperatures using ocean forward models. The averaging is performed in the antenna reference domain. An accurate filtering of the snapshots must be applied to discard land and/or Radio Frequency Interferences (RFI) contaminations. Ascending and descending passes must be considered separately. Finally, many orbits are used to increase the robustness of the estimation. An example of OTT for the X- and Y-polarizations is shown in Fig. 6.12a and b, respectively. This OTT has been obtained processing 89 ascending passes (1 week of data).

Very well defined structures are present associated to the various aliases, the border of the extended alias-free FOV is clear, as well as the transition extended alias-free/alias-free FOV; inhomogeneities up to 10 K are detected. Similarly to the case of the external brightness temperature calibration, the corrected brightness temperatures

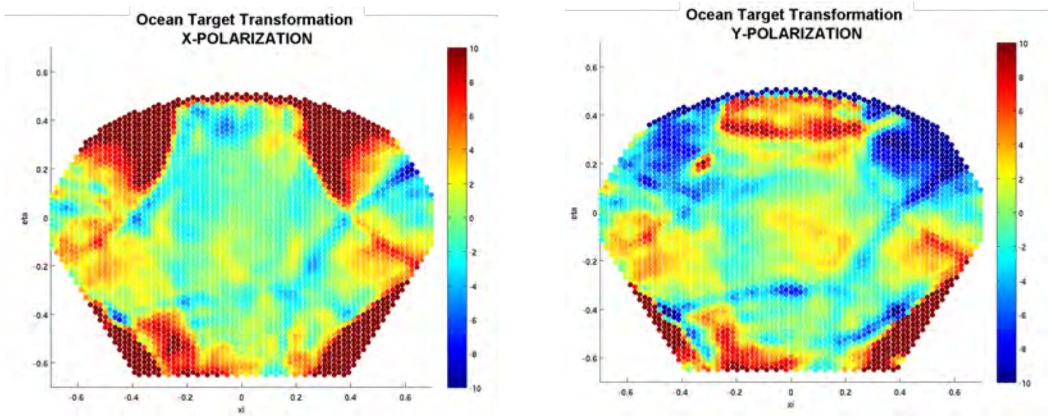

(a) (b)

Figure 6.12: An example of OTT for the (a) X- and (b) Y-polarizations

used in the retrieval are the measured ones minus the estimated bias, which is now constant in time, but spatially-dependent.

6.3.2 Results

Results are organized and presented following four research lines:

- Firstly, the bias mitigation techniques are compared: cases A, B, and C are analyzed and compared with climatology, in this case only the first configuration is shown (Model 2 in the "Dual from Full-Polarisation" mode),
- then the comparison T_X/T_Y *vs. Stokes' first* using Model 2 is done,
- the issue *Model 3(16) vs. Model 2* is assessed retrieving using Stokes' first parameter in brightness temperature, and finally
- the comparison between a level 3 product synthesized using all the overpasses, only the ascending ones, or only the descending ones is presented.

6.3.2.1 Bias mitigation techniques

The results of the spatio-temporal averaging and the comparison between these and the WOA climatology for the three configurations are shown in Figs. 6.13 and Fig. 6.14, being a, b, and c the case of applying no bias correction, the external brightness temperature calibration, and the ocean target transformation, respectively.

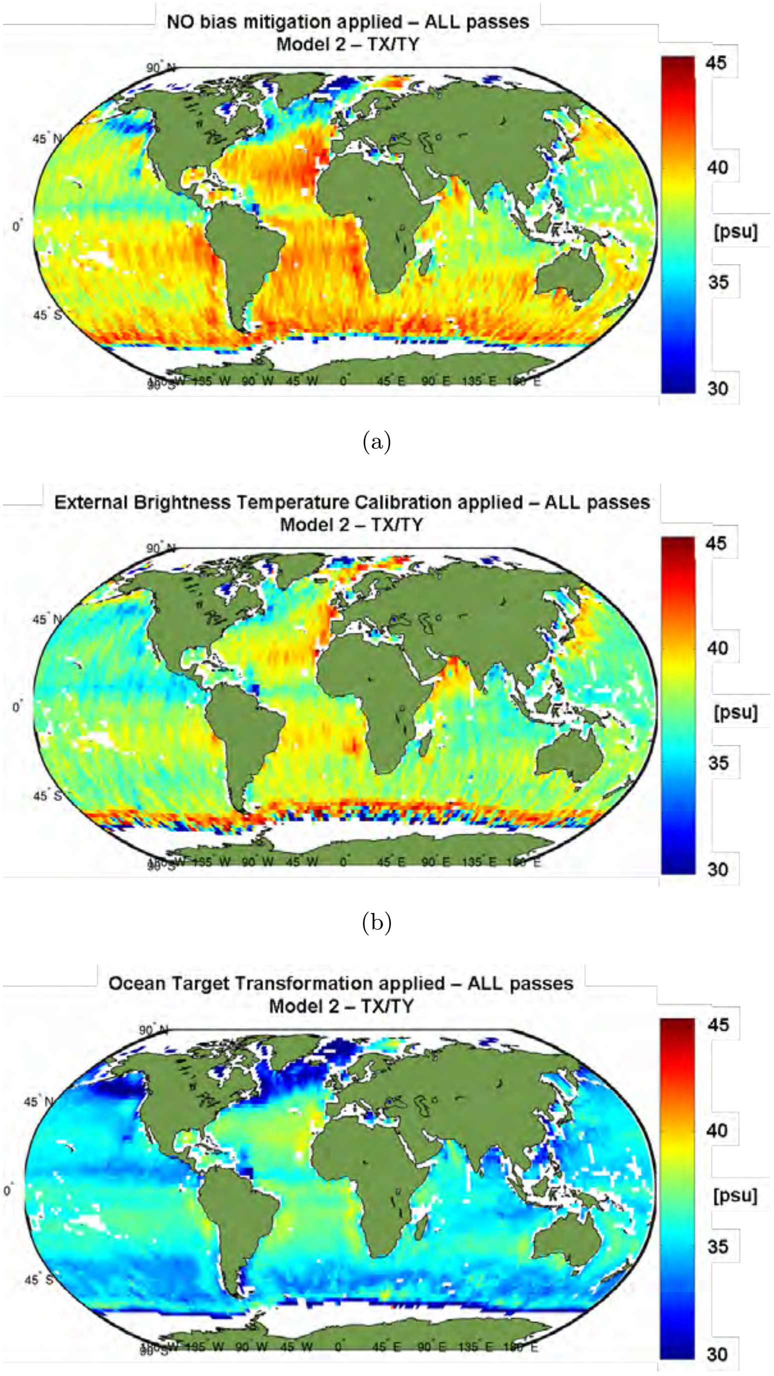

(a)

(b)

(c)

Figure 6.13: Level 3 ten-day average map for (a) the nominal case, (b) the case of applying the external brightness temperature calibration, and (c) of applying the ocean target transformation - MODEL 2 DUAL FROM FULL-POL

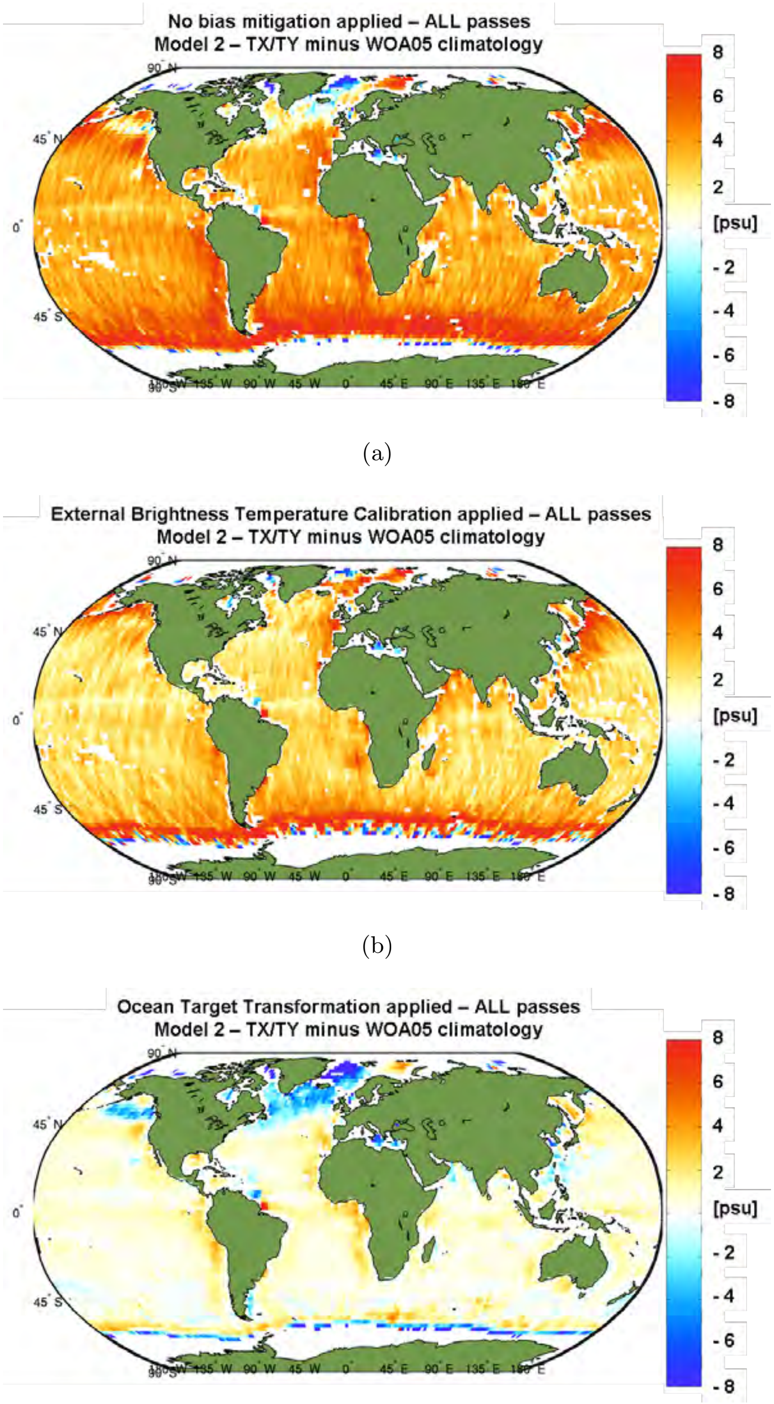

(a)

(b)

(c)

Figure 6.14: Level 3 ten-day map minus WOA05 climatology for (a) the nominal case, (b) applying the external brightness temperature calibration, and (c) applying the ocean target transformation - MODEL 2 DUAL FROM FULL-POL

As can be noticed, comparing Fig. 6.13 with the climatology presented in Fig. 6.9, in all the three cases SMOS measurements reproduce well the main structures of the *SSS* field. A clear example is the *SSS* anomaly generated by the Amazon plume, clearly visible in the three retrievals. Case C gives the best performance, while both case A and B are affected by a positive bias.

The very fresh waters in the Northern emisphere are due to Radio Frequency Interference (RFI), namely several horizon scanning radars have been detected around the North Pole strongly saturating the measured brightness temperatures for the higher icidence angles, and various radars are also present in China and affect the zone of Malaysia, Vietnam and the South China Sea. Strong artifacted positive "shadows" are present near to the coasts of South America, Africa, and Australia, especially in configuration A and C. This is the so-called land-sea transition problem, the phenomenon is still on study and could be due to bugs in the processing or to the underestimation of the contribution of the synthetic antenna secondary lobes to the measured brightness temperature. The effect is much less pronounced in the case of using the external brightness temperature calibration, actually if the strong positive bias affecting the retrieval of configuration B is subtracted, the result is very homogeneous as shown in Fig. 6.15.

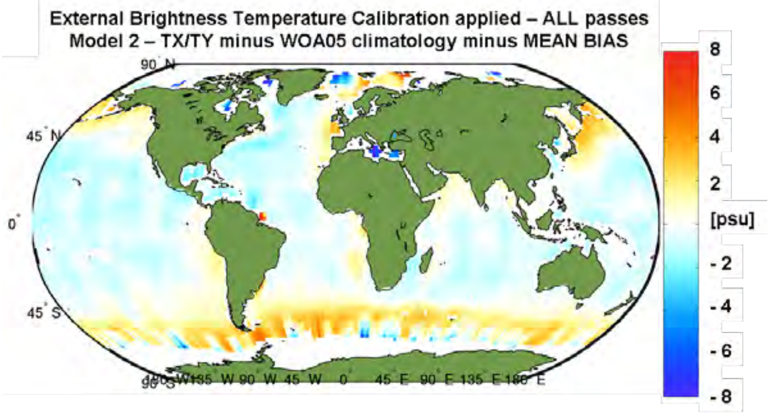

Figure 6.15: Level 3 ten-day map minus WOA05 climatology MINUS MEAN BIAS for the case of applying the external brightness temperature calibration - MODEL 2 DUAL FROM FULL-POL

The precision of the retrieval, calculated as expressed in Eqn. 6.4, is shown in Fig. 6.16, since this is very similar for all the configurations, only the case of applying the ocean target transformation is presented. The black line superimposed indicates the 2.5 psu level, considered as a 1-bit indicator of bad/good retrieval. As can be observed the zone affected by the land-sea transition problem are filtered out by this selection.

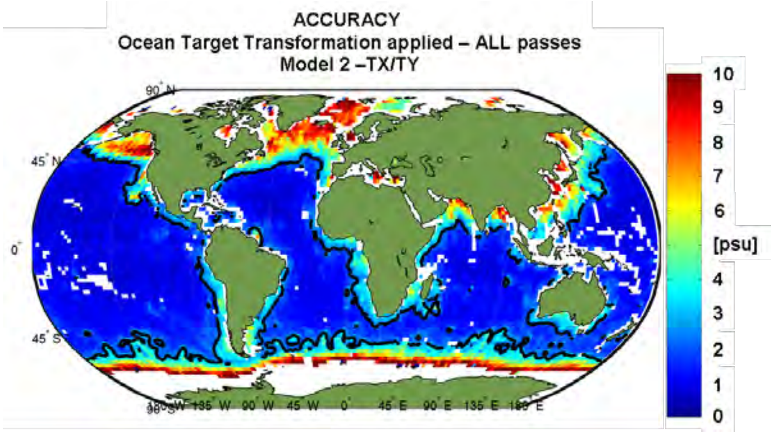

Figure 6.16: Precision of the level 3 retrieved *SSS* for the case of applying ocean target transformation. The black line indicates 2.5 psu - MODEL 2 DUAL FROM FULL-POL

The normalized histograms for the three configurations are shown in Figs. 6.17 and summarized in Table 6.4, where the comparison with ARGO data is also reported. In all the three figures the blue bars are calculated considering all the retrieved gridpoints, while the red ones are calculated using only gridpoint retrieved with a precision lower than 2.5 psu. Labels a, b, and c are the nominal case, the case of applying the external brightness temperature calibration, and of applying the ocean target transformation, respectively. Finally, in Table 6.4 μ stands for the mean value and σ is the standard deviation.

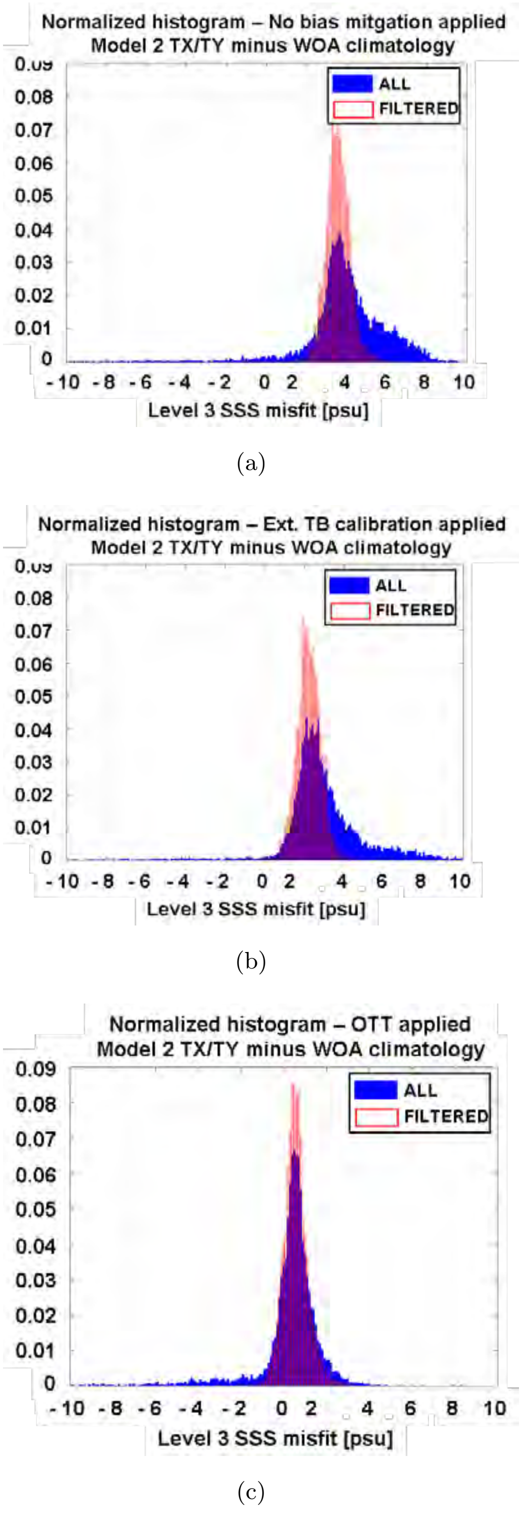

(a)

(b)

(c)

Figure 6.17: Normalized histograms of the misfit between the Level 3 ten-day retrieved *SSS* and WOA05 climatology for (a) the nominal case, (b) applying the external brightness temperature calibration, and (c) applying the ocean target transformation - MODEL 2 DUAL FROM FULL-POL

Table 6.4: Retrieval performance at level 3, Bias mitigation techniques

[psu]	$\mu(SSS_{mis})$	$\sigma(SSS_{mis})$	$rms(SSS_{mis})$
VS. WOA CLIMATOLOGY			
		All points	
case A	3.9591	2.6742	4.7776
case B	2.9600	2.3886	3.8036
case C	0.2260	2.2565	2.2678
		Filtered points	
case A	3.3468	3.7604	5.8288
case B	2.1981	1.7300	2.7972
case C	0.5559	1.4457	1.5489
VS. AVERAGED ARGO			
		All points	
case A	4.1488	1.8571	4.5455
case B	3.1541	1.7764	3.6199
case C	0.2958	1.4391	1.4692
		Filtered points	
case A	3.5769	0.6327	3.6327
case B	2.2214	0.5801	2.2959
case C	0.5278	0.5805	0.7846

As can be noticed by analyzing Table 6.4, comparisons with WOA climatology and ARGO averaged data give consistent results: the mean misfit decreases when using the external brightness temperature calibration (14% and 20% using all the points, 52% and 37% using only the filtered points, respectively), and even more using the ocean target transformation 52% and 68% using all the points, 73% and 78% using only the filtered points, respectively), standard deviation takes very similar values in the three configuration, except for the configuration B analyzing only the filtered points; filtering out points with a precision higher than 2.5 psu strongly improves the performance reducing the misfit rms and leading to the best case (case C) of 0.78-1.54 psu rms vs. ARGO and WOA climatology.

6.3.2.2 $\mathbf{T_X/T_Y}$ vs. Stokes' first

Based on the results of the previous section, the comparison between T_X/T_Y and Stokes' first parameter in brightness temperature and between Model 2 and Model 3 are commented only for the best case: case C, applying the ocean target transformation. Some of the figures and numbers presented in this and the following section have already been shown, anyway for sake of convenience and to easy the comparison, they are repeated.

Performance is assessed graphically through the analysis of the difference between the case of retrieving using Stokes' first parameter in brightness temperature and T_X/T_Y separately (Fig. 6.18), and numerically through the normalized histograms shown in Fig. 6.19 and of Table 6.5. In Figs. 6.19 a and b are the case of retrieving using T_X/T_Y separately and using Stokes' first parameter in brightness temperature, respectively, being the blue bars relative to all the retrieved gridpoints and the red ones only to the gridpoints with a precision lower than 2.5 psu. In Table 6.5 μ stands for the mean value and σ for the standard deviation.

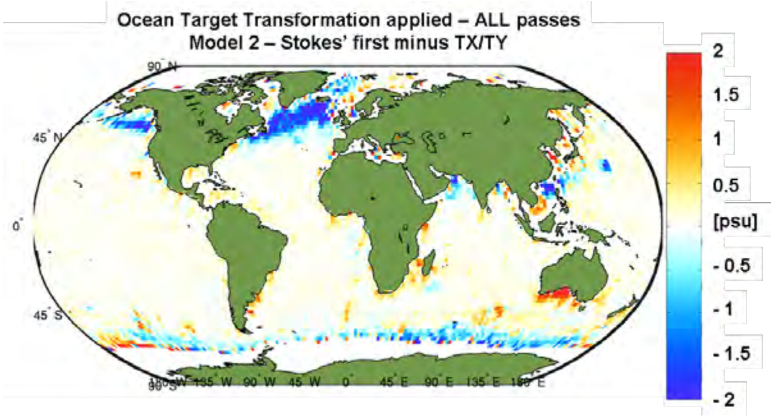

Figure 6.18: Level 3 retrieved *SSS* using Stokes' first minus using T_X/T_Y

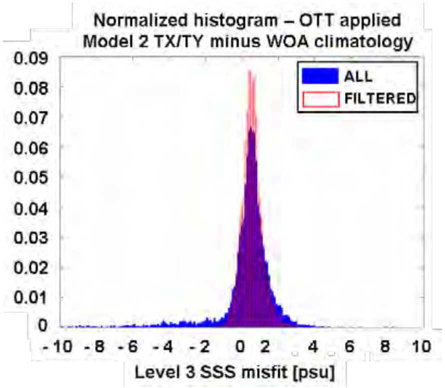

(a)

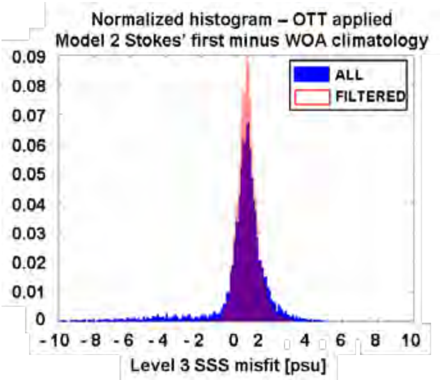

(b)

Figure 6.19: The normalized histograms of the retrieved *SSS* at level 3 when retrieving (a) using T_X/T_Y separately and (b) using Stokes' first parameter in brightness temperature. Blue bars are relative to all the retrieved gridpoints and the red ones only to the gridpoints with a precision lower than 2.5 psu

Table 6.5: Retrieval performance at level 3, Dual form Full-Polarisation vs. Stokes' first form Full-Polarisation.

[psu]	$\mu(SSS_{mis})$	$\sigma(SSS_{mis})$	$rms(SSS_{mis})$
VS. WOA CLIMATOLOGY			
		All points	
Dual	0.2260	2.2565	2.2678
Stokes' first	0.2445	2.3505	2.3631
		Filtered points	
Dual	0.5559	1.4457	1.5489
Stokes' first	0.2935	1.6756	1.7011
VS. WOA CLIMATOLOGY			
		All points	
Dual	0.2958	1.4391	1.4692
Stokes' first	0.6157	1.5464	1.6645
		Filtered points	
Dual	0.5278	0.5805	0.7846
Stokes' first	0.6080	0.5932	0.8495

According to the experiment, using T_X/T_Y separately or Stokes' first parameter on brightness temperature is almost equivalent, slightly better when using T_X/T_Y, at least at level 3. The difference SSS2 minus SSS1 is very homogeneous and does not depend on the geographic position, apart from the zone affected by RFI (North Atlantic Ocean, South China Sea) and the South of Australia, as shown in Fig. 6.18. Normalized histograms are very similar, only small changes have been detected.

6.3.2.3 Model 2 vs. Model 3(16)

In this section retrievals using Model 2 (*Irisov* (1997) and *Johnson and Zhang* (1999)) and Model 3 (*Gabarró et al.*, 2004) in its configuration 16 (tuned with WISE data, (*Camps et al.*, 2004b)) are compared. As in the previous section, performance is assessed through the analysis of the difference figure (Fig. 6.20) the normalized histograms shown in Fig. 6.22 and of Table 6.6. In Fig. 6.22 a and b are the case of retrieving using Model 2 and Model 3(16), respectively. The blue bars are relative to all the retrieved gridpoints and the red ones only to the gridpoints with a precision lower than 2.5 psu. In Table 6.6 μ stands for the mean value and σ is the standard deviation.

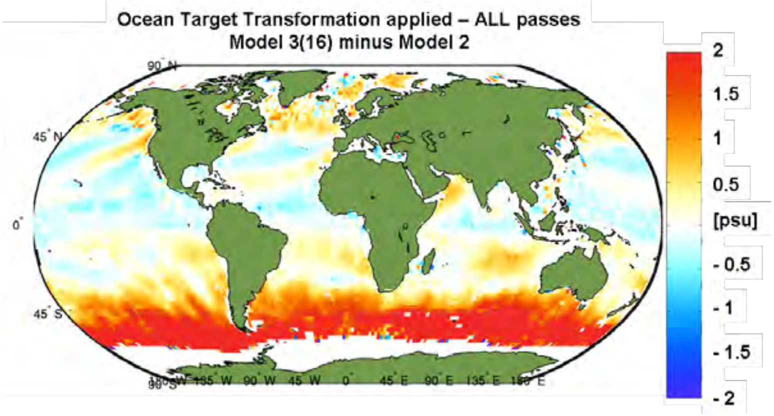

Figure 6.20: Level 3 retrieved *SSS* using model 2 minus using model 3(16)

From Fig. 6.20 can be easily noticed the strong correlation between the difference Model 2/ Model 3(16) and the wind speed and sea surface temperature maps in Fig. 6.9. The only difference between the two cases is, in fact, the modellization of the sea surface roughness contribution to the brightness temperature. Errorbars of the difference between Model 2 and Model 3(16) as a function of wind speed and sea surface temperature are shown in Fig. 6.21a and b, respectively. It is worth to notice that the dependence on the sea surface temperature is just a consequence of the dependence on the wind speed, high wind speed in fact decreases the sea surface temperature of the ocean.

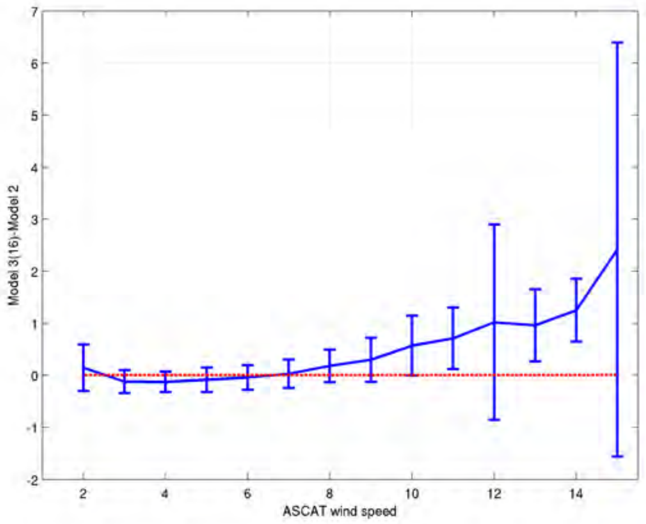

(a)

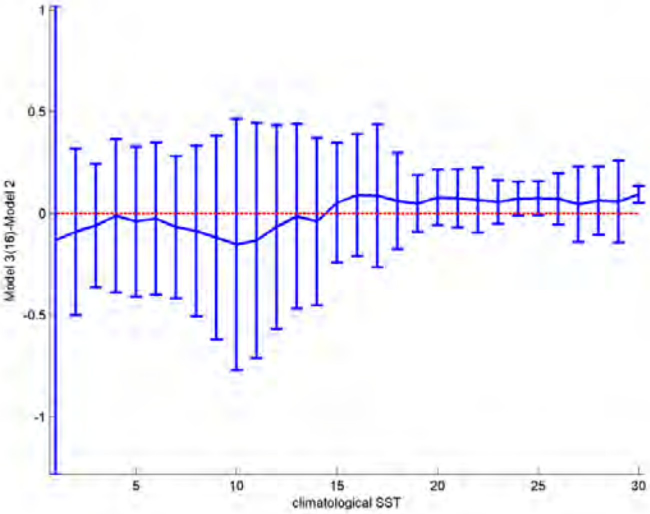

(b)

Figure 6.21: Errorbars of the difference between Model 2 and Model 3(16) for (a) wind speed and (b) sea surface temperature

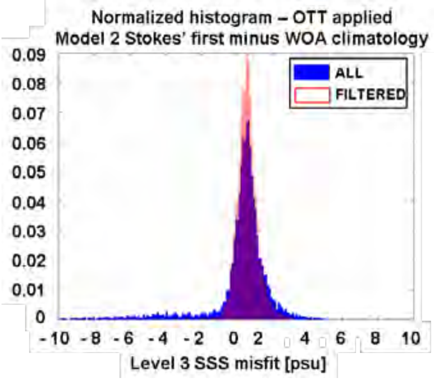

(a)

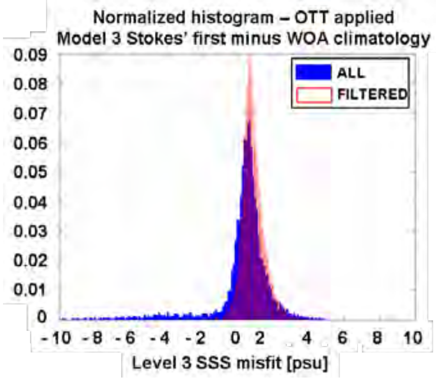

(b)

Figure 6.22: The normalized histograms of the retrieved *SSS* at level 3 when retrieving (a) using Model 2 and (b) using Model 3(16). Blue bars are relative to all the retrieved gridpoints and the red ones only to the gridpoints with a precision lower than 2.5 psu

Table 6.6: Retrieval performance at level 3, Model 2 vs. Model 3(16)

[psu]	$\mu(SSS_{mis})$	$\sigma(SSS_{mis})$	$rms(SSS_{mis})$
VS. WOA CLIMATOLOGY			
		All points	
Model 2	0.2445	2.3505	2.3631
Model 3	0.8302	2.5735	2.7041
		Filtered points	
Model 2	0.6157	1.5464	1.6645
Model 3	0.9346	1.9486	2.1611
VS. AVERAGED ARGO			
		All points	
Model 2	0.2935	1.6756	1.7011
Model 3	0.8490	1.7188	1.9171
		Filtered points	
Model 2	0.6080	0.5932	0.8495
Model 3	0.9522	0.6619	1.1597

According to the histograms and to Fig. 6.20, a 13 % and 21-27% rms increment is observed when retrieving with Model 3(16) instead than Model 2. Model 3 has been derived, in fact, from WISE measurements, acquired in the Mediterranean Sea in conditions quite far from the open ocean ones. The improvement of Model 3 is foreseen during the next months, and new results will be obtained in the next data reprocessing.

6.3.2.4 All vs. Ascending vs. Descending

The last test is one of the current objects of study in the SMOS community: whether using both ascending and descending overpasses in the retrieval or only the first or the second ones. Firstly, the misfit of the retrievals using all, only the ascending, and only the descending overpasses for the case of applying the ocean target transformation, compared with the WOA climatology are shown in Figs. 6.23 a, b, and c, respectively. As can be noticed, land-sea transition strongly affects the results: negative anomalies (waters seem fresher) are detected when the satellite approaches land and positive ones (waters seem saltier) when it leaves it. This effect is partially compensated by summing ascending and descending overpasses.

Normalized histograms are shown in Fig. 6.19 and Table 6.7. In Figs. 6.19 a, b, and c are the case of retrieving using all, only the ascending, or only the descending overpasses, respectively. In Table 6.7 μ stands for the mean value and σ for the standard deviation.

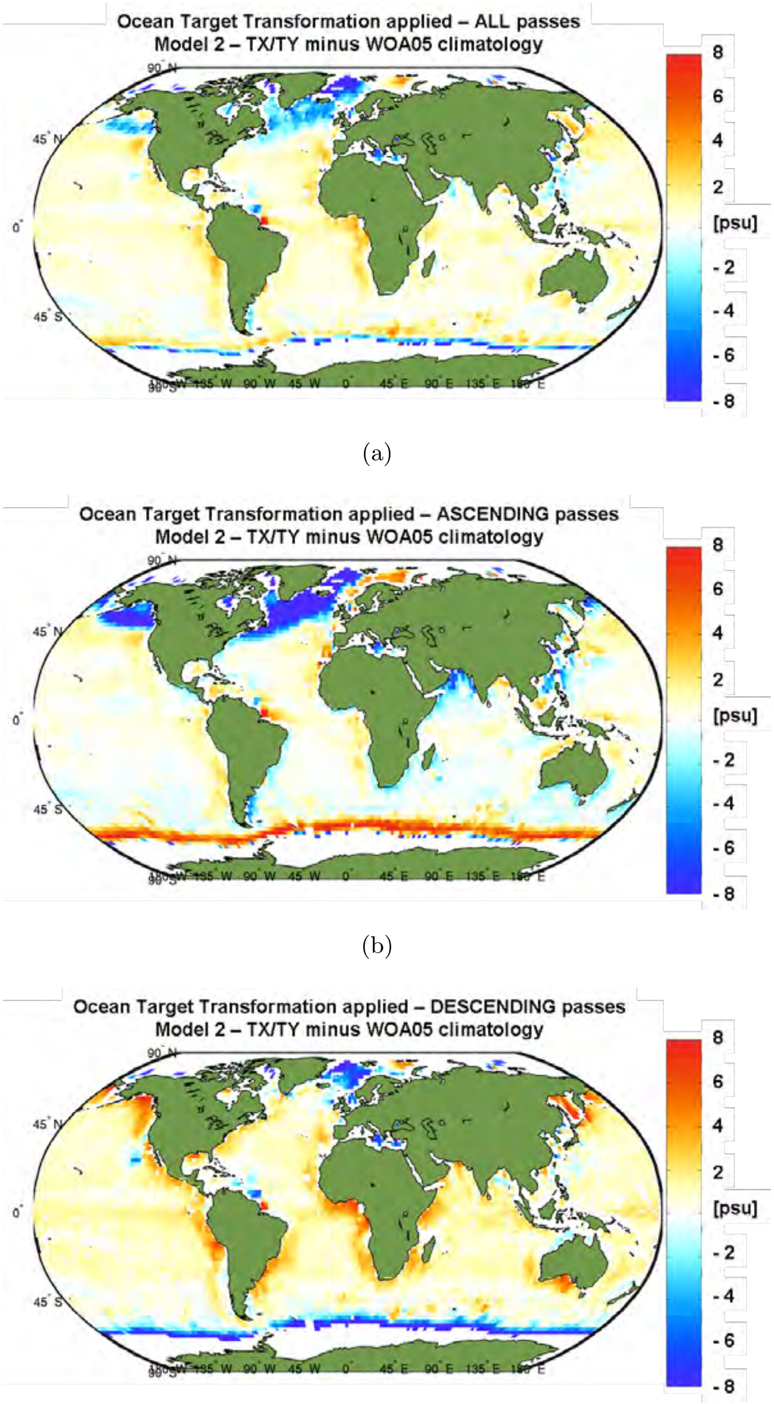

(a)

(b)

(c)

Figure 6.23: Level 3 ten-day average map minus WOA climatology using (a) all, (b) only the ascending, and (c) only the descending overpasses - MODEL 2 DUAL FROM FULL-POL, OTT APPLIED

Table 6.7: Retrieval performance at level 3, All vs. the ascending vs. descending

[psu]	$\mu(SSS_{mis})$	$\sigma(SSS_{mis})$	$rms(SSS_{mis})$
VS. WOA CLIMATOLOGY			
		All points	
All	0.2260	2.2565	2.2678
Ascending	-0.0214	3.3183	3.3183
Descending	0.3851	2.9766	3.0014
		Filtered points	
All	0.5559	1.4457	1.5489
Ascending	0.2175	1.5405	1.5557
Descending	0.9942	1.7178	1.9848
VS. AVERAGED ARGO			
		All points	
All	0.2958	1.4391	1.4692
Ascending	-0.3585	3.0150	3.0362
Descending	0.7824	1.8510	2.0096
		Filtered points	
All	0.5278	0.5805	0.7846
Ascending	0.1239	0.8506	0.8595
Descending	1.0820	0.9610	1.4472

As can be deduced from the histograms and Table 6.7, the performance worsens when only the ascending or descending overpasses are used, this is due the strong land-sea transition effects, which partially compensates when ascending and descending overpasses are considered together. Results improve for the case of using all the overpasses. If the external brightness temperature calibration is used the land-sea transition are less pronounced and the retrieved *SSS* results more homogeneous. Misfit maps, once subtracted the mean bias as in Fig. 6.15, are shown in Fig. 6.24 a and b for the case of using only the ascending or the descending overpasses, respectively. From the statistical point of view results are on the line of the case of using the ocean target transformation, with the best performance when using all the overpasses, in this case there is a preference for the ascending with respect to the descending overpasses. Mean value (μ), standard deviation (σ) and rms of the misift are summarized in 6.8.

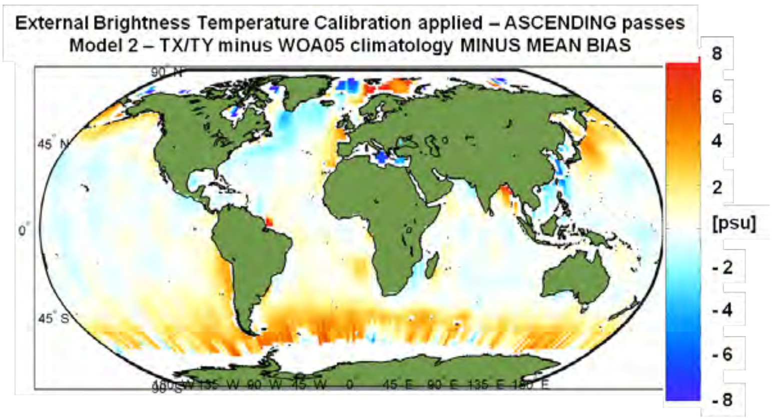

(a)

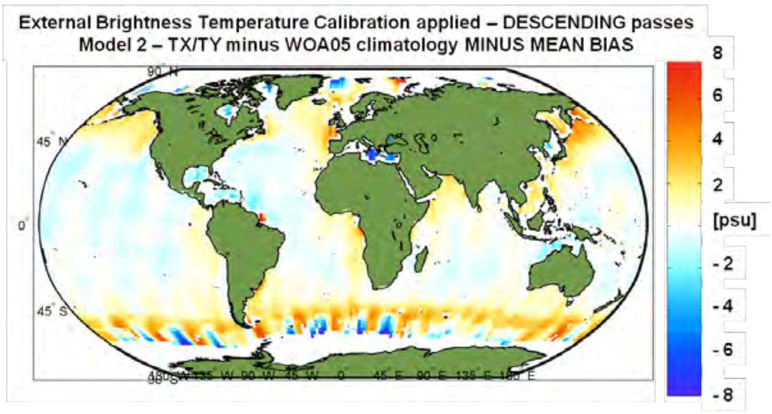

(b)

Figure 6.24: Level 3 ten-day average map minus WOA climatology using (a) all, (b) only the ascending, and (c) only the descending overpasses - MODEL 2 DUAL FROM FULL-POL, EXT TB CALIBRATION APPLIED, MEAN BIAS SUBTRACTED

Table 6.8: Retrieval performance at level 3, All vs. the ascending vs. descending, using External TB Calibration

[psu]	$\mu(SSS_{mis})$	$\sigma(SSS_{mis})$	$rms(SSS_{mis})$
VS. WOA CLIMATOLOGY			
		All points	
All	2.9600	2.3886	3.8036
Ascending	2.8765	2.7368	3.9704
Descending	2.8975	3.1534	4.2825
		Filtered points	
All	2.1981	1.7300	2.7972
Ascending	2.2768	2.4663	3.3566
Descending	2.5100	2.7129	3.6959
VS. AVERAGED ARGO			
		All points	
All	3.2541	1.7764	3.6199
Ascending	2.9333	2.2522	3.6982
Descending	3.2381	2.2810	3.9680
		Filtered points	
All	2.2214	0.5801	2.2959
Ascending	2.2337	1.0301	2.4598
Descending	2.5927	1.5949	3.0440

6.3.3 Conclusions

Ten days of real L1c data from SMOS have been processed using the official SMOS Level 2 OS Processor (*Zine et al.*, 2008) according to three different configurations: *A:* Nominal Product without any calibration; *B:* Applying the external brightness temperature calibration; and *C:* Applying the so-called ocean target transformation. For each one of the cases three different configurations have been tested: *SSS1:* Model 2 (*Irisov*, 1997) and (*Johnson and Zhang*, 1999), in the “Dual from Full-Pol” mode, i.e. retrieving using T_X and T_Y separately; *SSS2:* Model 2 (*Irisov*, 1997) and (*Johnson and Zhang*, 1999), in the “Stokes’ first from Full-Pol” mode, i.e. retrieving using Stokes’ first parameter in brightness temperatures; and *SSS3:* Model 3, configuration 16 (*Gabarró et al.*, 2004), in the “Stokes’ first from Full-Pol” mode. Retrieved *SSS*, averaged to construct level 3 maps, have been compared to WOA05 climatology and ARGO data. Statistics have been caluclated for all the points and only for the points with a retrieval precision lower than 2.5 psu.

SMOS measurements properly reproduce the main structures of the *SSS* field.

Retrieved *SSS* maps are affected by the presence of artifacts, a kind of “shadows” close to the coast of South America, Africa, and Australia due to the Gibbs effect generated by transition land-sea, this feature is under investigation and different mitigation techniques are now being tested. Besides the land-sea transition, RFI is the strongest error source for SMOS, heavy RFI have been detected in the North Pole, China, Europe and South America, several of them have been already turned down during July 2010, anyway this can be yet considered an open issue. Concerning the precision, results are very similar for the three cases, being the ocean target transformation the best configuration.

Case C (ocean target transformation) gives the best performance, while both cases A and B are affected by a positive bias. If all the points are considered, the misfit rms decreases in average 14-20% from the nominal case to using the external brightness temperature calibration, and 52-68% using the ocean target transformation. After the filtering out points with a precision higher than 2.5 psu these improvements become 37-52% in the first case and 73-78% in the second. The best retrieval is achieved with SSS1 (Model 2, Dual from Full-Pol mode) in case C with a misfit rms of 0.78 psu with respect to ARGO data.

Comparing SSS1 and SSS2, results indicate that using T_X/T_Y separately or Stokes’ first parameter on brightness temperature is almost equivalent, at least at level 3. Slightly better performance can be achieved using T_X/T_Y separately, in this way, in fact, the algorithm takes the maximum advantage from the multi-angularity.

Model 2 globally shows better performance than model 3. Anyway it has to be remarked that the latter is still in definition and, in particular, that configuation 16 is the result of a field campaign in the Mediterranean Sea (WISE (*Camps et al.*, 2004b)). If the filtered points statistics is considered, the misfit rms versus ARGO data and WOA climatology is 27-23 % lower (0.8495-1.6645 psu vs. 1.1597-2.1611 psu) if model 2 is used instead of model 3.

Finally, better retievals are obtained if all the overpasses are taken into account, this is due to the strong error associated to the land-sea transitions that affects the retrieval when using only the ascending or the descending overpasses. This effect partially compensates when all the overpasses are considered.

6.3.4 Comparison with simulations

As already stated, the 10-day level 3 product, retrieved using the Stokes' first parameter in brightness temperature, has been synthesized to allow the comparison with the simulations of Chapter 4, this is what this section is devoted to. The statistics of both the simulations and the real case are recall in Table 6.9 for the sake of convenience.

Table 6.9: Retrieval performance at level 3, simulations vs. real retrievals

[psu]	$\mu(SSS_{mis})$	$\sigma(SSS_{mis})$	$rms(SSS_{mis})$
SIMULATIONS			
Open Ocean	-0.1362	0.2239	0.2621
Coastal Zone	0.00559	0.6835	0.6858
REAL RETRIEVAL vs. ARGO			
External TB Calibration	3.3024	1.6341	3.6845
Ocean Target Transf.	0.6080	0.5932	0.8495

In the simulated level 3 product rms error of 0.2621 psu in the Open Ocean and 0.6858 psu in the Coastal Zone were achieved. In the real case, using the external brightness temperature calibration the result is 3.6845 psu. Two main differences between simulations and real retrievals can be found:

- Strong systematic errors, up to 10 K, have been found in the real measurements, which did not exist in the simulations and are not reflected in their results. In the current configuration these errors are corrected by the OTT. If simulations are compared with the OTT case, figures are much more similar with a misfit rms of 0.8495 psu and a standard deviation (0.5932 psu) lying between the simulated 0.2239 psu of the Open Ocean and the 0.6835 psu of the Coastal Zone.

- The residual bias could be attributed to the forward models inaccuracies, especially the ones relative to the sea surface roughness contribution to the brightness temperature. No error concerning the forward modelling was included in the simulations since brightness temperatures were generated and retrieved using the same models while in the second case real brightness temperatures are used. As pointed out in *Sabia et al.* (2006), using different models for generating and retrieving can induce a bias in the retrieval, which, according to the simulation presented in that study, is on the order of 1.3 psu for a monthly product. In the real case there is no forward model, but the inaccuracies of the backward model can conceivably induce bias in the retrieved *SSS*.

7

Conclusions and original contributions

This Ph.D. thesis has been carried out within framework of the SMOS mission, with the aim of improving the level 2 sea surface salinity retrieval algorithm. Several studies are part of it, trying to isolate the problems, looking for ad-hoc solutions. Based the analysis on the SMOS error budget as in *Sabia* (2008) and *Sabia et al.* (2010), the improvement of the level 2 retrieval algorithm has been approached throught the following points:

- The mitigation of the scene-dependent bias in the measurements is the objective of the *External Brightness Temperature Calibration* that allows to pass **from not even retrieving a 5 psu /10° -gradient at 25° C of temperature and no wind (very favourable conditions) to distinguish the 2-psu gradient even with high winds ($\mathbf{U_{10} = 15m/s}$) and low temperatures (SST = 5° C),** as shown in section 4.5.

- The possible L-band forward modeling inaccuracies and their effect on the retrieval are accounted for by the *External Sea Surface Salinity Calibration.* In this case performance improves as detailed in section 4.6:
  At level 2:

  1. The **external salinity calibration remarkably reduces the retrieved *SSS* mean error, while keeping unchanged the standard deviation**, preserving in this way the local variation of salinity within the same snapshot.

2. The mean value of the retrieved *SSS* error is approximately equal to zero, with fluctuations on the order of 0.5 psu, while its standard deviation is almost constant and lower that 1.5 psu within both the so-called “Narrow Swath”.
3. The **proximity of the coast degrades the performance of the *SSS* retrieval, increasing the standard deviation of the error by a factor of between 1.5 and 2. Large errors (3 - 4 psu) are found up to 150 km from the coast and ~1 psu up to 300 km**.
4. **External salinity calibration slightly decreases the error induced by the coastal proximity**: the mean error by 25% (0.5 over 2 psu) and the rms by 10% (0.5 over 5 psu), particularly in the zones with largest errors (low number of observations).

At level 3:

1. The mean error is reduced by more than 15% for 10-day product and by 5% in the 30-day one.
2. The **external salinity calibration only partially mitigates the error caused by the coast proximity for both for the 10- and the 30-day products**.
3. **Level-3 mean error is dominated by the standard deviation of the Level-2 error, and therefore, averaging does not significantly reduce the *SSS* retrieval error**.

- Radiometric sensitivity and accuracy patterns, and their effect on the relative weights used to build the level 2 retrieval cost function have been assessed as explained in Section 5.1. SMOS brightness temperatures misfit covariance matrices have been estimated and a new weight for the observable term of the cost function has been defined. Results suggest that **the current cost functions, although ensuring better performance, may be introducing non-linearities in the retrieval procedure** (causing non-Gaussian retrieved *SSS* error pdf) if compared to the results obtained using directly the misfit covariance matrices. According to previous studies, **non-linearities may be due to a non-optimum balancing of the cost function** that should be modified. Furthermore, **the inclusion of the brightness temperature misfit covariance matrices strongly modifies the error statistics and should be taken into account in the future in the choice of the relative weights**.

The application of the aforementioned techniques on real data proved their validity, namely:

- *The HUT case:* [6.1]
  Applying both techniques, *SSS* has been retrieved with an rms error of approximately 2 psu, which is a very good result considering the instrument characteristics ($\Delta T = 10K$) and the geophysical conditions (coastal region with cold water and very low *SSS*). Moreover, **averaging the results in larger cells** (approximately 1.5 km side), **the error decreases down to 1 psu, allowing to satisfactorily track the *SSS* gradient**.

- *The SMOS case:* [6.2]
  SMOS measurements properly reproduce the main structures of the *SSS* field.

  Land-sea transition strongly affects the retrieved *SSS* quality. It must be noticed that the reconstruction technique presented in *Camps et al.* (2008a) was already implemented in SEPS at the time of the simulation study of Chapter 4, while is not yet included in the official SMOS level 1 processor; this mofication would strongly improve the performance, especially close to the coast. **The second most important error source for SMOS is RFI**, several sources have been already turned down during July 2010, anyway much work is still neede to improve the detection algorithm and introduce some mitigation technique.

  Both External Brightness Temperature Calibration and Ocean Target Transformation improve the level 3 product causing in average a 14-20% and 52-68% decreases of the misfit (level 3 SSS minus climatology and ARGO averaged data) rms with respect to the nominal product, respectively. If only grid-points with a precision lower than 2.5 psu the improvement increases up to 37-52% in the first case and 73-78% in the second. The best retrieval is achieved with SSS1 (Model 2, Dual from Full-Pol mode) in case C with a misfit rms of only 0.78 psu with respect to ARGO data.

  Concerning the retrieval mode, using TX/TY separately or Stokes' first parameter on brightness temperature seems to give very similar results. Anyway, **slightly better performance can be achieved using TX/TY separately**.

  Model 2 globally shows better performance than model 3, as expected. Model 3 is, in fact, still in definition and will be improved for the next SMOS data reprocessing. In figures the level 3 retrieved *SSS* misfit rms versus ARGO data and WOA climatology is 27-23 % lower if model 2 is used instead of model 3, respectively.

Finally, **better retievals are obtained if all the overpasses are taken into account** with respect to using only the ascending or the descending overpasses. This is due to the strong error associated to the land-sea transitions that affects the retrieval when using only the ascending or the descending overpasses. This error partially compensates when all the overpasses are considered.

8

Future research lines

After several years of studies and simulations, SMOS is at last flying and providing real remote sea surface salinity measurements. Nevertheless, researches on this topic are far from stopping, several issues are still open concerning the consolidation of the product on one side, and its exploitation on the other side. Next steps should be, among others:

Data processing consolidation

- As an evolution of both the External Brightness Temperature Calibration and the Ocean Target Transformation, research should be done on the detection of instrumental errors patterns and systematic biases, mainly by performing calibrations and consistency tests at Level 1.
- There is room for improvement also in the characterization of external contaminations such as Solar and galactic reflections, radiofrequency interferences, land and ice borders.
- About the optimal processing, partly analysed in Chapter 5, the retrieval of salinity can be optimized including error modelling (both instrumental and geophysical), a comprehensive quality control, and the assessment of the inversion cost function (including the review of existing formulations as well as the derivation and testing of new ad-hoc formulations).
- Finally, as an advance with respect to the empirical model 3 used inthe current retrievals, the development of a fully empirical model that relates the various geophysical parameters, such as temperature, salinity, and surface wind, to the brightness temperature measured by the instrument can be envisaged.

Oceanografical exploitation

- Firstly, validation and *SSS* product comparison should be foreseen, including moored buoys, profilers, drifters, gliders, oceanographic cruises transects and VOS (Voluntary Observatory Ships).
- Based on advanced downscaling and assimilation techniques, ocean forecasting capabilities could be improved by the inclusion of SMOS measurements.
- A consolidated *SSS* product suitable for process studies and climate analyses can be obtained through data fusion between SMOS and other instruments measurements as well as modelling outputs.

Appendix A

A review of the rain effect on the brightness temperature

It is very easy to imagine that rain can modify both sea surface temperature (*SST*) and salinity (*SSS*). It represents, in fact, a source of fresh, and often colder, water. Nevertheless so easy is to say that it affects *SSS* and *SST* as complex it is to describe and quantify these variations. Most of these changes take place in the top millimeters-centimeters of the sea surface, to which, actually, microwave sensors are most sensitive. This very thin layer is called the *near-surface layer* and it is mostly dominated by the local fluxes of heat, moisture, momentums, and gas from the atmosphere. Several studies have been devoted so far to the better characterization of this important layer (*Soloviev and Lukas* (2006), *Saunders* (1967), *Soloviev and Schluessel* (1996), *Schluessel et al.* (1997), *Craeye and Schluessel* (1998)), and even if direct measurements to validate the models are still a challenge and most of the test have been carried out in laboratories, the basics physics of the phenomena happening in it is wide accepted within the scientific community, and can be summarized as described in the following paragraphs.

A.1 The sea surface microlayer

The sea surface microlayer is defined as the top first few millimeter of the ocean surface. The physics of the sea surface microlayer are related to the fundamental properties of turbulent boundary layers. The transfer of momentum, heat, and mass is controlled by the molecular diffusion, surface organic and inorganic films, result of the interplay between biological, chemic, and physical processes interfere with the air-sea interaction and affect the properties of the molecular layer. The thickness of the microlayer is basically determined by kinematic molecular viscosity, the thermal diffusion coefficient, and diffusivity molecular coefficients. Due to those processes in the top few millimeters of the ocean surface, both temperature and salinity can differ from the ones of the underlying mixed layer, identifying the so-called *cool skin* (*Saunders*, 1967) and *freshwater skin*, respectively. Models accounting for the description of the molecular sub-layers can be divided into two classes: *surface renewal* models and *boundary layers* models. Models belonging to the first class will be objective of this section. The properties of the sublayer are represented as a function of the surface renewal time τ. Environmental parameters controlling the layer instabilities are used to determine τ.

A.2 Surface cooling due to evaporation

Due to the interaction between the sea and the atmosphere, evaporation is one of the most important processes happening in the near-surface layer. During the nighttime, it is often the only one. Naming α_T is the coefficient of thermal expansion in water, g the acceleration of gravity, ν the kinematic molecular viscosity, k_T the thermal molecular conductivity, μ the coefficient for molecular gas diffusion, and h the molecular sublayer depth, in case of stationary meteorological and wave conditions, for the near-surface layer the following set of functional dependencies can be formulated:

$$\begin{aligned}
\overline{\Delta u} &= function\left(u_*, q_0, \alpha_T, g, \nu, k_T, h\right), \\
\overline{\Delta T} &= function\left(u_*, q_0, \alpha_T, g, \nu, k_T, h\right), \\
K_\mu &= function\left(u_*, q_0, \alpha_T, g, \nu, \mu, k_T, h\right),
\end{aligned} \tag{A.1}$$

where $q_0 = Q_0/(c_p\rho) = (Q_T + Q_E + I_L)/(c_p\rho)$, being Q_T the sensible heat flux, Q_E the latent heat flux, I_L the net long-wave irradiance, c_p the specific heat and ρ the sea water density.

To symplify the analysis, the relations in A.1 are expressed also in a dimensionless form, and some useful coefficient are defined. Equations A.1 become:

$$\begin{aligned}
\overline{\Delta u}/u_* &= f_u\left(Rf_0, Ke, Pr\right), \\
\overline{\Delta T}/T_* &= f_T\left(Rf_0, Ke, Pr\right), \\
K_\mu/u_* &= f_C\left(Rf_0, Ke, Pr, Sc\right),
\end{aligned} \tag{A.2}$$

where $T_* = q_0/u_*$, $Rf_0 = (\alpha_T g q_0 \nu)/(u_*^4)$ is the surface Richardson number *Kudryaztsev and Soloviev* (1985), $Ke = u_*^3/(g\nu)$ the Keulegan number *Csanady* (1990), $Pr = \nu/k_T$ the Prandt number, and $Sc = \nu/\mu$ the Schmidt number. At this stage, remembering the hypothesis of no insulation or rain and considering horizontal homogeneity, the molecular diffusion laws can be expressed as:

$$\begin{aligned}
\frac{\partial u}{\partial t} &= \frac{\partial}{\partial z}\left(\nu\frac{\partial u}{\partial z}\right), \\
\frac{\partial T}{\partial t} &= \frac{\partial}{\partial z}\left(k_T\frac{\partial T}{\partial z}\right), \\
\frac{\partial C}{\partial t} &= \frac{\partial}{\partial z}\left(\mu\frac{\partial C}{\partial z}\right),
\end{aligned} \tag{A.3}$$

leading to the solutions:

$$\begin{aligned}
\Delta u(t) &= 2\sqrt{\frac{t}{\pi\nu}}\frac{\tau_t}{\rho}, \\
\Delta T(t) &= -2\sqrt{\frac{t}{\pi k_T}}q_0, \\
\Delta C(t) &= \sqrt{\frac{t}{\pi\mu}}\Delta C.
\end{aligned} \tag{A.4}$$

Indicating a general cooling of the upper layer of the ocean surface and a consequent increase of the salinity.

Considering for each of the equations in A.4 its mean value and taking into account that, according to *Garbe et al.* (2002), the renewal events follow the log-normal distribution in A.5:

$$p(t) = \pi^{-1/2}\,(\sigma t)^{-1}\,exp\left[-(\ln t - m)^2/\sigma^2\right], t > 0 \tag{A.5}$$

Equations A.4 become:

$$\begin{aligned}
\overline{\Delta u} &= \int_0^\infty \frac{1}{t}p(t)\left(\Delta u(t')dt'\right)dt \\
&= \frac{4}{3}\sqrt{\frac{t_*}{\sqrt{\pi\nu}}}\,exp(-\sigma^2/16)\tau_t, \\
\overline{\Delta T} &= \int_0^\infty \frac{1}{t}p(t)\left(\Delta T(t')dt'\right)dt \\
&= \frac{4}{3}\sqrt{\frac{t_*}{\sqrt{\pi k_T}}}\,exp(-\sigma^2/16)q_0, \\
\overline{\Delta C} &= \int_0^\infty \frac{1}{t}p(t)\left(\Delta C(t')dt'\right)dt \\
&= 2\sqrt{\frac{t_*}{\sqrt{\pi\mu}}}\,exp(-3\sigma^2/16),
\end{aligned} \tag{A.6}$$

These expressions are very useful in case of general studies, but if the aim is to compare models to direct measurements, an adequate renewal time, not its mean value, must be used to really assess the viscosity, temperature, and salinity in the near-surface layer. Following *Soloviev and Schluessel* (1994), three different formulas can be applied depending on the wind conditions to obtain the renewal time:

1. *Calm sea or low winds Foster* (1971):

$$t_c = a_c \left(-v/\alpha_T g q_0\right)^{1/2}, \tag{A.7}$$

2. *Intermediate winds Csanady* (1990):

$$t_r = a_r \nu / u_*^2, \tag{A.8}$$

3. *High winds*:

$$t_w = a_w u_*^2 / g. \tag{A.9}$$

The surface Richardson number RF_0 controls the passage from regime 1 to regime 2, while the Keulegan number Ke from regime 2 to regime 3. Summarizing the three cases in one equation A.10 is obtained:

$$\frac{t_*}{(a_r \nu / u_*^2)} = \begin{cases} \left(Rf_0/Rf_{cr}\right)^{-1/2} & \text{at } Rf_0 \geq Rf_{cr} \\ 1 & \text{at } Ke \leq Ke_{cr} \\ Ke/Ke_{cr} & \text{at } Ke \geq Ke_{cr} \end{cases} \tag{A.10}$$

which can be further simplified into:

$$t_* = \left(a_r \nu / u_*^2\right) \left(1 + Rf_0/Rf_{cr}\right)^{-1/2} \left(1 + Ke/Ke_{cr}\right). \tag{A.11}$$

So as to conclude, according to the theory of the renewal time, described in *Kim et al.* (1971), *Liu and Businger* (1975), *Kudryaztsev and Soloviev* (1985), and *Soloviev and Schluessel* (1994), referring to A.5 and A.11, and defining the following coefficient Λ_0:

$$\Lambda_0 = \frac{4}{3\sqrt{\pi}} exp(-\sigma^2/16) \sqrt{a_r} \tag{A.12}$$

for nighttime t_* can be expressed as:

$$t_{*n} = \frac{9\pi\nu}{16 u_*^2} exp(\sigma^2/8) \Lambda_0^2 (1 - a_0^3 \Lambda_0^4 Rf_0)^{-1/2} (1 + Ke/Ke_{cr}). \tag{A.13}$$

applicable only with the assumption of $Rf_0 < 0$.

A.3 Solar radiation effect

The penetration of the solar radiation on the molecular sublayer has basically two effects on its dynamics, as explained in *Soloviev and Lukas* (2006) and *Soloviev and Schluessel* (1996): one the one hand it increases the evaporation of the upper layer on the other hand it leads to a stratification that increases the renewal time. Both effects are explained in the following paragraphs.

The effect on the sea temperature

Considering a fluid element adjacent to the sea surface and participating to the process of cyclic renewal of the surface water, being affected by both surface cooling (always present and modelled in paragraph A.2) and solar radiation absorption, the molecular diffusion law leads the evolution of the temperature difference across the sublayer according to:

$$\frac{\partial T}{\partial t} = \frac{\partial}{\partial z}\left(k_T \frac{\partial T}{\partial z}\right) + \frac{\partial q_R}{\partial z}, \tag{A.14}$$

where k_T is the thermal diffusion coefficient and $q_R = I_R/(c_p\rho)$ is the volume source due to absorption of solar radiation. The boundary and initial conditions are respectively

$$-k_T \left.\frac{\partial T}{\partial z}\right|_{r\to 0} = q_0, \tag{A.15}$$

and

$$T(z,0) = T_w. \tag{A.16}$$

Being $q_0 = (Q_T + Q_E + I_L)/(c_p\rho)$, Q_E and I_L not depending on the the temperature difference across the cool skin, and since Q_T depends of the temperature difference, it is in general much lower than Q_E and I_L and can be considered constant between surface renewals.

Introducing the variable $\Delta T(z,t) = T(z,t) - T_W$, the solution of equation A.14 can be written, separating the two contributions of the cooling and the solar radiation, as:

$$\Delta T(z,t) = \Delta T_C(z,t) + \Delta T_R(z,t), \tag{A.17}$$

where

$$\Delta T_C(z,t) = -\frac{q_0}{\sqrt{k_T \pi}} \int_0^t (t-t')^{-1/2} exp\left\{ -\frac{z^2}{k_T(t-t')} \right\} dt' \ , \tag{A.18}$$

and

$$\Delta T_R(z,t) = \int_0^t \int_{-\infty}^0 \hat{f}(\eta) \left(4k_T\pi(t-t')\right)^{-1/2} exp\left\{ -\frac{(z-\eta)^2}{k_T(t-t')} \right\} d\eta \, dt' \ , \tag{A.19}$$

with $f(z) = \partial q_R/\partial z$. The circumflex denote an even extension of the function t $z > 0$ so that $\hat{f}(z) = \hat{f}(-z)$.

Solving the integrals for the near-surface ($z = 0$) the following expression is obtained:

$$\begin{gathered} \Delta T(0,t) = \Delta T_C(0,t) + \Delta T_R(0,t) = -\tfrac{2q_{R0}}{\sqrt{k_T pi}} t^{1/2} + \\ + \int_0^t \left(4\pi k_T(t-t')\right)^{-1/2} \left(\int_{-\infty}^0 \tfrac{\partial q_{rv}}{\partial(-\eta)} e^{-\frac{\eta^2}{4k_T(t-t')}} d\eta + \int_0^\infty \tfrac{\partial q_{rv}}{\partial(\eta)} e^{-\frac{\eta^2}{4k_T(t-t')}} d\eta \right) dt' \ , \end{gathered} \tag{A.20}$$

Renewal time

When solar radiation is present Rf_0 can become positive and an extension of the definition of surface Richardson number for conditions of solar heating and condensation vapor at ocean surface must be taken into account to adapt A.13.

Under calm weather $Rf \ll -a_0^{-3}\Lambda_0^{-4}$, and the renewal events are mainly due to convective instability. According to *Woods* (1980) a Rayleigh-number criterion can be applied to determine the influence of the solar radiation absorption:

$$Ra(z) = \frac{z^4 \alpha_T g q_{R0} \left[f_R(D) - f_R(z)\right]}{\nu k_T^2}, \tag{A.21}$$

where $f_R(z)$ is the solar radiation absorption function, q_{R0} the solar irradiance just below the surface, and D the compensation depth defined by:

$$q_0 = q_{R0} \left[1 - f_R(D)\right]. \tag{A.22}$$

The maximum of $Ra(z)$ can be found from:

$$\frac{dRa(z)}{dz} = 4\left[f_R(z) - 1 + \frac{q_0}{q_{R0}}\right] + z\frac{df_R(z)}{dz} = 0, \tag{A.23}$$

which, compared to the critical value $Ra_{cr} = 1700$, determines if the stratification induced by the absorption of solar radiation can inhibit the thermally driven convection in the near-surface layer. The new definition of surface Richardson number including this phenomenon is expressed in A.24

$$Rf_0 = \frac{\alpha_T g \nu}{c_p \rho u_*^4} \begin{cases} \left(Q_E + Q_T + I_L + \left(\beta_S S_0 c_p Q_E\right)/\alpha_T L\right) & \text{for } Ra_{max} \geq Ra_{cr}, \\ \left(\beta_S S_0 c_p Q_E\right)/\alpha_T L & \text{for } Ra_{max} < Ra_{cr}. \end{cases} \tag{A.24}$$

A.4 Rainfall effect

Rainfalls induce several changes in the molecular boundary layer of the sea surface, among those:

- The freshwater flux related with the precipitation change the salinity of the upper ocean creating the so-called *freshwater skin* stabilizing the near-surface layer and dampening free convection in the oceanic boundary layer.
- The precipitation is mostly connected with sensible heat flux, being rain a source of usually low-temperature water. Two fluxes can be distinguished, the first one associated to small rain drops not penetrating into the ocean, and the second one caused by the bigger drops submerging into the ocean and gradually decaing with depth.
- Temperature and salinity changes modify the physical constants of sea water.
- Due to the rain drops impact on the ocean surface its roughness increases.
- The impact of rain drops partially or totally removes the surface films.
- Submerging rain drops affect the ordered wave motion and reduce the short gravity waves amplitude causing in this way the decrease of the surface renewal time.
- The impact and penetration of the rain drops into the ocean provoke additional surface renewal events.
- The horizontal momentum of the rain drops is passed to the sea surface increasing the wind stress acting on it.
- Thermodynamic processes take place when the freshwater skin interacts with the underlaying cool skin.

The most important contributions are analyzed in the following paragraphs.

A. A REVIEW OF THE RAIN EFFECT ON THE BRIGHTNESS TEMPERATURE

Water volumes

The rain drops falling onto the ocean can be considered as sphere of radius r_0 which size distribution is commonly described by the Marshall-Palmer distribution, according to A.25:

$$n\left(r_0\right) = \frac{dN}{dr_0} = n_0 exp(-2\Lambda r_0), \tag{A.25}$$

where N is the particle density, $n_0 = 1.6 \cdot 10^4\ m^{-3}mm^{-1}$, and $\Lambda = 4.1R^{-0.21}$, with the rain rate R is expressed in mm/h. The total volume of water can be thus expressed as:

$$V_0 = V_u \int_0^\infty \frac{4}{3}\pi r_0^3 n\left(r_0\right) dr_0 = V_u \int_0^\infty \frac{4}{3}\pi r_0^3 n_0 exp(-2\Lambda r_0) dr_0\ , \tag{A.26}$$

where $V_u = 1\ m^3$ and is necessary for dimensions coherence

According to their size, and then to their mass and kinetic energy, the rain drops can overcome the surface tension and penetrate into the water body. Different critical radius have been defined: $r_c = 0.4\ mm$ in *Oguz and Prosperetti* (1991), and $r_c = 0.75\ mm$ in *Green and Houk* (1979). Considering this radius as the threshold below which rain drops do not have enough kinetic energy to break the ocean surface, the total volume of water remaining at the surface (V_{surf}) and the one penetrating into the ocean (V_{pen}) can be expressed by A.27 and A.28, respectively:

$$V_{surf}(r_c) = V_u \int_0^{r_c} \frac{4}{3}\pi r_0^3 n_0 exp(-2\Lambda r_0) dr_0\ , \tag{A.27}$$

$$V_{pen}(r_c) = V_u \int_{r_c}^\infty \frac{4}{3}\pi r_0^3 n_0 exp(-2\Lambda r_0) dr_0\ . \tag{A.28}$$

Figure A.1 shows the fraction of rain water that remains on the ocean surface and the one that penetrates into it as a function of the rain rate (R) and for two different critical radii: $r_c = 0.4\ mm$ and $r_c = 0.75\ mm$.

Once the surface is broken the volume of the water decays exponentially according to $v(z) = v_0 exp\left(-z/\left(ar_0\right)\right)$, with $a = 100$ (*Manton*, 1973), introducing this dependency A.28 becomes:

$$V_{pen}(z, r_c) = V_u \int_{r_c}^\infty \frac{4}{3}\pi r_0^3 n_0 e^{\left(-2\Lambda r_0 + \frac{-z}{ar_0}\right)} dr_0\ . \tag{A.29}$$

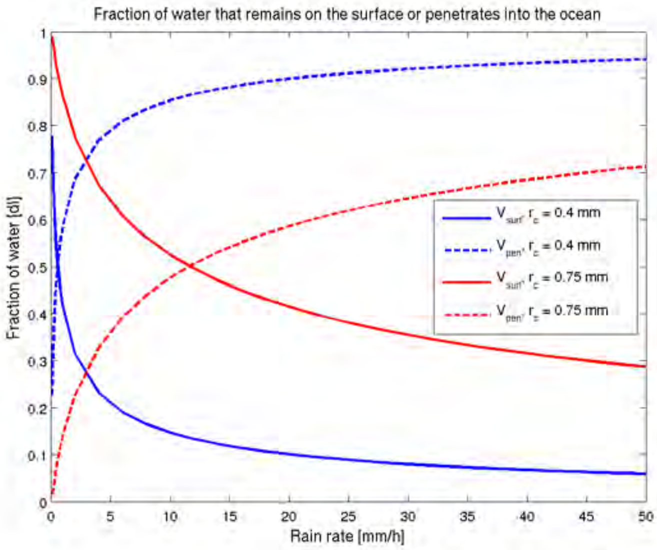

Figure A.1: Fraction of rain water that (solid line) remains on the surface and that (dashed line) penetrates into the ocean for (blue) $r_c = 0.4\ mm$ and (red) $r_c = 0.75\ mm$

Figure A.2 shows the penetration of the rain water into the sea surface according to A.29 for a rain rate of 20 mm/hr and a critical radius of $r_c = 0.75$ and $r_c = 0.4\ mm$. The value at the surface is the same in Fig. A.1.

Temperature and salinity changes due to rain

Temperature and salinity in the near-surface layer change according to the volume of the rain water. Indicating R_s, $q_{rs} = -Q_{rs}/c_p\rho$, R_v, and $q_{rv} = -Q_{rv}/c_p\rho$ the masses and normalized heat fluxes due to the surface and the penetrated water, respectively (being c_p the specific heat and ρ the sea water density), these changes (ΔT and ΔS) can be described by Eqns. A.30 and A.31, respectively:

$$\frac{\partial\left(\Delta T\right)}{\partial t} = \frac{\partial q_{rv}}{\partial z} - \frac{\partial q_{rs}}{\partial z}, \tag{A.30}$$

$$\frac{\partial\left(\Delta S\right)}{\partial t} = \frac{\partial R_s}{\partial z} - \frac{\partial R_v}{\partial z}. \tag{A.31}$$

Solving this system of equations for $z = 0$ leads to:

$$\Delta T_r = \Delta T_{rs} + \Delta T_{rv}, \tag{A.32}$$

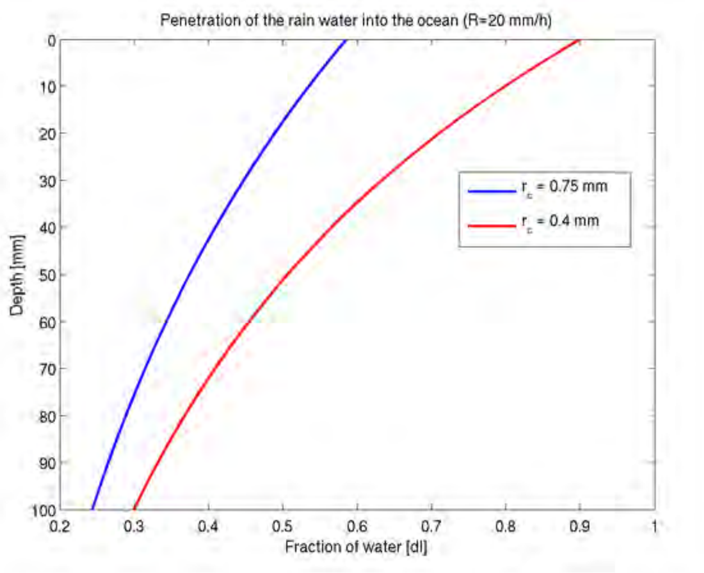

Figure A.2: Penetration of the rain water into the ocean for a rain rate of 20 mm/h and a critical radius of (blue) $r_c = 0.75$ and (red) $r_c = 0.4\ mm$

with

$$\Delta T_{rs}(0,t) = \frac{q_{rs}}{\sqrt{(k_T pi)}} \int_0^t \left(t - t'\right)^{-1/2} dt' = -\frac{2q_{rs}}{\sqrt{k_T pi}} t^{1/2}, \tag{A.33}$$

$$\Delta T_{rv}(0,t) = \int_0^t \frac{1}{\sqrt{4\pi k_T (t-t')}} \left(\int_{-\infty}^0 \frac{\partial q_{rv}}{\partial(-\eta)} e^{-\frac{\eta^2}{4k_T(t-t')}} d\eta + \int_0^\infty \frac{\partial q_{rv}}{\partial(\eta)} e^{-\frac{\eta^2}{4k_T(t-t')}} d\eta \right) dt', \tag{A.34}$$

and

$$\Delta S_r = \Delta S_{rs} + \Delta S_{rv}, \tag{A.35}$$

with

$$\Delta S_{rs}(0,t) = -\frac{2qR_s}{\sqrt{k_T pi}} t^{1/2}, \tag{A.36}$$

$$\Delta S_{rv}(0,t) = \int_0^t \frac{1}{\sqrt{4\pi\mu(t-t')}} \left(\int_{-\infty}^0 \frac{\partial R_v}{\partial(-\eta)} e^{-\frac{\eta^2}{4\mu(t-t')}} d\eta + \int_0^\infty \frac{\partial R_v}{\partial(-\eta)} e^{-\frac{\eta^2}{4\mu(t-t')}} d\eta \right) dt', \tag{A.37}$$

In Eqns. A.33 - A.37, k_T is the thermal molecular conductivity, μ is molecular diffusivity coefficient, t is the renewal time, and q_{rv}, q_{rs}, R_s, and R_v are obtained according to:

$$\begin{aligned} q_{rs} &= R(T_{rain} - T_{sea})\frac{V_{surf}}{V_0}, \\ q_{rv} &= R(T_{rain} - T_{sea})\frac{V_{pen}}{V_0}, \\ R_s &= R(S_{sea})\frac{V_{surf}}{V_0}, \\ R_v &= R(S_{sea})\frac{V_{pen}}{V_0}. \end{aligned} \tag{A.38}$$

The renewal time

Apart from inducing changes in the surface temperature and salinity rain can increase the number of surface-renewal events by promoting additional mixing. This change is mainly caused by the mixing induced by the formation of craters due to the impact of the rain drops on the ocean surface. The impact velocity of the rain drops falling onto the ocean has been expressed by *Best* (1950) as:

$$w_t = \alpha\left[1 - e^{-vr_0^{\lambda}}\right], \tag{A.39}$$

where $\alpha = 9.43\ ms^{-1}$, $v = 0.5650\ mm^{-\lambda}$, and $\lambda = 1.147$. For r_0 between 0.3 mm and 6 mm the A.39 can be approximated by

$$w_t = \alpha\left[b1 - b2e^{-v'r_0}\right]. \tag{A.40}$$

The radius of the craters is directly proportional to square root of this terminal velocity and can be expressed according to *Prosperetti and Oguz* (1993) by:

$$r_k = \varphi_0 r_0\left(\frac{\alpha^2\left[b1 - b2e^{-v'r_0}\right]^2}{gr_0}\right)^{1/4}, \tag{A.41}$$

where $\varphi_0 = (8/3)^{1/4}$.

The crater flux density can, thus, be expressed as (*Craeye and Schluessel* (1998)):

$$\begin{aligned} F_k &= \int_{r_c}^{\infty} \pi r_k r_0^2 n(r_0) w_t(r_0) dr_0 = \\ &= \int_{r_c}^{\infty} \frac{\pi \varphi_0^2}{\sqrt{g}} r_0^{3/2} \left[\alpha \left(b1 - b2e^{-v' r_0}\right)\right]^2 e^{-2\Lambda r_0} \end{aligned} \tag{A.42}$$

leading to a time of renewal due to rain $t_{*r} = 1/F_k$ shown in Fig. A.3 as a function of the rain rate.

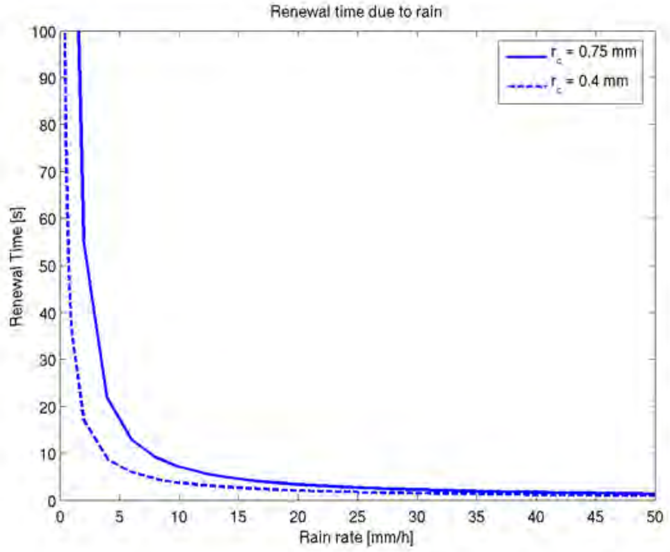

Figure A.3: Time between the renewal events due to rain

An additional source of renewal events is the kinetic energy of the rain drop due to the horizontal component of the rain-drop velocity passed to the ocean surface with the impact. It can be expressed as:

$$E_k = \int_{r_c}^{\infty} \frac{1}{2} \rho R \frac{4}{3} \pi r_0^3 n_0 e^{-2\Lambda r_0} \left[\alpha \left(b1 - b2e^{-v' r_0}\right)\right] dr_0 \, . \tag{A.43}$$

Defining a corresponding additional friction velocity equal to $u_* = \sqrt[3]{E_k/\rho}$, this must be included in the background time of renewal calculation.

A.5 The combined effect

To summarize all these contributions a set of functions in Matlab has been developed. The background time of renewal, considering solar insulation hss been calculated, adding, if necessary, the wind friction velocity associated to the rain precipitation. Apart from that, the time of renewal due only to the rain is calculated and summed to the background according to $1/t_{*t} = 1/t_{*b} + 1/t_{*r}$, to be applied in the calculation of the changes in temperature and salinity.

Appendix B

Publications

Journal publications

1. **M. Talone**, A. Camps, A. Monerris, M. Vall-llossera, P. Ferrazzoli, and M. Piles. Surface topography and mixed pixel effects on the simulated L-band brightness temperatures. *IEEE Trans. on Geosci. and Remote Sens., 45(7): 1996 - 2003,* July 2007.

2. S. Zine, J. Boutin, J. Font, N. Reul, P. Waldteufel, C. Gabarró, J. Tenerelli, F. Petitcolin, J.-L. Vergely, **M. Talone**, and S. Delwart. Overview of the SMOS sea surface salinity prototype processor. *IEEE Trans. on Geosci. and Remote Sens., 46(3): 621 - 645,* March 2008.

3. A. Camps, J. Font, M. Vall-llossera, I. Corbella, N. Duffo, F. Torres, S. Blanch, A. Aguasca, R. Villarino, C. Gabarró, L. Enrique, J. Miranda, R. Sabia, and **M. Talone**. Determination of the sea surface emissivity at L-band and its applications to SMOS salinity retrieval algorithm: Review of the contributions of UPC - ICM. *Radio Sci., 43,* June 2008.

4. C. Gabarró, M. Portabella, **M. Talone**, and J. Font. Towards an optimal SMOS ocean salinity inversion algorithm. *IEEE Geosci. and Remote Sens. Letters, 6(3): 509 - 513,* July 2009.

5. M. Piles, A. Camps, M. Vall-llossera, and **M. Talone**. Spatial resolution enhancement of SMOS data: a deconvolution-based approach. *IEEE Trans. on Geosci. and Remote Sens., 47(7): 2182 - 2192,* July 2009.

6. **M. Talone**, A. Camps, B. Mourre, R. Sabia, M. Vall-llossera, J. Gourrion, C. Gabarró, and J. Font. Simulated SMOS level 2 and 3 products: The effect of introducing ARGO data in the processing chain and its impact on the error induced by the vicinity of the coast. *IEEE Trans. on Geosci. and Remote Sens., 47(9): 3041 - 3050,* September 2009.

7. M. Piles, M. Vall-llossera, A. Camps, **M. Talone**, and A. Monerris. Analysis of a Least-Squares Soil Moisture Retrieval Algorithm from L-band Passive Observations. *MDPI Remote Sensing, 2: 352 - 374,* January 2010.

8. R. Sabia, A. Camps, **M. Talone**, and M. Vall-llossera. Determination of the sea surface salinity error budget in the soil moisture and ocean salinity mission. *IEEE Trans. on Geosci. and Remote Sens., 48(4, part 1): 1684 - 1693,* April 2010.

9. **M. Talone**, R. Sabia, A. Camps, M. Vall-llossera, C. Gabarró, and J. Font. Sea Surface Salinity Retrievals from HUT-2D L-band Radiometric Measurements. *Remote Sensing of the Environment, 114: 1756 - 1764,* 2010. doi: 10.1016/jrse.2010.03.006

10. M. Piles, A. Camps, M. Vall-llossera, A. Monerris, **M. Talone**, and J. Sabater. Performance of Soil Moisture Retrieval Algorithms using Multi-angular L-band Brightness Temperatures. *Water Resources Research, 56: WO6506,* 2010. doi: 10.10209/2009WR008554

11. (IN PRESS)
    G. Jordá, D. Gomis, and **M. Talone**. The SMOS L3 mapping algorithm for Sea Surface Salinity. Part 2: Observational error statistics and prefiltering procedure. *IEEE Trans. on Geosci. and Remote Sens., XX(XX): x - x,* XX.

12. (UNDER REVISION)
    M. Talone, A. Camps, R. Sabia, M. Vall-llossera, C. Gabarró, J. Gourrion, and J. Font. Error covariance matrices characterization in the ocean salinity retrieval cost function within the SMOS mission *Journal of Atmospheric and Oceanic Technology, XX(XX): x - x,* XX.

Conferences and Workshops pubblications

---

1. **M. Talone**, A. Camps, A. Monerris, M. Vall-llossera, P. Ferrazzoli, and M. Piles. Surface topography and mixed pixel effects on the simulated L-band brightness temperatures. In *Proceedings of the IEEE MicroRad, pages 181 - 186,* 2006.

2. R. Sabia, C. Gommenginger, A. Camps, and **M. Talone**. Recent insights in sea surface salinity estimation within the soil moisture and ocean salinity (SMOS) mission. In *Proceedings of the IEEE Gold Remote Sensing Conference,* 2006.

3. J. Font, J. Boutin, N. Reul, P. Waldteufel, C. Gabarró, S. Zine, J. Tenerelli, F. Petitcolin, J.-L. Vergely, and **M. Talone**. An algorithm to retrieve sea surface salinity from SMOS L-band radiometric measurements. In *Proceedings of the International Symposium on Recent Advances in Quantitative Remote Sensing: RAQRSII,* 2007.

4. S. Zine, J. Boutin, J. Font, N. Reul, P. Waldteufel, F. Petitcolin, J.-L. Vergely, C. Gabarró, **M. Talone**, and J. Tenerelli. SMOS sea surface salinity prototype processor: Algorithm validation. In *Proceedings of the IEEE International Geosciences and Remote Sensing Symposium IGARSS, pages 3955 - 3958,* 2007.

5. **M. Talone**, A. Camps, R. Sabia, and J. Font. Towards a coherent sea surface salinity product from SMOS radiometric measurements and argo buoys. In *Proceedings of the IEEE International Geosciences and Remote Sensing Symposium IGARSS, pages 3959 - 3962,* 2007.

6. R. Sabia, A. Camps, M. Vall-llossera, **M. Talone**, and J. Font. Towards an ocean salinity error budget estimation within the SMOS mission. In *Proceedings of the IEEE International Geosciences and Remote Sensing Symposium IGARSS, pages 38 - 41,* 2007.

7. M. Piles, A. Camps, J. L. Alvarez-Perez, M. Vall-llossera, A. Monerris, and **M. Talone**. Deconvolution algorithms in image reconstruction for aperture synthesis radiometers. In *Proceedings of the IEEE International Geosciences and Remote Sensing Symposium IGARSS, pages 1460 - 1463,* 2007.

8. C. Gabarró, M. Portabella, **M. Talone**, and J. Font. Analysis of the SMOS ocean salinity retrieval scheme. In *Proceedings of the IEEE International Geosciences and Remote Sensing Symposium IGARSS, pages 971 - 974,* 2007.

9. J.-L. Vergely, J. Boutin, S. Zine, J. Font, C. Gabarró, **M. Talone**, N. Reul, J. Tenerelli, I. Meirold-Mautner, and F. Petitcolin. Algorithm validation of level

2 sea surface salinity processing. In *Proceedings of the 7th SMOS Workshop on Cal/Val,* 2007.

10. N. Reul, J. Tenerelli, J. Boutin, S. Zine, J. Font, C. Gabarró, **M. Talone**, J.-L. Vergely, F. Petitcolin, and I. Meirold-Mautner. Validation of sea surface salinity processing algorithm used for SMOS ground segment. In *Proceedings of the 7th SMOS Workshop on Cal/Val,* 2007.

11. C. Gabarró, **M. Talone**, and J. Font. Roughness empirical model derived from SMOS data. In *Proceedings of the 7th SMOS Workshop on Cal/Val,* 2007.

12. J. Font, J. Boutin, N. Reul, P. Waldteufel, C. Gabarró, S. Zine, J. Tenerelli, **M. Talone**, F. Petitcolin, J.-L. Vergely, and S. Delwart. Status and description of level 2 products and algorithm (salinity). In *Proceedings of the 7th SMOS Workshop on Cal/Val,* 2007.

13. A. Camps, **M. Talone**, M. Vall-llossera, A. Monerris, and P. Ferrazzoli. The SMOS End-to-end Performance Simulator (SEPS): Recent improvements in support to the SMOS cal/val. In *Proceedings of the 7th SMOS Workshop on Cal/Val,* 2007.

14. C. Gabarró, J. Font, and **M. Talone**. Smos: Measuring sea surface salinity from space. In *Proceedings of the Second International Workshop on MARine TECHnology, MARTECH,* 2007.

15. R. Sabia, A. Camps, **M. Talone**, M. Vall-llossera, and J. Font. Does SMOS accomplish godae requirements? issues concerning satellite salinity retrieval. In *Proceedings of the Final Symposium on the Global Ocean Data Assimilation Experiment (GODAE),* 2008.

16. **M. Talone**, A. Camps, B. Mourre, R. Sabia, M. Vall-llossera, C. Gabarró, and J. Font. The impact of combining SMOS and ARGO data on the SMOS level 2 and 3 products and effect of the vicinity of the coast. In *Proceedings of the IEEE MicroRad,* 2008.

17. R. Sabia, A. Camps, M. Vall-llossera, and **M. Talone**. Extended ocean salinity error budget analysis within the SMOS mission. In *Proceedings of the IEEE International Geosciences and Remote Sensing Symposium IGARSS,* 2008.

18. **M. Talone**, A. Camps, C. Gabarró, R. Sabia, J. Gourrion, M. Vall-llossera, B. Mourre, and J. Font. Contributions to the improvement of the SMOS level

2 retrieval algorithm: Optimization of the cost function. In *Proceedings of the IEEE International Geosciences and Remote Sensing Symposium IGARSS,* 2008.

19. M. Piles, A. Camps, M. Vall-llossera, and **M. Talone**. Spatial resolution enhancement of SMOS data: A combined fourier wavelet approach. In *Proceedings of the IEEE International Geosciences and Remote Sensing Symposium IGARSS,* 2008.

20. J. F. Marchan-Hernandez, M. Vall-llossera, A. Camps, N. Rodriguez-Alvarez, I. Ramos-Perez, E. Valencia, X. Bosch-Lluis, **M. Talone**, J. M. Tarongi, and M. Piles. Ground-based GNSS-R measurements with the PAU instrument and their application to the sea surface salinity retrieval: First results. In *Proceedings of the IEEE International Geosciences and Remote Sensing Symposium IGARSS,* 2008.

21. R. Sabia, A. Camps, **M. Talone**, and M. Vall-llossera. The SMOS mission retrieval scheme: the ocean salinity error budget. In *Proceedings of the IEEE Gold Remote Sensing Conference,* 2008.

22. R. Sabia, A. Camps, M. Portabella, **M. Talone**, J. Ballabrera, J. Gourrion, C. Gabarró, A. L. Aretxabaleta, and J. Font. On the balancing of the SMOS ocean salinity retrieval cost function. In *Proceedings of the European Geosciences Union EGU General Assembly,* 2009.

23. C. Gabarró, **M. Talone**, and J. Font. Analysis of L-band radiometric data over the Mediterranean sea from the SMOS validation rehearsal campaign. In *Proceedings of the European Geosciences Union EGU General Assembly,* 2009.

24. **M. Talone**, A. Camps, J. F. Marchan-Hernandez, J. M. Tarongi, M. Piles, X. Bosch-Lluis, I. Ramos-Perez, E. Valencia, N. Rodriguez-Alvarez, M. Vall-llossera, and P. Ferr. Preliminary results of the Advanced L-band Transmission and Reection Observation of the Sea Surface (ALBATROSS) campaign: Preparing the SMOS calibration and validation activities. In *Proceedings of the IEEE International Geosciences and Remote Sensing Symposium IGARSS,* 2009.

25. R. Sabia, A. Camps, **M. Talone**, J. Gourrion, J. Ballabrera, M. Vall-llossera, and J. Font. Meridional variability in SMOS salinity retrievals: Trade-Off between sensitivity to geophysical effects ad increased temporal sampling. In *Proceedings of the IEEE International Geosciences and Remote Sensing Symposium IGARSS,* 2009.

26. M. Piles, A. Camps, M. Vall-llossera, A. Monerris, **M. Talone**, A. Aguasca, and R. Acevo. Downscaling of SMOS-derived soil moisture during SMOS calibration/validation phase in the central part of the Duero basin. In *Proceedings of the IEEE International Geosciences and Remote Sensing Symposium IGARSS,* 2009.

27. R. Sabia, A. Camps, M. Portabella, **M. Talone**, J. Ballabrera, J. Gourrion, A. L. Aretxabaleta, C. Gabarró, and J. Font. Issues in the balancing of the SMOS ocean salinity retrieval cost function. In *Proceedings of the Third International Workshop on MARine TECHnology, MARTECH,* 2009.

28. R. Sabia, J. Gourrion, C. Gabarró, **M. Talone**, M. Portabella, J. Ballabrera, J. Martinez, A. L. Aretxabaleta, A. Camps, A. Monerris, J. Font. SMOS measurements preliminary validation: Objectives and approach. In *Proceedings of the European Geosciences Union EGU General Assembly,* 2010.

29. J. Gourrion, **M. Talone**, R. Sabia, C. Gabarró, V. Gonzalez, A. Camps, I. Corbella, A. Monerris, J. Font. SMOS brightness temperatures validation: Preliminary results of the commissioning phase. In *Proceedings of the European Geosciences Union EGU General Assembly,* 2010.

30. **M. Talone**, J. Gourrion, V. Gonzalez, R. Sabia, A. Camps, I. Corbella, A. Turiel, A. Monerris, J. Font. SMOS' brightness temperatures statistical characterization. In *Proceedings of the ESA Living Planet Symposium*, Bergen, Norway, 2010.

31. C. Gabarró, A. Turiel, J. Martinez, M. Portabella, **M. Talone**, R. Sabia, J. Font. Improvement of the empirical roughness-induced emissivity model for the SMOS mission. In *Proceedings of the ESA Living Planet Symposium*, Bergen, Norway, 2010.

32. P. Spurgeon, J. Font, J. Boutin, N. Reul, J. Tenerelli, J.-L. Vergely, C. Gabarró, X. Yin, S. Lavender, A. Chuprin, M. McCulloch, C. Henocq, J. Gourrion, **M. Talone**, P. Waldteufel. Ocean salinity retrieval approaches for the SMOS satellite. In *Proceedings of the ESA Living Planet Symposium*, Bergen, Norway, 2010.

33. J. Font, J. Boutin, N. Reul, P. Spurgeon, J. Ballabrera, A. Chuprin, C. Gabarró, J. Gourrion, C. Henocq, S. Lavender, N. Martin, J. Martinez, M. McCulloch, I. Meirold-Mautner, F. Petitcolin, M. Portabella, R. Sabia, **M. Talone**, J. Tenerelli, A. Turiel, J.-L. Vergely, P. Waldteufel, X. Yin, S. Zine. Overview of SMOS

level 2 ocean salinity processing and first results. In *Proceedings of the IEEE International Geosciences and Remote Sensing Symposium IGARSS,* 2010.

34. **M. Talone**, J. Gourrion, R. Sabia, C. Gabarró, V. Gonzalez, A. Camps, I. Corbella, A. Monerris, J. Font. SMOS' brightness temperatures validation: first results after the commissioning phase. In *Proceedings of the IEEE International Geosciences and Remote Sensing Symposium IGARSS,* 2010.

35. R. Sabia, J. Gourrion, M. Portabella, C. Gabarró, **M. Talone**, J. Ballabrera, A. Turiel, J. Martinez, A. Camps, A. Lopez de Aretxabaleta, A. Monerris, J. Font.SMOS' measurements preliminary validation against modeled brightness temperatures and external-source salinity data. In *Proceedings of the IEEE International Geosciences and Remote Sensing Symposium IGARSS,* 2010.

References

Consultative meeting in soil moisture ocean salinity: Measurement requirements and radiometer techniques, ESA, 1995. 39, 42

Anterrieu, E., and A. Camps, On the reduction of the systematic error in imaging radiometry by aperture synthesis: a new approach for the smos space mission, in *Proceedings of the IEEE MicroRad*, 2008. 43, 92, 106

Barlow, R., *Statistics, A Guide to the Use of Statistical Methods in the Physical Sciences*, The Manchester Physics Series, John Wiley & Sons, 1989. 100

Barré, H. M. J. P., B. Duesmann, and Y. H. Kerr, Smos: The mission and the system, *IEEE Trans. on Geosci. and Remote Sens.*, *46*(3), 587–593, 2008. 70, 99

Best, A., The size distribution of raindrops, *Quarterly Journal of the Royal Meteorological Society*, *76*, 16–36, 1950. 165

Blanch, S., and A. Aguasca, Seawater dielectric permittivity model from measurements at l band, in *Proceedings of the IEEE International Geosciences and Remote Sensing Symposium IGARSS*, pp. 1362–1365, 2004. 23

Boutin, J., and N. Martin, Argo upper salinity measurements: Perspectives for l-band radiometer calibration and retrieved sea surface salinity validation, *IEEE Geosci. and Remote Sens. Letters*, *3*(2), 202–206, 2006. 57, 58

Burgees, T. M., and R. Webster, Optimal interpolation and isarithmic mapping of soil properties; i the semi-variogram and punctual kriging, *European Journal of Soil Science*, *31*(2), 315, 1980. 58, 62

Butora, R., and A. Camps, Noise maps in aperture synthesis radiometric images due to cross correlation of visibility noise, *Radio Sci.*, *38*(4), 1067, 2003. 92, 96

Camps, A., J. Bara, I. Corbella, and F. Torres, The processing of hexagonally sampled signals with standard rectangular techniques: Application to 2-d large aperture synthesis interferometric radiometer, *IEEE Trans. on Geosci. and Remote Sens.*, *35*(1), 183–190, 1997. 43, 48

Camps, A., I. Corbella, M. Vall-llossera, N. Duffo, F. Marcos, F. Martinez-Fadrique, and M. Greiner, The smos end-to-end performance simulator: Description and scientific applications, in *Proceedings of the IEEE International Geosciences and Remote Sensing Symposium IGARSS*, pp. 13–15, 2003. 54, 86, 93

Camps, A., M. Vall-llossera, L. Batres, F. Torres, N. Duffo, and I. Corbella, Retrieving sea surface salinity with multiangular l-band brightness temperatures: Improvement by spatio-temporal averaging, *Radio Sci.*, *40*, 2005a. 54, 90, 92, 105, 107, 125

Camps, A., M. Vall-llossera, I. Corbella, N. Duffo, and F. Torres, Improved image reconstruction algorithm for aperture synthesis radiometers, *IEEE Trans. on Geosci. and Remote Sens.*, *46*(1), 146–158, 2008a. 43, 54, 61, 92, 106, 125, 151

Camps, A., et al., L-band sea surface emissivity: Preliminary results of the wise-2000 campaign and its application to salinity retrieval in the smos mission, *Radio Sci.*, *38*, 2004a. 28, 86

Camps, A., et al., The wise 2000 and 2001 field experiment in support of the smos mission: sea surface salinity retrieval, *IEEE Trans. on Geosci. and Remote Sens.*, *42*(4), 804–823, 2004b. 28, 29, 107, 114, 137, 147

Camps, A., et al., The emissivity of foam-covered water surface at l-band: Theoretical modeling and experimental results from the frog 2003 field experiment, *IEEE Trans. on Geosci. and Remote Sens.*, *43*(5), 925–937, 2005b. 26

Camps, A., et al., Determination of the sea surface emissivity at l-band and its applications to smos salinity retrieval algorithm: Review of the contributions of upc - icm, *Radio Sci.*, *43*, 2008b. 105

CDTI, Centro para el desarrollo tecnologico industrial, www.cdti.es. 44

CEOS, Committee on earth observation satellites, www.ceos.org. 49

Claassen, J. P., and A. K. Fung, The recovery of polarized apparent temperature distributions of flat scenes from antenna temperature measurements, *IEEE Trans. on Antennas and Propagation*, *AP-22*(3), 433–442, 1974. 35

CNES, Centre national detudes spatiales, www.cnes.fr. 44

CORIOLIS, Coriolis project, http://www.coriolis.eu.org/. 58, 62

CP-34, Centro procesado niveles 3 y 4, www.cp34-smos.icm.csic.es. 50

Craeye, C., and P. Schluessel, Rainfall on the sea: surface renewals and wave damping, *Boundary-Layer Meteorology*, *89*, 349–355, 1998. 155, 165

Csanady, G. T., The role of breaking wavelets in air-sea gas transfer, *J. Geophys. Res.*, *95*, 749–759, 1990. 156, 158

Dinnat, E., J. Boutin, G. Caudal, and J. Etcheto, Issues concerning the sea emissivity modeling at l band for retrieving surface salinity, *Radio Sci.*, *38*(4), 2003. 25, 55, 125

Duffo, N., et al., Some results of the miras-smos demonstrator campaigns, in *Proceedings of the IEEE International Geosciences and Remote Sensing Symposium IGARSS*, pp. 3639–3642, 2007. 105

Ellison, W., A. Balana, G. Delbos, K. Lamkaouchi, L. Eymard, C. Guillon, and C. Prongent, New permittivity measurements of sea water, *Radio Sci.*, *33*(3), 639–648, 1998. 23

EUROCKOT, Eurockot website, www.eurockot.com. 44

Font, J., G. Lagerloef, D. LeVine, A. Camps, and O. Z. Zanife, The determination of surface salinity with the european smos space mission, *IEEE Trans. on Geosci. and Remote Sens.*, *42*(10), 2196–2205, 2004. 39

Font, J., C. Gabarró, and B. Mourre, Synergetic aspects and auxiliary data concepts for sea surface salinity measurements from space - wp4000: Summary, synthesis and recommendations - final report, *Tech. rep.*, ESA, 2005. 91, 96

Font, J., A. Camps, and J. Ballabrera, *Microwave Aperture Synthesis Radiometry: Setting the Path for (Operational) Sea Salinity Measurement from Space, Remote Sensing of European Seas*, Springer Netherlands, 2008. 92

Foster, T. D., Intermittent convection, *Geophys. Fluid Dyn.*, *2*, 201–271, 1971. 158

Fung, A. K., *Microwave Scattering and Emission. Models and Theirs Applications*, Artech House, Boston-London, 1994. 25

Gabarró, C., J. Font, A. Camps, M. Vall-llossera, and A. Julia, A new empirical model of sea surface microwave emissivity for salinity remote sensing, *Geophys. Res. Lett.*, *31*, 2004. 29, 55, 120, 126, 137, 146

Gabarró, C., M. Portabella, M. Talone, and J. Font, Towards an optimal smos ocean salinity inversion algorithm, *IEEE Geosci. and Remote Sens. Letters*, *6*(3), 509–513, 2009. 90, 101, 105

Garbe, C. S., B. Jaehne, and H. Haussecker, Measuring the sea surface heat flux and probability distribution of the surface renewal events, *AGU Monograph Gas Transfer at Water Surface*, pp. 109–114, 2002. 157

Goodberlet, M., and J. Miller, Npoess sea surface salinity. technical report, *Tech. Rep. contract 43AANE704017*, NOAA, USA, 1997. 108

Green, T., and D. F. Houk, The mixing of rain with near-surface water, *J. Fluid Mech.*, (90), 569–588, 1979. 162

Hollinger, J. P., Passive microwave measurements of sea surface roughness, *IEEE Transactions on Geoscience Electronics*, *GE-9*(3), 165–169, 1971. xi, 27, 29, 93

Irisov, V. G., Small-slope expansion for thermal and reflected radiation from a rough surface, *Waves in Random Media*, *7*, 1–10, 1997. 25, 55, 120, 125, 137, 146

Johnson, J. T., and M. Zhang, Theoretical study of the small slope approximation for ocean polarimetric thermal emission, *IEEE Trans. on Geosci. and Remote Sens.*, *37*(5), 2305–2316, 1999. 25, 55, 120, 125, 137, 146

Kainulainen, J., M. Takala, and M. Hallikainen, Radiometric performance of interferometric synthetic aperture radiometer hut-2d, in *Proceedings of the IEEE International Geosciences and Remote Sensing Symposium IGARSS*, 2007. 106

Kalnay, E., et al., The ncep/ncar 40-year reanalysis project, *Bulletin of American Meteorology Society*, *77*(3), 437–471, 1996. 62, 94

Kim, H. T., S. J. Kline, and W. C. Reynolds, The production of turbulence near a smooth wall in a turbulent boundary layer, *J. Fluid Mech.*, *50*, 133–160, 1971. 158

Klein, L. A., and C. T. Swift, An improved model for the dielectric constant of sea water at microwave frequencies, *IEEE J. Ocean. Eng.*, *OE-2*(1), 104–111, 1977. 23, 55, 93, 107, 125

Kudryaztsev, V. N., and A. V. Soloviev, On parametrization of cool skin of the ocean, *Atmospheric and Oceanic Physics*, *21*(2), 177–183, 1985. 156, 158

Lagerloef, G., C. T. Swift, and D. LeVine, Sea surface salinity: The next remote sensing challenge, *Oceanography*, *8*(2), 44–50, 1995. 2

LeVine, D., and S. Abraham, The effect of the ionosphere on remote sensing of sea surface salinity from space: Absorption and emission at l band, *IEEE Trans. on Geosci. and Remote Sens.*, *40*(4), 771–782, 2002. 33, 34, 35, 54

LeVine, D., M. Kao, R. W. Garvine, and T. Sanders, Remote sensing of ocean salinity: Results from the delaware coastal current experiment, *Journal of Atmospheric and Oceanic Technology*, *15*, 1478–1484, 1998. 53

Levitus, S., Nodc world ocean atlas 1998 data, report, 1998 :noaa-cires, *Tech. rep.*, Clim. Diag. Cent., Boulder, Colorado, 1998. 62, 94

Liu, W. T., and J. A. Businger, Temperature profile in the molecular sublayer near the interface of fluid in turbulent motion, *Geophys. Res. Lett.*, *2*, 403–404, 1975. 158

Madec, G., Nemo ocean engine, 2008. 62, 94

Manton, M. J., On the attenuation of sea waves by rain, *Geophys. Fluid Dyn.*, *5*, 249–260, 1973. 162

McMullan, K. D., M. Brown, M. Martin-Neira, W. Rits, S. Ekhlom, J. Marti, and J. Lemanczyk, Smos: The payload, *IEEE Trans. on Geosci. and Remote Sens.*, *46*(3), 594–605, 2008. 39, 44

Meirold-Mautner, I., C. Mugerin, J.-L. Vergely, P. Spurgeon, F. Rouffi, and N. Meskini, Smos ocean salinity performance and tb bias correction, in *Proceedings of the European Geosciences Union EGU General Assembly*, 2009. 120, 126

Meissner, T., and F. Wentz, The complex dielectric constant of pure and sea water from microwave satellite observations, *IEEE Trans. on Geosci. and Remote Sens.*, *42*(9), 2004. 23

Mourre, B., J. Ballabrera, E. Garcia-Ladona, and J. Font, Surface salinity response to changes in the model parameters and forcings in a climatological simulation of the eastern north-atlantic ocean, *Ocean Modelling*, *23*(1-2), 21–32, 2008. 62, 94

Oguz, H. N., and A. Prosperetti, Numerical calculation of the underwater noise of rain, *J. Fluid Mech.*, *228*, 417–442, 1991. 162

Planck, M., On the law of distribution of energy in the normal spectrum, *Annalen der Physik*, *4*, 553ff, 1901. 6, 8

Prosperetti, A., and H. N. Oguz, The impact of drops on liquid surfaces and the underwater noise of rain, *Ann. Rev. Fluid Mech.*, *25*, 577–602, 1993. 165

Randa, J., et al., Recommended terminology for microwave radiometry, *Tech. Rep. 1551*, National Institute of Standards and Technology, 2008. 18, 94, 96, 108

Rautiainen, K., J. Kainulainen, T. Auer, S. Tauriainen, and M. Hallikainen, Helsinki university of technology synthtic aperture radiometer - hut-2d, in *Proceedings of the IEEE International Geosciences and Remote Sensing Symposium IGARSS*, pp. 3635–3638, 2007. 106, 118

Rautiainen, K., J. Kainulainen, T. Auer, J. Pihlflyckt, J. Kettunen, and M. Hallikainen, Helsinki university of technology l-band airborne synthetic aperture radiometer, *IEEE Trans. on Geosci. and Remote Sens.*, *46*(3), 717–726, 2008. 106, 118

Reul, N., B. Chapron, E. Obligis, S. Labroue, O. Boone, and O. Z. Zanife, Salinity data processing study, *Tech. Rep. contract N15165/01/NL/SF WP1100-WP3000*, ESA, 2001. 25, 55, 126

Reul, N., J. Tenerelli, N. Floury, and B. Chapron, Earth-viewing l-band radiometer sensing of sea surface scattered celestial sky radiation - part ii: Application to smos, *IEEE Trans. on Geosci. and Remote Sens.*, *46*(3), 675–688, 2008. 53

Ribo, S., and M. Martin-Neira, Faraday rotation correction in the polarimetric mode of miras, *IEEE Trans. on Geosci. and Remote Sens.*, *42*(7), 1405–1410, 2004. 35

Rodgers, J. L., and W. A. Nicewander, Thirteen ways to look at the correlation coefficient, *The American Statistician*, *42*(1), 59–66, 1988. 94

Sabia, R., Sea surface salinity retrieval error budget within the esa soil moisture and ocean salinity mission, Ph.D. thesis, Universitat Politècnica de Catalunya, 2008. iv, 51, 109, 149

Sabia, R., A. Camps, M. Vall-llossera, and N. Reul, Impact on sea surface salinity retrieval of different auxiliary data within the smos mission, *IEEE Trans. on Geosci. and Remote Sens.*, *44*(10), 2769 – 2778, 2006. 53, 91, 96, 148

Sabia, R., A. Camps, M. Talone, and M. Vall-llossera, Determination of the sea surface salinity error budget in the soil moisture and ocean salinity mission, *IEEE Trans. on Geosci. and Remote Sens.*, *48*(4), 1684–1693, 2010. iv, 51, 101, 109, 149

Saunders, P. M., The temperature at the ocean-air interface, *J. Atmos. Sci.*, *24*, 269–273, 1967. 155, 156

Schluessel, P., A. V. Soloviev, and W. J. Emery, Cool and freshwater skin of the ocean during rainfall, *Boundary-Layer Meteorology*, *82*, 437–472, 1997. 155

Seo, J., and J. P. Breidenbach, Real-time correction of spatially nonuniform bias in radar rainfall data using gauge measurements, *J. Hydrometeorol.*, *3*(2), 93–111, 2002. 55, 126

SEPS ADDD, Seps architectural and detailed design document (addd), available at http://cassiopea.estec.esa.int/SEPS/Documents/. 86, 93

SEPS SUM, Seps software user manual (sum) version 4.0, available at http://cassiopea.estec.esa.int/SEPS/Documents/. 99

Smith, N., and M. Lefrèbvre, The global ocean data assimilation experiment (godae); monitoring the oceans in the 2000s: An integrated approach, in *Proceedings of the Symposium on the Global Ocean Data Assimilation Experiment (GODAE)*, 1997. 44

SMOS MRD, Smos mission requirements document, avilable at www.cp34-smos.icm.csic.es/img_enlaces/SMOS_MRD_V5.pdf. 44

SMOS website, Esa smos mission website, http://www.esa.int/esaLP/LPsmos.html. 43

Snyder, J. P., An equal-area map projection for polyhedral globes, *Cartographica*, *29*(1), 10–21, 1992. 92, 120

Soloviev, A. V., and R. Lukas, *The near-surface layer of the ocean*, Springer, 2006. 155, 159

Soloviev, A. V., and P. Schluessel, Parametrization of the temperature difference across the cool skin of the ocean and of he air-ocean gas tranfer on the basis of modelling surface renewal, *J. Phys. Oceanogr.*, *24*, 1339–1346, 1994. 158

Soloviev, A. V., and P. Schluessel, Evolution of cool skin and direct air-sea gas transfer coefficient during daytime, *Boundary-Layer Meteorology*, *77*, 45–68, 1996. 155, 159

Talone, M., A. Camps, A. Monerris, M. Vall-llossera, P. Ferrazzoli, and M. Piles, Surface topography and mixed pixel effects on the simulated l-band brightness temperatures, *IEEE Trans. on Geosci. and Remote Sens.*, *45*(7), 1996–2003, 2007a. 86

Talone, M., A. Camps, R. Sabia, and J. Font, Towards a coherent sea surface salinity product from smos radiometric measurements and argo buoys, in *Proceedings of the IEEE International Geosciences and Remote Sensing Symposium IGARSS*, pp. 3959–3962, 2007b. 54, 58, 86, 96, 107, 109

Talone, M., A. Camps, B. Mourre, R. Sabia, M. Vall-llossera, J. Gourrion, C. Gabarró, and J. Font, Simulated smos level 2 and 3 products: The effect of introducing argo data in the processing chain and its impact on the error induced by the vicinity of the coast, *IEEE Trans. on Geosci. and Remote Sens.*, *47*(9), 3041–3050, 2009. 90, 92, 105, 107, 109, 118

Tenerelli, J., N. Reul, A. Mouche, and B. Chapron, Earth-viewing l-band radiometer sensing of sea surface scattered celestial sky radiation - part i: General characteristics, *IEEE Trans. on Geosci. and Remote Sens.*, *46*(3), 659–674, 2008. 54

The ARGO Science Team, On the design and the implementation of argo – an initial plan for a global array of profiling floats, Melbourne, Australia. 57

The SMOS L2OS Team, Smos algorithm theoretical basis document, available at www.smos-bec.cmima.csic.es. 35

Torres, F., I. Corbella, A. Camps, N. Duffo, and M. Vall-llossera, Error budget map to srd (system requirements document) prs, project: Image validation support and seps development, validation and delivery for smos plm, phase c/d, *Tech. Rep. SO-TN-UPCPLM- 0007, v 7.0*, ESA, 2005. 92

Ulaby, F., R. Moore, and A. K. Fung, *Microwave Remote Sensing: Active and Passive – volume II: Radar remote sensing and surface scattering and emission theory*, Addison-Wesley Publishing Company, 1982. xii, 17, 23, 24, 25, 31, 32, 33, 40, 41, 42

Uppala, S. M., et al., The era-40 re-analysis, *Quarterly Journal of the Royal Meteorological Society*, *131*(612), 2961–3012, 1996. 62, 94

Vall-llossera, M., J. Miranda, A. Camps, and R. Villarino, Sea surface emissivity modeling at l-band: An inter-comparison study, in *Proceedings of the WISE/LOSAC/EUROSTARRS campaigns Workshop ESASP525*, pp. 143–153, 2003. 28

Waldteufel, P., and G. Caudal, About off-axis radiometric polarimetric measurements, *IEEE Trans. on Geosci. and Remote Sens.*, *40*(6), 1435–1439, 2002. xii, 35, 36

WOA05, Nodc world ocean atlas 2005 website, http://www.nodc.noaa.gov/OC5/WOA05/pr_woa05.html. 120

Woods, J. D., Diurnal and seasonal variation of convection in the wind mixed-layer of the ocean, *Quarterly Journal of the Royal Meteorological Society*, *106*, 379–394, 1980. 160

Yueh, S. H., Modeling of wind direction signals in polarimetric sea surface brightness temperatures, *IEEE Trans. on Geosci. and Remote Sens.*, *35*(6), 1400–1418, 1997. 25, 26, 55, 125

Zine, S., J. Boutin, P. Waldteufel, J.-L. Vergely, T. Pellarin, and P. Lazure, Issues about retrieving sea surface salinity in coastal areas from smos data, *IEEE Trans. on Geosci. and Remote Sens.*, *45*(7), 2061–2072, 2007. 61, 92

Zine, S., et al., Overview of the smos sea surface salinity prototype processor, *IEEE Trans. on Geosci. and Remote Sens.*, *46*(3), 621–645, 2008. 30, 33, 53, 90, 105, 107, 120, 146